Chaos in Pulsed Laminar Flow

Pankaj Kumar

Dissertation submitted to the Faculty of the
Virginia Polytechnic Institute and State University
in partial fulfillment of the requirements for the degree of

Doctor of Philosophy
in
Engineering Mechanics

Mark A. Stremler, Chair
Hassan Aref
Mark S. Cramer
Pavlos P. Vlachos
Shane D. Ross

August 9, 2010
Blacksburg, Virginia

Keywords: Source-sink, Lid-driven cavity flow, Lyapunov exponent, Kolmogorov entropy,
Topological chaos, Set oriented approach, Almost invariant set

Chaos in Pulsed Laminar Flow

Pankaj Kumar

ABSTRACT

Fluid mixing is a challenging problem in laminar flow systems. Chaotic advection can play an important role in enhancing mixing in such flow. In this thesis, different approaches are used to enhance fluid mixing in two laminar flow systems.

In the first system, chaos is generated in a flow between two closely spaced parallel circular plates by pulsed operation of fluid extraction and reinjection through singularities in the domain. A singularity through which fluid is injected (or extracted) is called a source (or a sink). In a bounded domain, one source and one sink with equal strength operate together as a source-sink pair to conserve the fluid volume. Fluid flow between two closely spaced parallel plates is modeled as Hele-Shaw flow with the depth averaged velocity proportional to the gradient of the pressure. So, with the depth-averaged velocity, the flow between the parallel plates can effectively be modeled as two-dimensional potential flow. This thesis discusses pulsed source-sink systems with two source-sink pairs operating alternately to generate zig-zag trajectories of fluid particles in the domain. For reinjection purpose, fluid extracted through a sink-type singularity can either be relocated to a source-type one, or the same sink-type singularity can be activated as a source to reinject it without relocation. Relocation of fluid can be accomplished using either "first out first in" or "last out first in" scheme. Both relocation methods add delay to the pulse time of the system. This thesis analyzes mixing in pulsed source-sink systems both with and without fluid relocation. It is shown that a pulsed source-sink system with "first out first in" scheme generates comparatively complex fluid flow than pulsed source-sink systems with "last out first in" scheme. It is also shown that a pulsed source-sink system without fluid relocation can generate complex fluid

flow.

In the second system, mixing and transport is analyzed in a two-dimensional Stokes flow system. Appropriate periodic motions of three rods or periodic points in a two-dimensional flow are determined using the Thurston-Nielsen Classification Theorem (TNCT), which also predicts a lower bound on the complexity generated in the fluid flow. This thesis extends the TNCT -based framework by demonstrating that, in a perturbed system with no lower order fixed points, almost invariant sets are natural objects on which to apply the TNCT. In addition, a method is presented to compute line stretching by tracking appropriate motion of finite size rods. This method accounts for the effect of the rod size in computing the complexity generated in the fluid flow. The last section verifies the existence of almost invariant sets in a two-dimensional flow at finite Reynolds number. The almost invariant set structures move with appropriate periodic motion validating the application of the TNCT to predict a lower bound on the complexity generated in the fluid flow.

This dissertation is dedicated to

My parents, Mr. Manohar Lal Gupta and Mrs. Krishna Devi

My wife, Smita

and

My daughter, Sidhi

Acknowledgments

First and foremost, I owe my very deep and profound gratitude to my advisor, Prof. Mark A. Stremler, for his guidance and mentorship in various ways to think like a researcher. He taught me a great deal about the field of fluid mechanics and decision-making in research by providing me opportunities.

I would like to thank Prof. Shane Ross for the many fruitful discussions we had on various topics in the area of dynamics and my research in general.

Also, my sincere thanks to Prof. Hassan Aref, Prof. Mark Cramer, and Prof. Pavlos Vlachos for graciously being on my thesis committee. Also, I would like to thank Dr. Raffaella De Vita for attending my Preliminary Examination and Dr. Sunghwan Jung for being there at my final dissertation presentation.

Alireza, Ganesh, Gautam, Grant, Mohsen, Phanindra, Piyush, Saikat, Souvick, and Udit also deserve my thanks for the many productive sessions we had on various issues of my research.

I should also thank my old friend Saif Iqbal for standing by my side in times of need.

My sincere thanks also belong to Sally Shrader and Lisa Smith, and, in general, the entire Department of Engineering Science and Mechanics.

Last but not least, words can not express the gratitude I have for my parents, Manohar Lal Gupta and Krishna Devi, and most importantly my wife, Smita, for their unconditional love, support, and encouragement. I am also indebted to my beautiful daughter, Sidhi, for all the joy that she has brought to my life.

Contents

List of Figures

List of Tables

Chapter 1

Introduction

The chapter gives a brief review of chaos in pulsed laminar flow, explaining its importance and presenting different tools to generate and analyze it.

1.1 Background

Chaos in fluid flow can enhance convection, which is one of the major modes of heat and mass transfer. A turbulent flow is chaotic and turbulence appears in a flow when the Reynolds number, Re, is larger than a critical threshold (e.g., 2300 in pipe flow, 1500 in flow between parallel plates). The Reynolds number Re characterizes ratio of inertial forces to viscous forces. For a system, if U and L denote characteristic velocity and length scales and ν is the kinematic viscosity, Re is defined as $Re = UL/\nu$. Thus, for large scale systems, it is usually easy to generate turbulence (or chaos) in a fluid flow which is necessary for many natural and engineering phenomena. For example, turbulent wind flow aids in the loss of heat from earth. Another advantage of turbulent wind flow is that it disperses heavy carbon dioxide in the atmosphere. Otherwise, if the air were motionless, all of the carbon dioxide

in the atmosphere would hover at very low altitudes, poisoning the population. Similarly, coolant flow through a device prevents its overheating by transferring heat produced by the device to other devices that use or dissipate it. The turbulence in coolant flows enhances the capability of heat dissipation.

For microfluidic systems, such as microelectronics cooling and DNA microarray analysis, the characteristic dimension is on the order of $\sim$100 μm and U is small. Therefore, the Reynolds number Re is less than unity which leads to laminar microfluidic flows and hence chaos does not come naturally. Generating chaos in such laminar systems is a challenging problem.

Usually, stirring and diffusion are two simultaneous processes leading mixing of two miscible fluids [14]. Stirring increases the mean gradients by stretching and folding the fluid interfaces whereas diffusion decreases the gradient and homogenizes the fluids at the molecular level to complete the mixing. For macrofluidic systems, chaos causes the formation of eddies of many different length scales. The energy cascades from large scale structures to smaller structures and produces a hierarchy of eddies such that the molecular diffusion becomes important and enhances mixing. In laminar fluidic systems, unlike turbulent flows, fluid travels smoothly or in regular paths. In such systems, mixing solely by molecular diffusion is too slow for many applications [43]. The speed of mixing can be increased by stretching and folding of fluid interfaces in such systems. Limitations of fabrication technologies for microfluidic systems constrain the use of standard mixing methods, such as mechanical stirring.

Over the past decades, generating and analyzing chaos in nonlinear dynamical systems, such as microfluidic systems, have emerged as an important subject for research in fluid dynamics [49, 50]. Early interest in compact, high performance, force liquid cooling of planer integrated systems [54] broadened to a comprehensive study of transport and mixing in microfluidic systems with applications to chemical and biological analysis Stremler et al. [47].

The motivation of this thesis is to design fluid transportation methods in microfluidic systems to generate chaos in laminar flows. Two different laminar flow systems are considered. In the first system, chaos is generated in a Hele-Shaw flow by pulsed operation of fluid extraction and reinjection through singularities in a circular domain. This thesis analyzes the fluid transportation with various design parameters like the strength of singularities, position of singularities in the domain, and the method of fluid relocation.

In the second system, we study mixing and transport in a lid-driven cavity flow. Chen [10] uses the structures consisting of fixed points and elliptical islands in lid-driven cavity flow to find lower bounds on complexity of the fluid flow. Certain small perturbations in design parameters destroy the periodic fixed points of low period in the domain. We establish a concept of almost invariant set in lid-driven cavity flow to demonstrate existence of phase space structure required for the prediction of the lower bound on the complexity of the fluid flow. In addition, the concept of almost invariant set as ghost rods is established for the application of TNCT to the lid-driven cavity flow with finite Reynolds number. The study of mixing in a laminar flow with finite Reynolds number is necessary for the simulation and optimization of real-world mixers.

1.2 Chaotic advection

Advection is a term used to describe the transport of a material by fluid in which the velocity of the material particle is equal to the velocity field of the fluid in space and time. The advection equation of the material is given by

$$\frac{d\vec{x}}{dt} = \vec{v}(\vec{x}, t), \tag{1.1}$$

where $\vec{v}(\vec{x}, t)$ is the velocity field of the fluid and $\vec{x}$ is the position vector.

The trajectory of the material particle is chaotic when the advection equation 1.1 is non-integrable, and this phenomenon is known as chaotic advection [2]. Chaotic advection is widely used for improving and analyzing mixing in laminar flow by enhancement of stretching and folding of material interfaces [47]. The stretching and folding of material interfaces increases the specific interfacial area σ_d which is inversely proportional to the diffusion distance L_d; thus, the specific interfacial area σ_d increases and the diffusion distance L_d decreases. At the microscopic level, the molecular transportation time t_d is proportional to L_d^2 resulting faster diffusion; thus enhances mixing [40]. Chaotic advection can occur in different laminar flows, from Stokes flow to potential flow [8], and with applications to different flow systems, including unsteady two-dimensional flows [11, 20] as well as both steady and time periodic three-dimensional flows [47].

Theoretically, without the action of molecular diffusion, the complete picture of the mixing can be given by the location of the material interfaces as a function of space and time [35] which can grow exponentially in time even with a relatively simple velocity field.

This dissertation investigates chaotic advection in two different laminar flow systems using different techniques employed in the analysis of dynamical systems, like the Poincaré section [26, 35, 37, 38], the Lyapunov exponent [27, 34], the Kolmogrov-Sinai (KS) entropy [23, 41, 42], the almost invariant set (AIS), and the topological entropy [1, 33].

Chapter 2

Mathematical Foundation

2.1 Dynamical systems

A dynamical system is a smooth action of real or integer numbers on another object (usually a manifold). Systems in which real numbers act are called continuous dynamical systems and systems in which integer numbers act are called discrete dynamical systems. In practice, a flow $\vec{x} = \Psi_t(\vec{X})$ is generated by the Eulerian velocity field given as

$$d\vec{x}/dt = \vec{v}(\vec{x}, t), \tag{2.1}$$

with the initial conditions $\vec{x}_{t=0} = \vec{X}$ and $\vec{x} \in \mathbb{R}^n$. The motion of a fluid particle in an Eulerian velocity field is a continuous dynamical system.

For an incompressible steady flow in 2D there exists a streamfunction $\psi(x, y)$ and the path-

lines coincide with the streamlines. Trajectories of particles can be defined as

$$\frac{dx}{dt} = -\frac{\partial \psi}{\partial y} \tag{2.2}$$

$$\frac{dy}{dt} = \frac{\partial \psi}{\partial x}, \tag{2.3}$$

which is a Hamiltonian system and $H(x, y) = \psi(x, y)$ is the Hamiltonian function of the system. The dimension of the phase space is 2; thus, the Hamiltonian system defined by Eqs. (2.2) amd (2.3) has one degree of freedom. If the Hamiltonian does not depend explicitly on time t, then the value of ψ is invariant, and the system is conservative. For this system 'phase space' is 'configuration space'.

This thesis analyzes flows which is indeed dissipative system. However, either pulsing the fluid flow or driving the boundaries adds energy to the system, so that the resulting velocity field is time-periodic. Motion of a passive particle in the Hamiltonian system discussed is controlled by advection equation Eq. (2.1). Thus, passive particle motion is conservative while the underlying velocity field is generated by dissipative systems.

The dimension of a continuous dynamical system can be reduced by one when the flow positions are recorded at specified times as

$$\vec{x}_n = \Phi_T^n(\vec{x}_0) \tag{2.4}$$

$$\vec{x}_{n+1} = \Phi_T(\vec{x}_n), \tag{2.5}$$

where Φ_T is a mapping with the time step T and $n = 0,\ 1,\ 2, \ldots$. The system described in Eqs. (2.5) and (2.4) is a discrete dynamical system.

2.2 Hele-Shaw flow

The governing equations for an incompressible Newtonian flow in an inertial frame of reference are [3]

$$\nabla \cdot \vec{u} = 0, \tag{2.6}$$

and

$$\rho \left[\frac{\partial \vec{u}}{\partial t} + \vec{u} \cdot \nabla \vec{u} \right] = -\nabla p + \mu \nabla^2 \vec{u} + \vec{f}, \tag{2.7}$$

where $\vec{u}$ is the flow velocity, ρ is the fluid density, p is the pressure, and $\vec{f}$ is the body force. For a Hele-Shaw flow as shown in Fig. 2.1, Eq. (2.7) can be written as

$$\nabla(p/\mu) = \nabla^2 \vec{u}, \tag{2.8}$$

where $\vec{u} = u_x \hat{e_x} + u_y \hat{e_y}$. Equation (2.8) can be written as

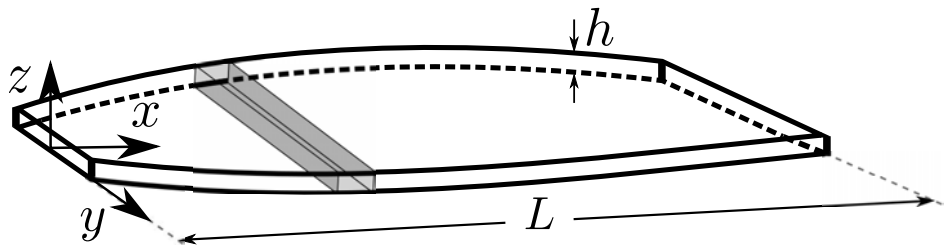

Figure 2.1: Hele-Shaw flow.

$$\frac{\partial p}{\partial x} = \mu \frac{\partial^2 u_x}{\partial z^2} \tag{2.9}$$

$$\frac{\partial p}{\partial y} = \mu \frac{\partial^2 u_y}{\partial z^2} \tag{2.10}$$

$$\frac{\partial p}{\partial z} \sim 0. \tag{2.11}$$

Using the boundary conditions $\vec{u}_{z=0} = 0$ and $\vec{u}_{z=h} = 0$, a solution of Eqs. (2.9), (2.10), and (2.11) is

$$\vec{u} = \frac{z}{2\mu}(h - z)\nabla p, \tag{2.12}$$

where $p = p(x, y)$.

For small value of $h \ll 1$, Eq. (2.12) can be simplified by averaging the velocity as

$$\vec{\bar{u}} = \frac{1}{h}\int_0^h \vec{u}dz = \frac{h^2}{12\mu}\nabla p = \nabla\phi, \tag{2.13}$$

where $\vec{\bar{u}}$ is the depth-average velocity between two parallel plates and is a ϕ potential scalar. Thus, with the depth-averaged velocity, the flow between the parallel plates can effectively be modeled as two-dimensional potential flow. Models take into account the viscous interaction of fluid with the top and bottom plates.

2.3 Fluid flow in lid-driven cavity

For a steady and slow fluid flow with constant viscosity when the body force is negligible, if the principal boundary conditions involve $\vec{u}$ alone, then Eq. (2.7) can be written as

$$\nabla \times \nabla(p/\mu) = \nabla \times \nabla^2\vec{u} = \nabla^2(\nabla \times \vec{u}) = 0. \tag{2.14}$$

For a two-dimensional steady flow with negligible inertia, the solenoidal velocity field from Eq. (2.6) can be written as

$$\vec{u} = \nabla \times \psi, \tag{2.15}$$

where ψ is a streamfunction. With Eq. (2.15), the vorticity equation for $\nabla \times \vec{u}$ can be written as

$$\nabla \times \vec{u} = -\nabla^2 \psi. \tag{2.16}$$

Combining Eqs. (2.14) and (2.16) gives the biharmonic equation,

$$\nabla^2(\nabla^2 \psi) = 0. \tag{2.17}$$

So, the streamfunction of a two-dimensional incompressible Newtonian fluid in the Stokes flow regime satisfies the two-dimensional biharmonic equation.

2.4 Fixed and periodic point

For a given flow $\vec{x} = \Psi(\vec{x}, t)$, $\vec{x}_f$ is a fixed point if

$$\vec{x}_f = \Psi(\vec{x}_f, t)$$

for any time t. A point $\vec{x}_p$ is a periodic point with period T if

$$\vec{x}_p = \Psi(\vec{x}_p, T).$$

For a discrete dynamical system, $\vec{x}_{n+1} = \Phi(\vec{x}_n)$, a point $\vec{x}_f$ is a fixed point of the mapping $\Phi(.)$ if

$$\vec{x}_f = \Phi^n(\vec{x}_f) \tag{2.18}$$

for any value of n. Point $\vec{x}_f$ is a periodic point of order n if Eq. (2.18) is true for some value of n such that $\vec{x}_f \neq \Phi^{n_1}(\vec{x}_f)$ for any $n_1 < n$. The smallest possible value is $n = 1$. A

fixed point of a flow and its corresponding mapping are not the same, but a fixed point of a mapping corresponds to a periodic point of the flow, as shown in figure 2.2.

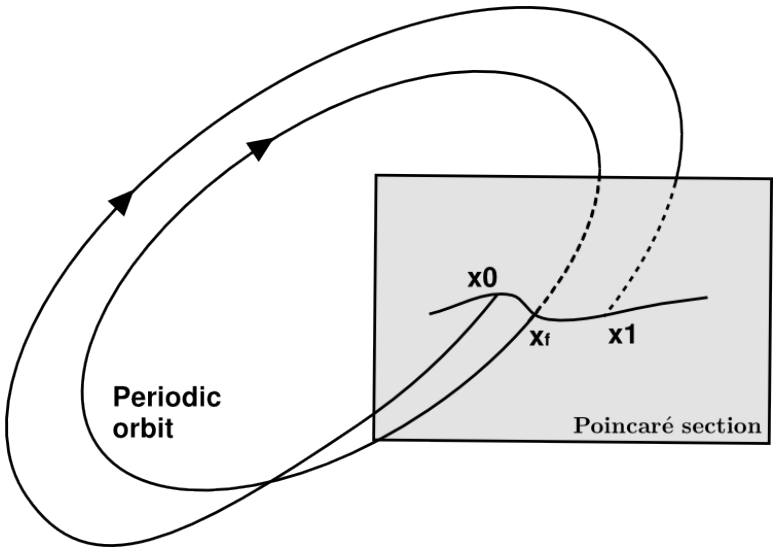

Figure 2.2: Poincaré section for a flow with x_f as a fixed point of the mapping which corresponds to the periodic point of the flow.

2.5 Poincaré section

A Poincaré section can be interpreted as a discrete dynamical system with a state space dimension smaller than the original continuous dynamical system. A Poincaré section displays a plot with the characteristics of the solutions belonging to all possible initial conditions. Figure 2.3 is a sample Poincaré section showing characteristics of a lid-driven cavity flow with all possible initial conditions. The Poincaré section shown in Fig. 2.3 can be divided into two regions:

1. Circular, elliptical, and closed curved structures known as regular regions.
2. A region with a random distribution of points without any structure known as the chaotic sea.

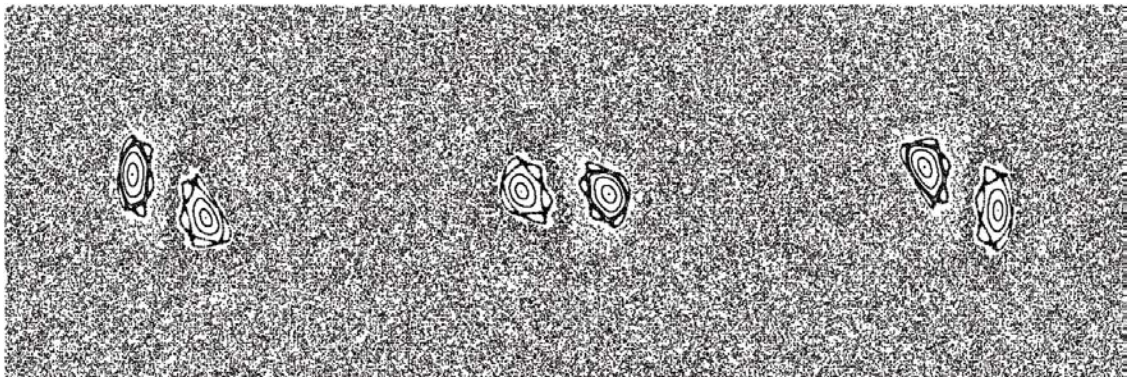

Figure 2.3: A sample Poincaré section for lid-driven cavity flow .

A fluid particle with an initial condition in the chaotic sea moves all over the chaotic sea. A particle in a regular region follows a fixed circular, elliptical or closed curved trajectory. Also, a particle in the chaotic sea never enters any regular region, and neither do trajectories in regular islands go to the chaotic sea.

2.6 Lyapunov exponents and the Kolmogorov entropy

A Lyapunov exponent of a dynamical system is a quantity that characterizes the rate of divergence of infinitesimally close trajectories [35]. Hence, for a fluid flow it characterizes the average stretching rate of material lines. For two trajectories in phase space with initial separation $\delta\vec{Z}_0$, as shown in Fig. 2.4, the final separation $\delta\vec{Z}(t)$ after time t is given as

$$\delta\vec{Z}(t) = e^{\lambda t}\left|\delta\vec{Z}_0\right|, \tag{2.19}$$

where λ is the Lyapunov exponent. A total of N Lyapunov exponents exist for a N dimensional phase space with different orientation of initial separation vector. For a system such

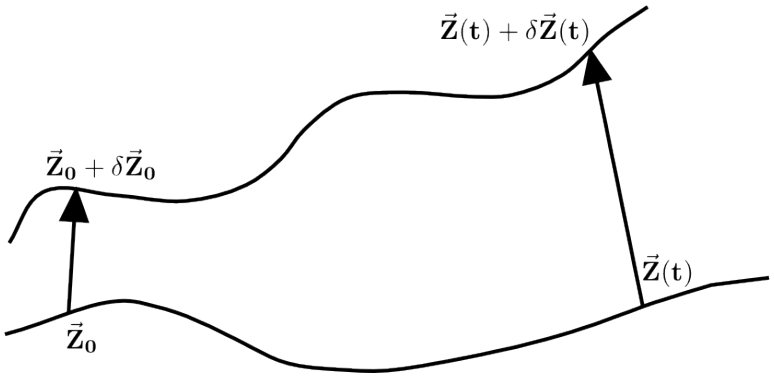

Figure 2.4: Generation of trajectories from two infinitesimally close points $\vec{Z}_0$ and $\vec{Z}_0 + \delta\vec{Z}_0$.

that $\nabla.\vec{u} = 0$ and $\det(D\phi_t(\vec{X})) = 1$,

$$\sum_{i=1}^{N} \lambda_i = 0. \tag{2.20}$$

For a dissipative system

$$\sum_{i=1}^{N} \lambda_i < 0. \tag{2.21}$$

This thesis discusses systems with two dimension in phase space, so there are a total of two Lyapunov exponents. The maximum Lyapunov exponent is defined by

$$\lambda = \lim_{t\to\infty} \frac{1}{t} \ln \frac{\left|\delta\vec{Z}(t)\right|}{\left|\delta\vec{Z}_0\right|} \tag{2.22}$$

Numerical computation of maximum Lyapunov exponent

In general, maximum Lyapunov exponent is computed by calculating average logarithmic rate of separation between two nearby trajectories. Procedure to compute the value of maximum Lyapunov exponent is as follows:

1. Select two nearby points separated by distance δZ_0. An appropriate choice of δZ_0 is one that is about 1000 times larger than the precision of the floating point numbers

that are being used.

2. Advance the trajectories of both the points for pulse time T and calculate the new separation δZ as shown in Fig. 2.5. For a two-dimensional system with variables x

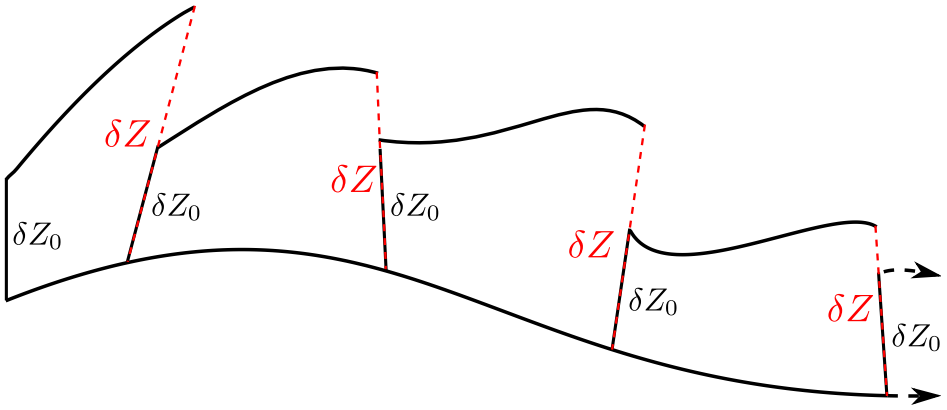

Figure 2.5: Schematic of trajectories to compute the Lyapunov exponent.

and y, the separation would be $\delta Z = \sqrt{(x_a - x_b)^2 + (y_a - y_b)^2}$, where the subscripts (**a** and **b**) denote the final position of the points.

3. Evaluate $\log |\delta Z / \delta Z_0|$.

4. Readjust the position of one point so its separation is δZ_0 in the same direction as δZ as shown in Fig. 2.5.

5. Calculate a running average for a few thousand of periods which converges the result to the maximum Lyapunov exponent.

The Kolmogorov (KS) entropy is used to quantify the chaos generated in pulsed source-sink systems [43, 44]. The sum of all positive Lyapunov exponents gives an estimate of the KS entropy [10, 19, 36, 42],

$$h_{KS} = \int_P \sum_{\lambda_i > 0} \lambda_i d\mu_s, \tag{2.23}$$

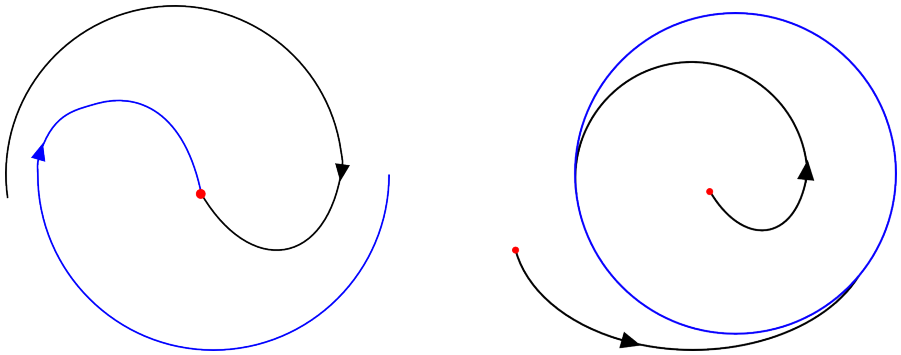

Figure 2.6: Dissipative or non-conservative systems. (a) Dissipative system with attracting fixed point and (b) dissipative system with attracting orbit.

where μ_s is the area of a chaotic sea. In case of only one chaotic sea in the system, the KS entropy can be estimated as

$$h_{KS} = \mu_s \lambda, \tag{2.24}$$

The value of μ_s can be computed as

$$\mu_s = \frac{A_c}{A_p}, \tag{2.25}$$

where A_c and A_p are the areas of chaotic sea in phase space and the total area of phase space respectively. $h_{KS} = 0$ denotes a non-chaotic system and $h_{KS} > 0$ shows presence of chaos in the system.

Case 1: $\lambda < 0$

Negative Lyapunov exponents are characteristic of a dissipative or nonconservative system. One common example of such a system is the damped harmonic oscillator. Trajectories of phase space variables get attracted to a fixed point, as shown in Fig. 2.6a, or to a periodic trajectory as shown in Fig. 2.6b.

Case 2: $\lambda = 0$

A Lyapunov exponent of zero value indicates that the system is in some sort of steady state mode and is non-chaotic. A physical system with this exponent is conservative. The trajectory of a phase space variable with $\lambda = 0$ is either a neutral fixed point (or an eventual fixed point) or a closed curve as shown in Fig. 2.7.

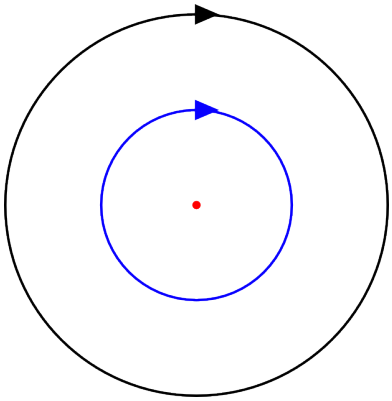

Figure 2.7: Conservative system with natural fixed point and orbits

Case 3: $\lambda > 0$

The trajectory of a phase space variable is unstable and chaotic for the Lyapunov exponent $\lambda > 0$. Initially nearby points , no matter how close, will diverge to arbitrary separation. These points are unstable and all neighborhoods in the chaotic sea of the phase space will eventually be visited. Figure 2.3 shows a Poincaré section for a lid-driven cavity flow with $\lambda > 0$ for the chaotic sea.

2.7 Topological chaos and topological entropy

The complexity of a dynamical system can also be measured in terms of topological entropy, a nonnegative real number typically denoted by h [18, 33]. For two dimensional flows, topological entropy is equal to the maximum line stretching exponent over all possible initial material lines [7, 17]. Assume a two dimensional domain D with incompressible fluid and N number of movable cylindrical stirrers inserted with configuration R_N, where the subscript N denotes the number of stirrers (holes) are in the fluid region, as shown in Fig. 2.8. Stirring action consists of a motion of one or more stirrers along specified trajectories within the domain D such that at the end of a 'stirring cycle' the stirrers are at the same positions as when the cycle began (although generally permuted, and possibly rotated about their axes). So, the stirrers move in a certain way such that they map onto itself and the mapping is differentiable, one-to-one, and its inverse is differentiable, i.e. it is a diffeomorphism. For

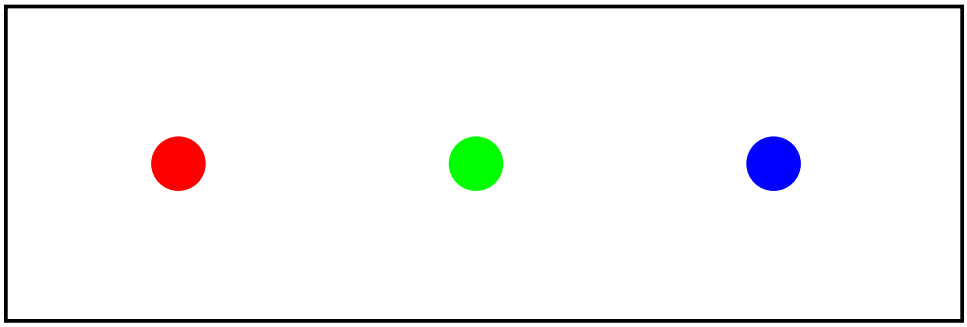

Figure 2.8: A schematic of two dimensional domain with $N = 3$ number of cylindrical stirrers.

such system, topological entropy can be determined by computing the stretching rate of topologically non-trivial lines [33]. A line connecting a stirring rod with the outer boundary or a loop that encircles exactly two of the stirring rods can be selected as a non-trivial line [45]. The value of the topological entropy is always greater than or equal to the Lyapunov exponent, and the difference of these two values gives an indications of the uniformity of

stretching in the flow [53].

2.7.1 Thurston-Nielsen Classification Theorem

Let the N number of stirrers in domain D with initial configuration R_N undergo a cyclic motion and return back to their initial configuration at the end of the cycle. Schematics of the cyclic motion of $N = 3$ stirrers are shown in Fig. 2.9. Two diffeomorphisms are said

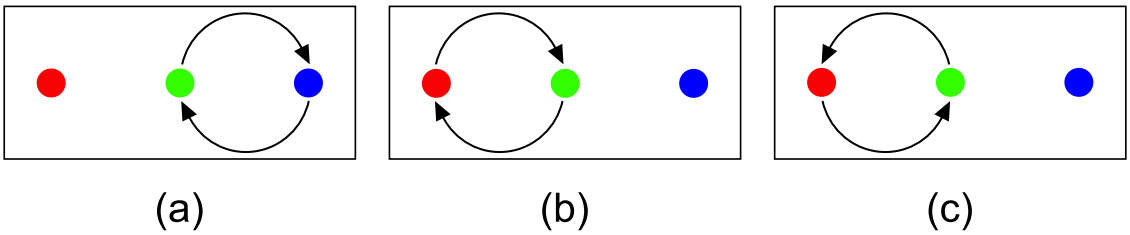

Figure 2.9: Illustration of stirrers interchange with $N = 3$ stirrers. (a) R_+ interchange with braid σ_2, (b) L_+ interchange with braid σ_1, and (c) L_- interchange with braid σ_{-1}.

to be isotopic if they can be continuously deformed into each other without motion of the boundaries. A precise definition of the Thurston-Nielsen theorem is given by [8]:

If f is a homeomorphism of a compact surface, S, then f is isotopic to a homeomorphism, φ, of one of the following types:

1. *Finite order: the n^{th} iterate of φ is isotopic to the identity;*
2. *Pseudo-Anosov: φ preserves a pair of transverse, measured foliations, $\mathcal{F}_u$ and $\mathcal{F}_s$, and there is a $\lambda > 1$ such that φ stretches $\mathcal{F}_u$ by a factor λ and contracts $\mathcal{F}_s$ by $1/\lambda$*
3. *Reducible: φ fixes a family of reducing curves, and on the complementary surfaces satisfies (1) or (2).*

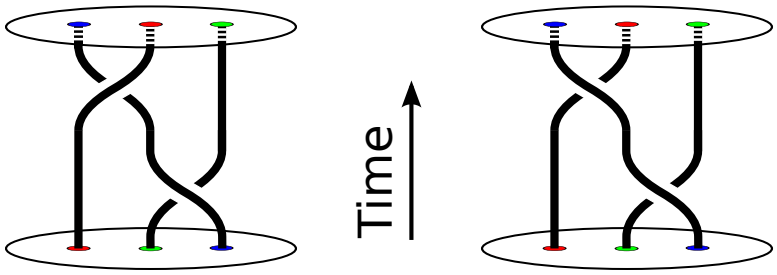

Figure 2.10: (a) A pseudo Anosov braid and (b) a finite order braid.

The theorem applies to the more general homeomorphisms, i.e. invertible, continuous, but not necessarily differentiable mappings. For fluid mechanics applications we usually assume differentiability and so we have focused on diffeomorphisms. The theorem deals with compact surfaces, i.e. finite regions of stirred fluid. It applies only to two-dimensional flows. Two diffeomorphisms are isotopic if one can be deformed continuously into the other. If two stirred motions f and g are isotopic then we can accomplish the same stirred motion as g by first performing the stirred motion dictated by f and then followed by a fixed stirrer diffeomorphism h. For a given stirred motion f, all diffeomorphisms isotopic to f are called its isotopy class. The finite order isotopy classes are topologically trivial but there can be some chaotic region in it due to the dynamics of the flow not due to the topology of the boundary motion. The pseudo-Anosov isotopy classes are chaotic. The reducible class is a combination of both the finite order and the pseudo-Anosov regions.

Assume a two dimensional domain with N number of identical stirrers inserted as shown in Fig. 2.9. The stirrers never come in contact with or go across one another or the boundary. For $N = 1,\ 2$ the flow is isotopic to the identity with any stirrers motion, i.e., from a topological point view the stirring pattern can be recovered by simply rotating the outer boundary. However, with the number of stirrers $k \geq 3$ it is possible to generate complex stirring pattern which can not be recovered simply by rotating the outer boundary. As discussed in [8], consider the simplest case with $N = 3$ stirrers to generate and analyze

chaos. Figure 2.9 shows three different types of stirring operations labeled as R_+, L_+, and L_-. As shown in Fig. 2.10, a stirring cycle consists of R_+ followed by L_- is isotopic to the pseudo-Anosov class and a stirring cycle consists of R_+ followed by L_+ is isotopic to the finite order class.

The pseudo-Anosov maps are a generalization of the Anosov mapping [8]. A brief review of the theory of the linear Anosov diffeomorphism on the two dimensional torus T^2 explains important properties. To get the linear Anosov map on T^2, we can start with a positive integer matrix,

$$M = \begin{bmatrix} a & b \\ c & d \end{bmatrix}, \tag{2.26}$$

with unit determinant $ad - bc = 1$, and $a + d > 2$. The matrix M defines a mapping f_M, on the plane given by $f_M(x, y) = (ax + by, cx + dy)$.

In the same way, a matrix A with two positive real eigenvalues λ and $1/\lambda$, can represent pseudo-Anosov map. For a fluid system with the pseudo-Anosov case, the fluid stretches exponentially at a rate λ in the unstable direction and $1/\lambda$ in the stable direction.

The TNCT predicts a quantitative lower bound on the topological entropy of a pseudo-Anosov type stirring. To use the TNCT to compute the stretching rate in the pseudo-Anosov case, a matrix representation of the stirring protocol can be generated [8]. This thesis presents a method in chapter 4 to derive the matrix representing the stirring protocol. With continuity and smoothness assumption the stirrer produces a (2+1) dimensional "world line" as shown in Fig. 2.10. The mathematical framework to identify trajectories of the stirrers interchange and labeling are provided by Artin's braid group [28]. Three different types of interchange motions of the stirrers and labeling are shown in Fig. 2.9. Each trajectory interchange is a generator for the overall braid. Generator σ_i means the i^{th} and $(i+1)^{th}$ rods interchange their positions clockwise, while σ_{-i} means the i^{th} and $(i+1)^{th}$ rods interchange

their positions anti-clockwise. Note that the index i here refers to the current position of a rod obtained by projecting the positions on $x-$axis and counting from the left, and hence it does not always refer to same rod. For example, in Fig. 2.9(a) the 2^{nd} rod interchanges position clockwise with the 3^{rd} rod resulting in generator σ_2. Figure 2.9(b) shows the σ_1 generator in which the 1^{st} rod interchanges position clockwise with the 2^{nd} rod. In Fig. 2.9(c) the 1^{st} rod interchanges position anti-clockwise with the 2^{nd} rod resulting in the generator σ_{-1}.

The stirrer interchanges in the 3-stirrer problem can be represented by a 2×2 integer matrix. The generator σ_2 is represented by the matrix

$$M_2 = \begin{bmatrix} 1 & 0 \\ 1 & 1 \end{bmatrix} \tag{2.27}$$

and the generator σ_{-1} by

$$M_{-1} = \begin{bmatrix} 1 & 1 \\ 0 & 1 \end{bmatrix}. \tag{2.28}$$

A detailed derivation of the matrix representation is discussed in [8].

For the system considered in Fig. 2.10 (a), σ_{-1} follows σ_2, and in the notation used here the braiding motion is represented as $\sigma_{-1}\sigma_2$. The matrix representation of the braiding $\sigma_{-1}\sigma_2$ is

$$M = M_{-1}M_2 = \begin{bmatrix} 1 & 1 \\ 0 & 1 \end{bmatrix} \begin{bmatrix} 1 & 0 \\ 1 & 1 \end{bmatrix} = \begin{bmatrix} 2 & 1 \\ 1 & 1 \end{bmatrix} \tag{2.29}$$

which has the two eigenvalues $\frac{1}{2}(3 \pm \sqrt{5})$.

The derived matrix M in Eq. (2.29) is an irreducible transition matrix for a chaotic pseudo-Anosov map. Thus, the considered flow stretches along the unstable manifold by a factor

$\lambda = \frac{1}{2}(3+\sqrt{5}) > 1$ and contracts along the stable manifold by a factor $1/\lambda = \frac{1}{2}(3-\sqrt{5}) < 1$, with finite number of singularities. According to Handel's isotopy stability theorem, this complicated behavior is preserved under isotopy, so that in a subdomain of the fluid system the stirring motion produces stretching at a rate that is at least λ. The TNCT does not predict the size of the domain, but experimentally it is shown that the subdomain is in the scale of the stirrer motions. Thus, limited topological data in a subdomain predicts a quantitative lower bound on complexity in the dynamics of the flow with stirring motion of psudo-Anosov type. For $N > 3$, the Bestvina-Handel algorithm can be used to compute the topological entropy [8]. A free software, the 'train track code', is available for implementation of the algorithm [5, 6].

2.8 Statistical approach

Under certain conditions, a nonlinear dynamical systems can be treated as Markov chains on a state space to study various probability measures propagating under the application of the system. The propagator is called the "Perron-Frobenius operator" P of the underlying dynamical system. This section gives a brief review of a class of statistical techniques for discrete-time dynamical system using "Perron-Frobenius operator" (PF-operator) P, which enables us to numerically compute various mathematical objects that quantify transport in a system by computing statistically important sets in the phase space. The computations are based on an appropriate discretization of the PF-operator P containing important information about the dynamical system. The various eigenvectors and eigenvalues of such a linear operator give an insight into transport in phase space at various level of detail.

In mathematics, a σ-algebra $\mathcal{B}$ over a set $\mathcal{X}$ is a family of subsets of $\mathcal{X}$ which is closed under countable set operations. Formally, $\mathcal{B}$ is a σ-algebra if and only if it has the following

properties:

1. The empty set is in $\mathcal{B}$,

2. If E is in $\mathcal{B}$ then so is the complement of $\mathcal{E}$.

3. If $\mathcal{E}1$, $\mathcal{E}2$, $\mathcal{E}3$,... is a sequence in $\mathcal{B}$ then their (countable) union is also in $\mathcal{B}$.

From 1 and 2 it follows that $\mathcal{X}$ is in $\mathcal{B}$; from 2 and 3 it follows that the σ-algebra is also closed under countable intersections. The Borel σ-algebra on a topological space $\mathcal{X}$ with topology T is the smallest σ-algebra containing T.

Consider a discrete dynamical system:

$$x_{i+1} = f(x_i), \tag{2.30}$$

where $i = 1,\ 2,\ 3, \ldots$ and $f : X \to X$ refers to a diffeomorphism on a compact subset $X \subset \mathcal{R}^n$. Let $\mathbf{B}$ be the Borel σ-algebra on X, and denoted by m the Lebesgue measure on $\mathbf{B}$.

Definition 1. *A subset $A \subset X$ is called invariant if $f(A) \subseteq A$.*

Consider $p(x, .)$ as the stochastic transition function associated with the system, i.e., $p(x, A)$ is the probability that the first iterate of $x \in X$ lies in the set $A \subset X$. For the deterministic case, $p(x, .) = \delta_{f(x)}$. We can consider that for every $x \in X$, the probability measure $p(x, .)$ is absolutely continuous with respect to the Lebesgue measure m. So, $p(x, A)$ can be written as

$$p(x, A) = \int_A k(x, y) dm(y) \tag{2.31}$$

for all $A \subset \mathbf{B}$, where $k(x, y)$ is a transition density function $k : X \times X \to \mathbf{R}$.

Let B denote the open unit ball in $\mathcal{R}^n$ and $\mathcal{X}_B$ the characteristic function of B, i.e.,

$$\mathcal{X}_B(x) = \begin{cases} 1 & \text{if } \|x\| \leq 1 \\ 0 & \text{otherwise.} \end{cases} \tag{2.32}$$

For $\epsilon > 0, x, y \in X$, we can write

$$k_\epsilon(x, y) = \frac{1}{\epsilon^n m(B)} \mathcal{X}_B \left(\frac{1}{\epsilon}(y - x) \right). \tag{2.33}$$

The value of $k_\epsilon(x, y)$ evaluates to zero if the distance between points x and y is greater than ϵ. Hence the transition density function can be replaced by $k_\epsilon(f(x, y), y)$ and Eq. 2.31 can be written as

$$p_\epsilon(x, A) = \int_A k_\epsilon(f(x), y) dm(y). \tag{2.34}$$

Definition 2. *The Perron-Frobenius operator P on any measure ν is defined as*

$$P\nu(A) = \int p(x, A) d\mu(x) \tag{2.35}$$

In the deterministic case, this reduces to

$$P\nu(A) = \nu(f^{-1}(A)), \tag{2.36}$$

where f describes the deterministic dynamical system defined in equation 2.30.

Definition 3. *A measure μ is said to be invariant under the evolution of system defined by stochastic transition function p if it satisfies*

$$\mu(A) = \int p(x, A) d\nu(x), \tag{2.37}$$

for all $A \in \mathbf{B}$. So, if μ is an invariant measure of the system, then

$$\mu(A) = \int p(x, A) d\mu(x) = P\mu(A), \tag{2.38}$$

for all $A \in \mathbf{B}$. Hence, any invariant measure of the system is an eigenfunction of the PF-operator P with eigenvalue 1.

Definition 7. *An invariant measure μ is an SRB measure if there exists a subset $U \subset X$ with $m(U) > 0$ and such that for each continuous function ψ*

$$\lim_{n\to\infty} \frac{1}{n} \sum_{i=0}^{n-1} \psi(f^i(x)) = \int \psi d\mu, \tag{2.39}$$

for all $x \in U$.

The above relation always holds for almost all x which belong to sets having a non-zero μ measure, by the Birkhoff Ergodic Theorem. When measure μ is a SRB measure then temporal average equals the spatial average for a set of initial conditions with positive m including $m = 0$. Thus, SRB measures are also called as natural measures or physical measures.

Discretization of PF-operator

Phase space need to be discretized in order to compute the PF-operator. If we discretize the domain X by a collection of small boxes, i.e. $X \subset (B_1 \cup B_2 \cup \ldots \cup B_n)$ then we are discretizing the PF-operator by creating a n-state Markov chain, where each box $B \in (B_1, B_2, \ldots, B_n)$ corresponds to a state in the chain. For a deterministic system, (i,j)th element of the

stochastic matrix P of the Markov chain can be defined as

$$P_{ij} = \frac{m(B_i \cap f^{-1}(B_j))}{m(B_i)}, \tag{2.40}$$

which is the probability that a randomly chosen point in B_i will be mapped into B_j over one iteration as shown in Fig. 2.11. The dynamics of Markov chain consist of the dynamics

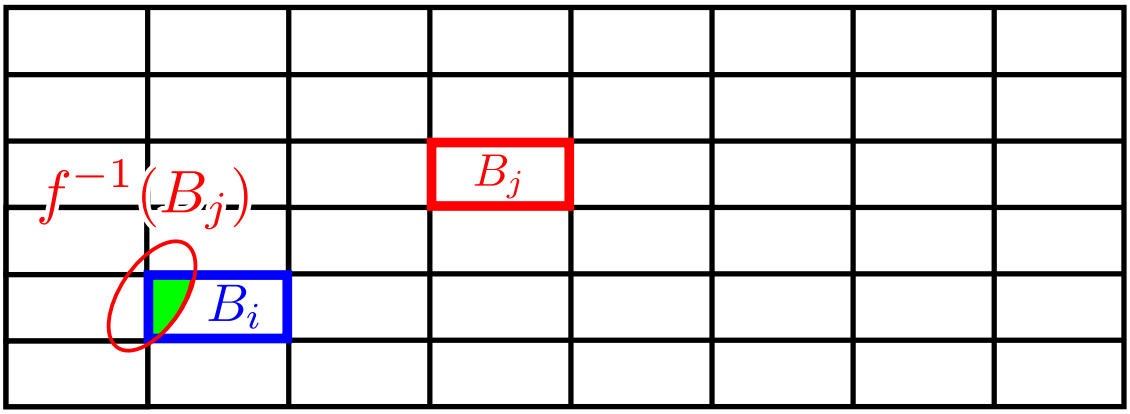

Figure 2.11: Discretization of domain into boxes. The green color region is $B_i \cap f^{-1}(B_j)$

of the map f in addition of some noise due to discretization of the PF-operator. First left eigenvector p of the matrix P gives an estimate of the physical-invariant measure of the system, $\mu(B_i) = p_i$, which can be extended over any Borel-set $A \in X$ by

$$\mu(A) = \sum_{i=1}^{n} \frac{m(A \cap B_i)}{m(B_i)} p_i. \tag{2.41}$$

Almost invariant sets

The transition probability of mapping from set A_1 into A_2 under action of stochastic transition function is defined as

$$p(A_1, A_2) = \frac{1}{\mu(A_1)} \int_{A_1} p(x, A_2) d\mu(x). \tag{2.42}$$

Then the quantity $p(A, A)$ can be denoted as $\rho_\mu(A)$ is the fraction of the phase space volume of set A that maps back to the set over one iteration of the map.

Definition 8. *A set $A \subset X$ is said to be almost invariant if*

$$\rho_\mu(A) = \frac{\mu(A \cap f^{-1}(A))}{\mu(A)} \approx 1, \tag{2.43}$$

i.e., the points in the set map back to the same set over one iteration of the map with high probability, with the measure being the invariant measure μ.

Chapter 3

Pulsed Source Sink Pair Flow

3.1 Introduction

The mechanics of a wide range of practical applications in engineering and natural science can be represented by potential flows such as DNA microarray analysis [47], groundwater flow, flow within porous media and oil recovery in shale beds [24, 25]. This chapter presents pulsed source-sink systems to achieve chaotic advection in potential flow. One of the major applications of such systems is in massively parallel expression screening, a biological tool used widely in genomic research [4, 12, 21, 32, 47] as shown in Fig. 3.1. In this technology, immobilized, well-characterized probe molecules are spotted on surface which are shown as an array of black small circles in Fig. 3.1. Unknown complementary target biomolecules are suspended in a solution placed in between the surfaces to find its characteristics by finding its binding sequence with the probe molecules. The prediction of the best possible characteristic of the unknown complementary target biomolecules is possible when every target biomolecule in the solution has the equal probability to interact with each of the spotted probe molecules on the surface. The standard size of a microarray analysis is $7.5\ cm \times 2.5\ cm \times 50\ \mu m$.

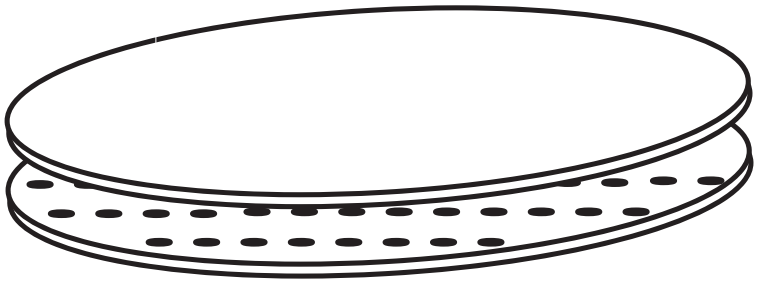

Figure 3.1: A schematic of the massively parallel expression screening. Immobilized well-characterized probe molecules are spotted on surface. Unknown complementary target biomolecules suspended in a solution placed in between the plates.

Thus, the target solution stays in a very high-aspect-ratio volume. For small separation between two parallel surfaces of microarray analysis, the fluid motion across the microarray surface can be modeled as Hele-Shaw flow with the depth averaged velocity proportional to the gradient of the pressure, which can be represented by velocity potential as described in section 2.2. For high-aspect-ratio value, with no fluid motion, the interaction of the target molecules to the probe molecules relies on very slow diffusion of the target molecules. Chaotic advection of the target molecules can improve and accelerate the interaction of target molecules to the probe molecules, which will increase the number of target molecules that bind to a probe spot and reduce the required number of target molecules. Jones and Aref [24] present a pulsed system with one source and one sink as a time-dependent flow to generate chaos in an unbounded domain. A source or a sink is a point singularity through which fluid is injected or extracted, respectively. In practice, a source or sink can be made by putting a hole in one of the plates bounding a Hele-Shaw flow. In [24], the source and the sink with equal strength q operate alternately at time intervals $\delta t = A/q$, where A is the extracted or reinjected fluid area through the sink or source, respectively. The detailed description of the system is discussed in [24]. It is shown that chaotic advection can generate chaos in potential flow with pulsed source-sink system.

Different designs of pulsed source-sink systems with two sources and sinks in bounded do-

mains are presented in [16, 29, 46]. In a bounded domain, one source and one sink with equal strength operate together as a source-sink pair to conserve the volume of the fluid. Chaotic advection in such systems mainly depends on domain geometry, arrangement of source-sink pairs, reinjection procedure of the extracted fluid, pulse time, and the method of transporting the extracted fluid from the sink to the corresponding source. Authors of [43] present a pulsed source-sink system in a bounded rectangular domain. In this work, the model for the fluid flow requires evaluation of an elliptic integral of the first kind and so computing a particle positions is computationally costly. Therefore, [43] presents results for only one fixed source-sink arrangement.

The motivation of the presented work is to consider a pulsed source-sink system governed by a simple mathematical equation to increase the computation speed, allowing for a more comprehensive analysis of the parameter space. Additionally, the presented work aims to design and analyze pulsed source-sink systems with various arrangements of source-sink pairs, reinjection procedure of the extracted fluid, pulse time, and transportation methods of the extracted fluid from the sink to the corresponding source.

This chapter presents and analyzes different arrangements of two source-sink pairs in a bounded circular domain. Section 3.2 presents a mathematical model for steady operation of a single source-sink pair. Section 3.3 presents the pulsed source-sink pair protocols used to generate chaos by relocating the extracted fluid from a source to corresponding sink. In Section 3.5, a pulsed source-sink system is presented that generates chaotic advection without fluid relocation, thereby enabling simplified fabrication and operation of devices for practical implementation.

3.2 Mathematical formulation: one source-sink pair

Consider a steady flow owing to simultaneous operation of a point source and a point sink in an unbounded plane. Let the source and sink both have strength q, and be positioned at $z_p(= x_p + iy_p)$ and $z_n(= x_n + iy_n)$, respectively, on the complex plane. The complex potential for this flow is

$$F(z) = (q/2\pi)[\log(z - z_p) - \log(z - z_n)]. \tag{3.1}$$

Streamlines in this flow are given by $Im(F) =$ constant. Without any loss of generality, it can be assumed that $z_p = +d$ and $z_n = -d$, where d is real and positive. Streamlines are thus given by

$$\text{Arg}\left\{\frac{z-d}{z+d}\right\} = \frac{2\pi\psi}{q} = \beta = \text{constant}, \tag{3.2}$$

where ψ is the value of the streamfunction and $-\pi < \beta \leq \pi$. It is useful to write (3.2) as

$$\text{Arg}\left\{|z|^2 - d^2 + 2idy\right\} = \beta, \tag{3.3}$$

which shows that $\beta = 0$ corresponds to the streamlines at $y = 0$ for $|x| > d$, and that $\beta = \pi$ corresponds to the streamline at $y = 0$ for $|x| < d$. In addition, Eq. (3.2) shows that sign(β)=sign(y) for $y \neq 0$. As long as $\beta \neq 0$ or π, (3.3) can be written as

$$x^2 + (y - y_c)^2 = R^2, \tag{3.4a}$$

$$y_c^2 = d\cot\beta, \tag{3.4b}$$

$$R = d|\csc\beta|; \tag{3.4c}$$

that is, the streamline for a given value of β is an arc of the circle centered at $(0, y_c)$ with radius R. Several example streamlines are shown in Fig. 3.2. The flow is symmetric about

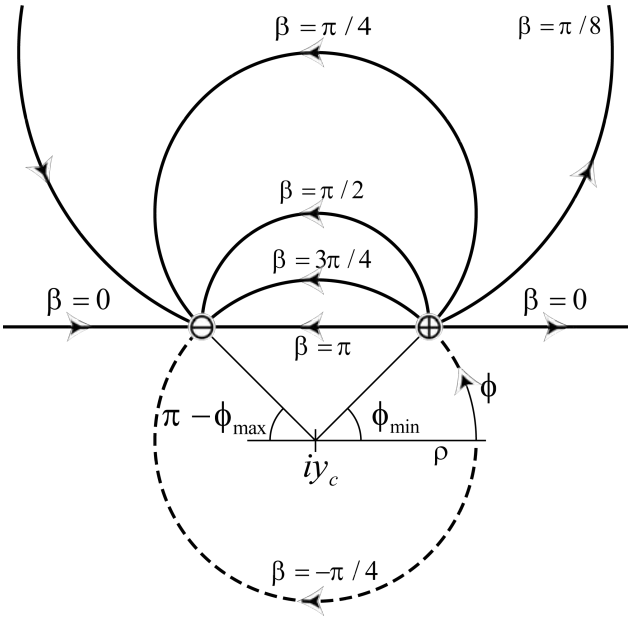

Figure 3.2: Sample streamlines labeled with the associated value of β. $\oplus$ and $\ominus$ represent a source and a sink, respectively. Arrow on streamline shows the direction of the motion along a streamline. Parameters defining streamline geometry are shown for $\beta = 3\pi/4$.

the x-axis, and thus the mathematical formulation can be derived for $y \geq 0$, $\beta \geq 0$ without any loss of generality. When a particle leaves the source, its trajectory has an initial slope given by

$$\frac{dy}{dx} = \frac{\pm d}{\sqrt{R^2 - d^2}} = \tan\beta, \tag{3.5}$$

where constant β defining a streamline has the physical interpretation of being the angle at which a particle on that streamline leaves the source. A particle on this same streamline will enter the corresponding sink at angle $\pi - \beta$. For a given value of β (assuming $\beta > 0$), the streamline extends from the source at ϕ_{min} to the sink at ϕ_{max}. If $0 < \beta < \pi/2$ so that $y_c > 0$, then the definition of y_c from (3.4b) and the geometry shown in Fig. 3.2 gives

$$\cot(-\pi/2 + \phi_{min}) = \frac{y_c}{d} = \cot\beta.$$

If $\pi/2 < \beta < \pi$ so that $y_c < 0$, then

$$\cot(\pi/2 - \phi_{min}) = \frac{|y_c|}{d} = -\cot\beta = \cot(\pi - \beta).$$

In both the cases the bounds on ϕ are

$$\phi_{min} = -\pi/2 + \beta. \tag{3.6a}$$

$$\phi_{max} = 3\pi/2 - \beta, \tag{3.6b}$$

showing that a particle travels through an angle $\triangle\phi = 2(\pi - \beta)$ as it moves from source to sink. The equation of motion for a passive particle in this flow is given by

$$\frac{d\overline{z}}{dt} = \frac{dF}{dz} = \frac{q}{2\pi}\left\{\frac{1}{z-d} - \frac{1}{z+d}\right\}, \tag{3.7}$$

where the overbar denotes complex conjugation. The particle at z is restricted to move along a streamline, so its position can be written as

$$z = iy_c + Re^{i\phi} \tag{3.8}$$

as long as $\beta \neq 0, \pi$. Substituting (3.8) into (3.7) yields, after some manipulation,

$$[R\sin\phi + y_c]\frac{d\phi}{dt} = \frac{q\ d}{2\pi R^2}. \tag{3.9}$$

Integration of (3.9) gives

$$y_c(\phi - \phi_0) - (x - x_0) = \frac{q\ d}{2\pi R^2}(t - t_0) \tag{3.10}$$

where $\phi_0 = \phi(t_0)$ and $x_0 = x(t_0)$. The time required for a particle to travel from the source to the sink along the streamline β is thus

$$T_\beta = \frac{4\pi R^2}{q}[(\pi - \beta)\cot\beta + 1]. \tag{3.11}$$

The left-hand side of (3.10) can be written as $\triangle G(\phi) = G(\phi) - G(\phi_0)$, where

$$G(\phi) = y_c\ \phi - R\cos\phi \tag{3.12}$$

is a one-to-one function over valid values of ϕ. A few illustrative examples are shown in Fig. 3.3. Thus, for $\phi_{min} \le \phi \le \phi_{max}$, (3.10) can be inverted to determine the displacement

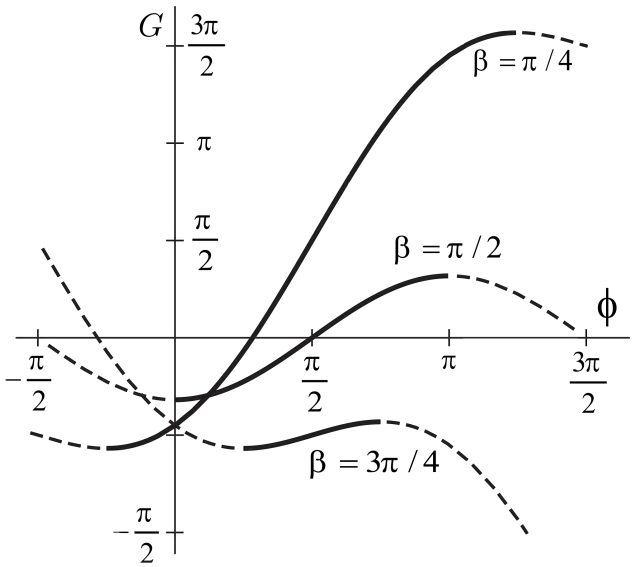

Figure 3.3: Plot of $G(\phi)$ for three streamlines. Solid lines show values for $\phi_{min} \le \phi \le \phi_{max}$.

of a particle during a time interval $\triangle t = t - t_0$. If $\beta = 0$ or π, the streamline is defined by $z = x$, and (3.7) gives

$$(x^2 - d^2)\frac{dx}{dt} = \frac{q\ d}{\pi}. \tag{3.13}$$

Integration of (3.13) shows that the position of a particle along the real axis is found by inverting (3.14),

$$\frac{1}{3}(x^3 - x_0^3) - d^2(x - x_0) = \frac{q\ d}{\pi}(t - t_0). \tag{3.14}$$

When $\beta = \pi$, the time taken by a particle to travel from the source at $x = d$ to the sink at $x = -d$ is

$$T_\pi = \frac{4\pi d^2}{3q}, \tag{3.15}$$

which is also the minimum time required for a particle to travel from the source to the sink. T_π is referred as the first breakthrough time in the ground water flow literature [15].

The total fluid injected (extracted) by a source (sink) in a source-sink pair is $A = q\ \triangle t$, where $\triangle t$ is time of the operation of the source-sink pair. If the flow were due only to the source, that area would be a circle with radius

$$\lambda = \sqrt{q\ \triangle t/\pi}.$$

When the flow is due to both a source and a sink, the value of the area is obviously different, as illustrated in Fig. 3.4; but λ still provides a useful length scale for describing the duration of a pulse. It is found that a circle with one source and one sink on its circumference divides the evolution of the fluid area into two equal parts. Thus, the area of fluid injected (or extracted) by source (or sink) inside the circular domain for a pulse time $\triangle t$ of a source-sink pair is $A = \frac{1}{2}Q\Delta t$.

It is convenient to consider the present problem in dimensionless form. Assume that there exists a characteristic length scale L for the system. In the case of a single source-sink pair, the obvious choice is $L = d$. For multiple pairs, the characteristic length may be different. Scaling all the lengths by L, i.e., setting $\delta = d/L$, $\eta_c = y_c/L$, $\rho = R/L$, and $\wedge = \lambda/L$; the

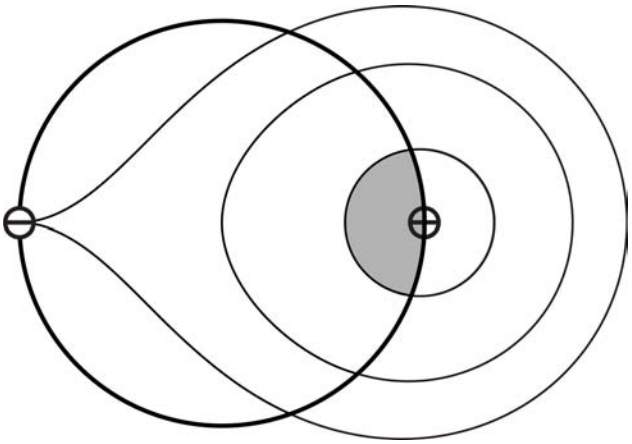

Figure 3.4: Evolution of a material line made up of fluid leaving the source at $t = 0$. Contours are shown for $t = \pi/10$, $\pi/2$ and π. The contour connecting to the sink shows the material line at $t = \pi$, the instant at which the particle traveling along the x axis reaches the sink. For the smallest contour, for $t = \pi/10$, the gray area indicates the area inside the circular domain. The gray area of and white sections are equal.

implicit equation for ϕ is

$$\eta_c\,(\phi - \phi_0) - \rho(\cos\phi - \cos\phi_0) = \frac{\delta\wedge^2}{2\rho^2}, \tag{3.16a}$$

$$\eta_c = \delta\cot\beta, \tag{3.16b}$$

$$\rho = \delta|\csc\beta|, \tag{3.16c}$$

when $0 < \beta < \pi$ and the implicit equation for $\xi = x/L$ is

$$\frac{1}{3}(\xi^3 - \xi_0^3) - \delta^2(\xi - \xi_0) = \delta\wedge^2, \tag{3.17}$$

when $\beta = 0$ or π. The appropriate choice of dimensionless time is $\tau = qt/\pi L^2$, thereby giving $\wedge^2 = \triangle\tau$. With the scaling, the dimensionless first breakthrough time is

$$\theta_\pi = 4\delta^2/3, \tag{3.18}$$

and the dimensionless time it takes for a particle with $0 < \beta < \pi$ to travel from source to sink is

$$\theta_\beta = 4\delta^2[(\pi - \beta)\cot\beta + 1]\csc^2\beta. \tag{3.19}$$

3.3 Source-sink pair in bounded domain

When two or more source-sink pairs are placed in a plane such that each of the sources and sinks are on a circle, then the circle is the only possible common streamline for those source-sink pairs when one source-sink pair is operated at a time. If the reinjection method is designed in such a way that it does not let the fluid cross the circle, then the circle can be considered as a boundary for the source-sink pair flow. Two such source-sink pair assemblies are shown in Fig. 3.5. Source $(z_+)_1$ and sink $(z_-)_1$ are operated together as SSSP1 and $(z_+)_2$ and $(z_-)_2$ as SSSP2. Fluid will slip along the boundary generated by the circular streamline. Fluid flow in the pulsed source-sink is the Hele-Shaw flow. So, it can be assumed that the flow starts and stops instantaneously when a source-sink pair is turned on or turned off. The possible streamlines owing to the steady operation of source-sink pairs are shown in Fig. 3.6. The solid streamlines are due to the steady operation of the SSSP1 and the dashed streamlines represent the streamlines owing to the steady operation of the SSSP2. One period of a pulsed source-sink consist of two pulses. During the first pulse, the SSSP1 operates for half of the period T and for the second pulse, the SSSP2 operates for other half T of the period, where $2T$ is the time period. A possible zig-zag motion of a fluid particle in the circular domain can be visualized through the alternating pulsed operation of SSSP1 and SSSP2.

In the protocols shown in Fig. 3.5, the fluid extracted through one of the holes, that makes a sink, can be reinjected either through the same hole or through a different hole. In the

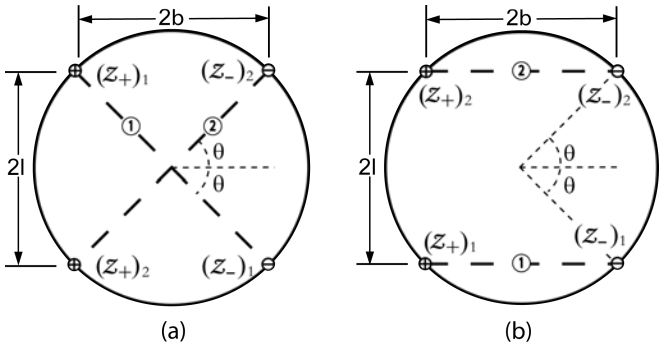

Figure 3.5: Domain geometry and locations of SSSPs with aspect ratio $l/b = tan(\theta)$. Sources are indicated by $\oplus$ and labeled with $(z_+)_i$ and sinks by $\ominus$ and labeled with $(z_-)_i$. A source and a sink connected by dashed line form a SSSP that operates together. Source $(z_+)_1$ and sink $(z_-)_1$ are operated together as SSSP1 and $(z_+)_2$ and $(z_-)_2$ as SSSP2. Fluid extracted at sinks $(z_-)_1$ and $(z_-)_2$ are reinjected at $(z_+)_2$ and $(z_+)_1$, respectively, in the consecutive pulse. (a) Crossed SSSP (X): Line joining the sources and sinks of each SSSPs are crosses at the center of the circular domain and (b) Parallel SSSP (P): Line joining the sources and sinks of each SSSPs are parallel to each other.

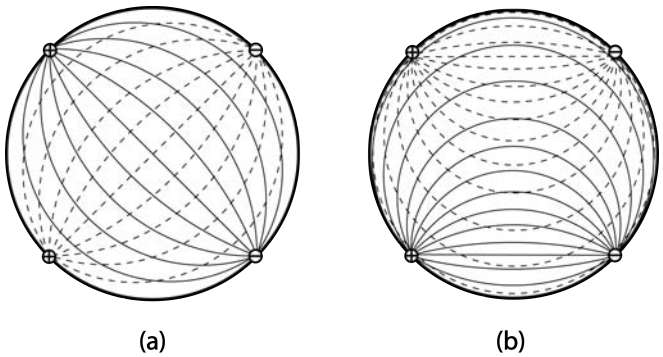

Figure 3.6: Sample streamlines generated by the steady operation of SSSPs. Solid lines are the possible streamlines due to steady operation of SSSP1 and dashed lines are due to steady operation of SSSP2. (a) Sample streamlines for configuration X and (b) sample streamlines for configuration P.

case when fluid is reinjected at the same hole, we do not need to transport the extracted fluid for reinjection. This hole is then referred to as "dynamic"; that is, the hole switches repeatedly between a source and a sink. A pulsed source-sink pair consisting of "dynamic" holes is referred to here as a "Dynamic Source-Sink Pair (DSSP)". Similarly, if fluid is only extracted (or reinjected) through a hole then the hole is "static". A pulsed source-sink pair

consisting of “static” holes is referred to here as a “Static Source-Sink Pair (SSSP)”.

3.4 Configurations with static source-sink pairs

This section discusses configurations consist of SSSP. In this system, fluid extracted through a sink requires to be relocated to corresponding source. Two different methods, “first-out, first-in” (FOFI) and “last-out, first-in” (LOFI) are considered for transporting the extracted fluid from a sink to corresponding source, as shown in Fig. 3.7. Figure 3.7 (a) shows a

Figure 3.7: “First Out, First In” and “Last Out, First In” method to transport extracted fluid from a source to a sink for reinjection.

schematic of the steps required for the “FOFI” reinjection scheme. In this method, fluid is extracted to a tube which is then flipped over to reinject the extracted fluid. “LOFI” reinjection scheme is again schematically shown in Fig. 3.7 (b). In “LOFI” method for fluid relocation, the extracted fluid in a tube is slid over for the reinjection without any flipping. The LIFO method can be implemented with a piston pump mechanism, as shown in Fig. 3.8. Two syringe pumps are used to design the “LOFI” relocation method. Each syringe with two valves connects a source of one source-sink pair to the sink of other source-sink pair . In Fig. 3.8, source A and sink B are operating as one source-sink pair and source C and sink D are operating as another source-sink pair . The FOFI method can be implemented by replacing the syringe with a positive displacement pump such as peristaltic pump is

shown in Fig. 3.9. Two different methods for reinjection of transported fluid are used in the present thesis. Relations between angle of extraction and angle of reinjected for each configuration are shown in Fig. 3.10. A particle extracted through sink, during pulse n, at time $(n-1)\alpha+\Delta$, will be reinjected through the appropriate source at time $(n+1)\alpha-\Delta$, where $0<\Delta<\alpha$ is the dimensionless time given for the particle to enter into sink during n^{th} pulse.

3.4.1 Regular motion with the "LOFI" reinjection scheme

In this section, the configurations RX and TP, shown in Fig. 3.10(a) and 3.10(d) with the "LOFI" reinjection scheme, are considered first. As shown below, in both the configurations all particle trajectories are regular.

Configuration RX

The schematic of the configuration RX is shown in Fig. 3.10(a). The extracted and reinjected particle positions are symmetric about y-axis, when using the "LOFI" reinjection scheme with configuration RX. Thus, a fluid particle at $z_{extracted}$ during the n^{th} pulse is reinjected to

$$z_{reinjected} = -\bar{z}_{extracted} \tag{3.20}$$

during the $(n+1)^{th}$ pulse. Figure 3.11 shows two representative particle trajectories. Let, "-0" denote the position of a fluid particle after the n^{th} pulse by SSSP1. It is assumed that the particle requires time Δt to get extracted through the sink during the $(n+1)^{th}$ pulse by SSSP2. If $\Delta t < T$, then the particle will be extracted during the $(n+1)^{th}$ pulse through the sink of SSSP2, and the particle will be reinjected to "+0" during the $(n+1)^{th}$ pulse by SSSP1, as shown in Fig. 3.11.

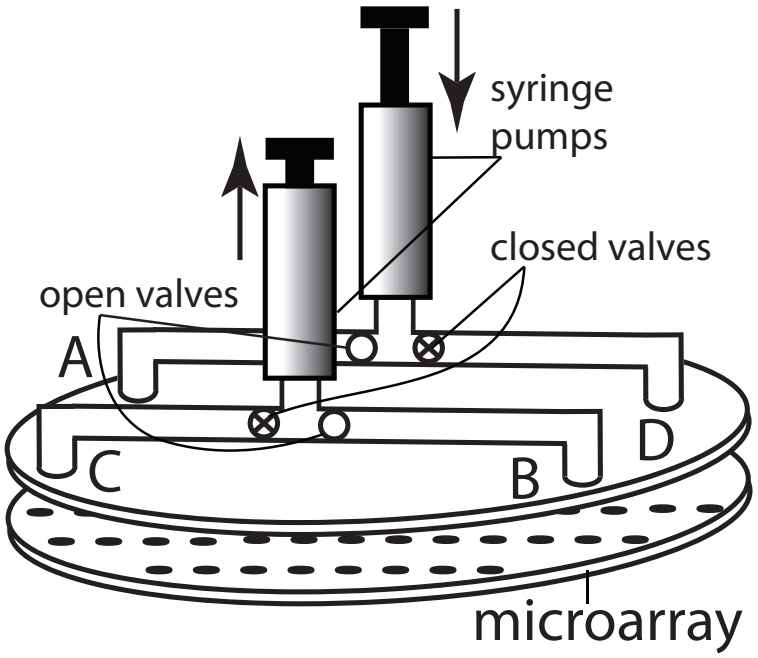

Figure 3.8: Schematic of a pulsed source-sink chamber with external fluidic control with syringe system. Presented configuration has a source at A and a sink at B. Figure shows one of the operating mode. Operating in this mode for time T is the first half of the cycle. Valve states switch by reversing syringe pumps operation for the second half of the cycle. For the second half of the cycle C operates as source and D as sink. Fluid extracted from B is re-injected at C, and fluid extracted from D is re-injected at A.

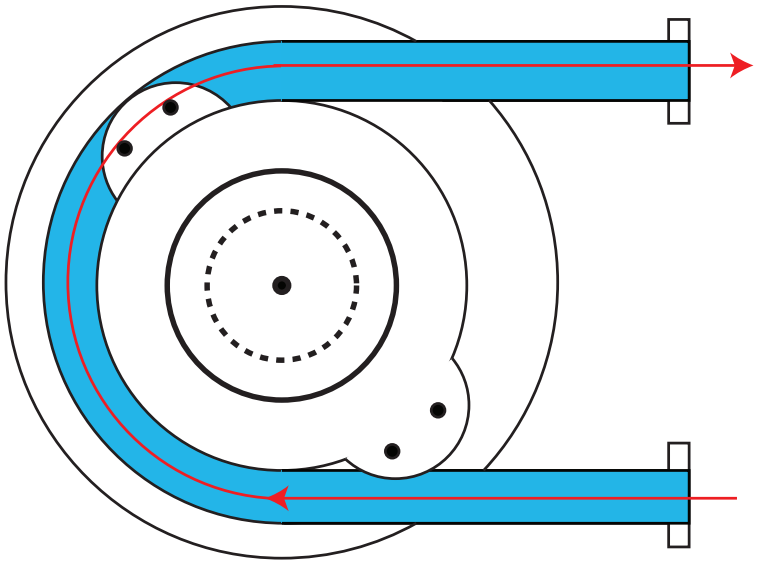

Figure 3.9: Peristaltic pump for the fluid transportation from sink to the corresponding source.

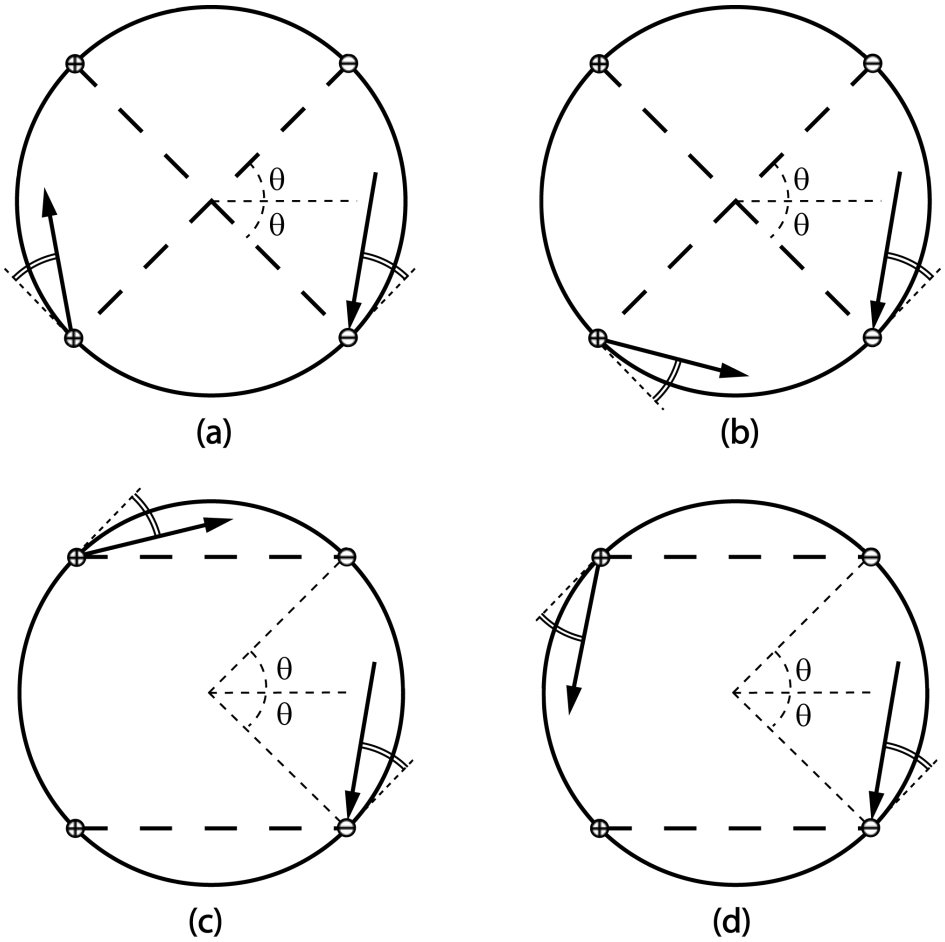

Figure 3.10: Relation between the extraction and reinjection angles. The lines with arrow shows the direction at which a particle gets extracted / reinjected. (a) Configuration RX, (b) configuration TX, (c) configuration RP, and (d) configuration TP.

Owing to the symmetry of the flow, the positions of "-0" and "+0" are mirror images of each other about the y-axis. Let the particles at "+0" and "-0" move forward and backward in time, respectively. Here, solid and dashed curves in Fig. 3.11 represent trajectories of particles moving forward and backward in time, respectively. A black dot labeled with a negative number represents a particle position during a pulse backward in time, and a white dot labeled with a positive number represents a particle position during a pulse forward in time. In configuration RX, the source-sink pairs of equal strength are located with positions mirror image of each other. So, positions of the particles at $0+$ and $0-$ during k^{th} forward

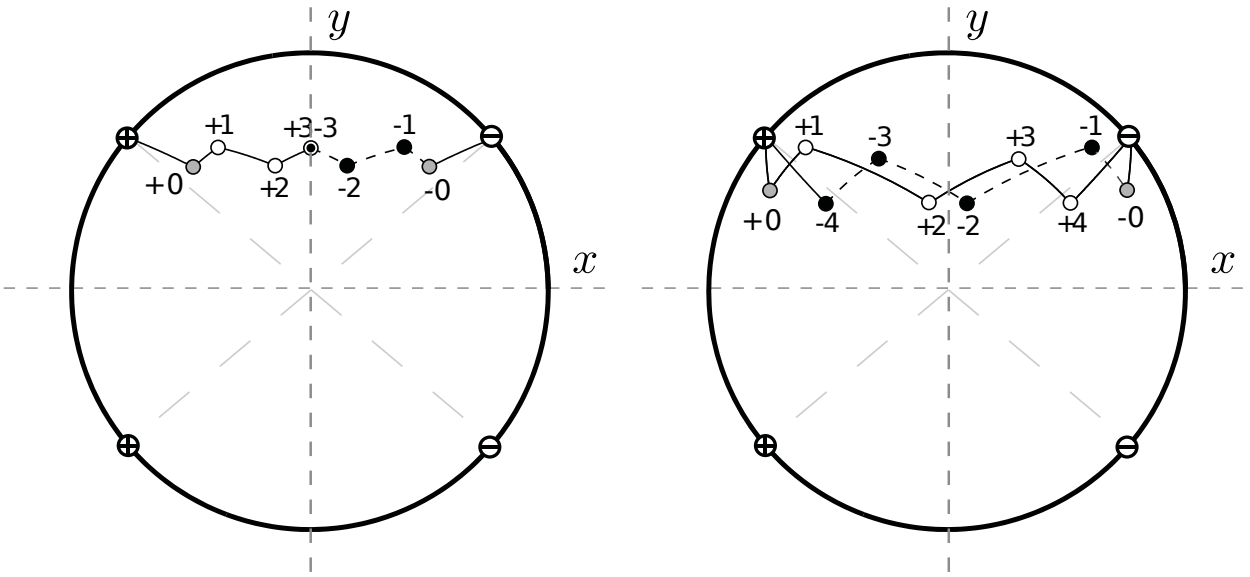

Figure 3.11: Trajectory of a fluid particle for configuration RX using "LIFO" reinjection scheme. (a) Particle maps to the vertical line passing through the center of the domain after n^{th} pulse, where $n = 1\ , 2, \ldots$ and (b) particle does not map to the y-axis.

and backward pulse, respectively, are related as

$$z_{-k} = -\bar{z}_{+k} \tag{3.21}$$

where z_{+k} and z_{-k} are positions of particles during k^{th} pulse in forward and backward, respectively, and $k = 0, 1, 2, \ldots, n$.

A fluid particle will have a periodic trajectory only when one (or more) of Eqs. (3.22), (3.23), or (3.24) is/are true.

$$z_{-n} = z_{+n} \tag{3.22}$$

$$z_{-n} = z_{+(n+1)} \tag{3.23}$$

$$z_{-(n+1)} = z_{+n} \tag{3.24}$$

Equation (3.22) can only be true when $real(z_{-n}) = real(z_{+n}) = 0$ which is shown in

Fig. 3.11(a) with $n = 3$.

If a particle moving forward in time gets extracted during n^{th} pulse, then it gets re-injected at $z_{+(n+1)} = -\overline{z_{+n}}$ during $(n+1)^{th}$ pulse. Positions of particles moving forward and backward in time are related as in Eq. (3.20). So, the position of the particle during $(n+1)^{th}$ pulse is $z_{+(n+1))} = -\overline{(-\overline{z_{-n}})} = z_{-n}$ is equivalent to Eq. (3.23). Similarly, position of a particle, moving backward in time, during $(n+1)^{th}$ pulse is $z_{-(n+1))} = -\overline{(-\overline{z_{+n}})} = z_{+n}$ is equivalent to Eq. (3.24). Figure 3.11(b) shows the periodic trajectory for fluid particles satisfying Eqs. (3.23) and (3.24) with $n = 4$.

Thus, a particle trajectory for configuration RX with "LOFI" reinjection scheme satisfies all the conditions required for a periodic solution with arbitrary initial condition, without the occurrence of any chaos in the system.

Configuration TP

A schematic of the configuration TP is shown in Fig. 3.10(d). Figure 3.12 shows representative particle trajectories. Owing to the symmetry of the flow, a fluid particle at $z_{extracted}$ that is extracted during the n^{th} pulse is reinjected to

$$z_{reinjected} = -z_{extracted} \tag{3.25}$$

during the $(n+1)^{th}$ pulse for configuration TP using the "LOFI" reinjection scheme. Let "-0" denote the position of a fluid particle after the n^{th} pulse by SSSP1. It is assumed that the particle requires Δt time to get extracted through the sink during $(n+1)^{th}$ pulse by SSSP2. If $\Delta t < T$, where T is the pulse time, then the particle will be extracted during the $(n+1)^{th}$ pulse through the sink of SSSP2, and the particle will be reinjected to "+0" during $(n+1)^{th}$ pulse by SSSP1, as shown in Fig. 3.12.

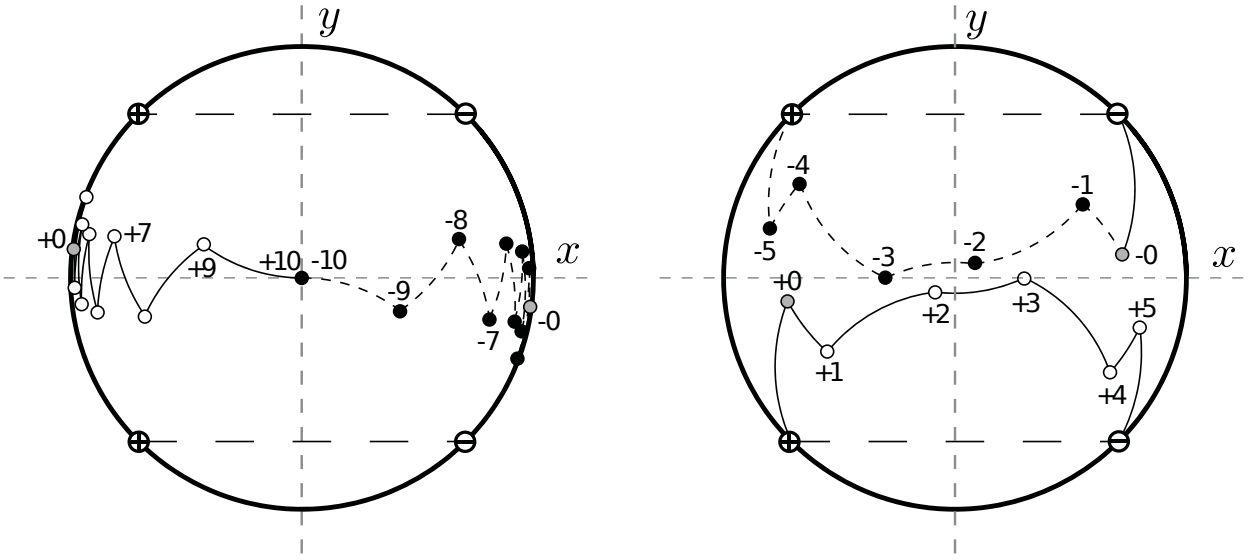

Figure 3.12: Periodic trajectories of fluid particles for configuration TPL. (a) When particle maps to y-axis and (b) when particle does not map to y-axis.

Let the particles at "+0" and "-0" move forward and backward in time, respectively. Solid and dashed curves in Fig. 3.12 represent trajectories of particles moving forward and backward in time, respectively. A black dot labeled with a negative number represents a particle position during a pulse backward in time and a white dot labeled with a positive number represents a particle position during a pulse forward in time. In configuration TP, the position of the source-sink pairs of equal strengths are mirror images of each other about the $x-$axis. So, positions of the particles at $0+$ and $0-$ during k^{th} forward and backward pulse, respectively, are related as

$$z_{-k} = -z_{+k} \tag{3.26}$$

where z_{+k} and z_{-k} are positions of particles in forward and backward time, respectively, and $k = 0, 1, 2, \ldots, n$.

A fluid particle will have a periodic trajectory only when the particle moves on a fixed trajectory, which can be defined in terms of mathematical equations Eqs. (3.22), (3.23), or (3.24). Combination of Eqs. (3.22) and (3.26) for $n = k = n1$, shows that the condition

is only true when a particle maps to the origin for some value of $n1$. This is shown in Fig. 3.12(a) with the value $n1 = 10$.

If a particle moving forward in time gets extracted during n^{th} pulse, then using Eq. (3.25), it will be re-injected at $z_{+(n+1)} = -z_{+n}$ during $(n+1)^{th}$ pulse. Substituting the value of z_{+n} from Eq. (3.26) for $k = n$, $z_{+(n+1)} = -z_{+n} = -(-z_{-n}) = z_{-n}$ which is the condition required for the regular trajectory defined as Eq. (3.23). In the same way, a particle moving backward in time that gets extracted during the n^{th} pulse will be re-injected at $z_{-(n+1)} = -z_{-n}$ during the $(n+1)^{th}$ pulse. Using Eq. (3.26) for $k = n$, gives $z_{-(n+1)} = -z_{-n} = -(-z_{+n}) = z_{+n}$, which is also the condition required for the regular trajectory given in Eq. (3.24). Figure 3.12(b) shows the periodic trajectory for fluid particles satisfying Eqs. (3.23) and (3.24) with the value $n = 5$.

Thus, a particle trajectory for configuration TP with "LOFI" reinjection gives periodic solutions for all initial conditions, and there is no chaos in the system.

3.4.2 Chaotic motion with the "LOFI" reinjection scheme

Numerical simulation shows that configurations TX and RP, shown in Fig. 3.10(b) and 3.10(c), generate chaotic trajectories of a fluid particle in a fraction of the domain for various values of α and θ using "LOFI" reinjection scheme.

Configuration TX

A schematic of the configuration TX is shown in Fig. 3.10(b). It shows the orientations of the static source-sink pairs in the domain and the relation between the angle of extraction and reinjection of a fluid particle. Poincaré sections are generated by recording the position

of a passive particle in the domain after every period of operation. A detailed description of the Poincaré section is given in section 2.5. Figure 3.14 shows a table of the Poincaré sections for configuration TX with "LOFI" reinjection scheme for various values of α and θ. For small value of α pulsed operation of this system is close to steady operation of SSSPs resulting division of fluid in the domain into two sections as shown in Fig. 3.13. Thus, fluid

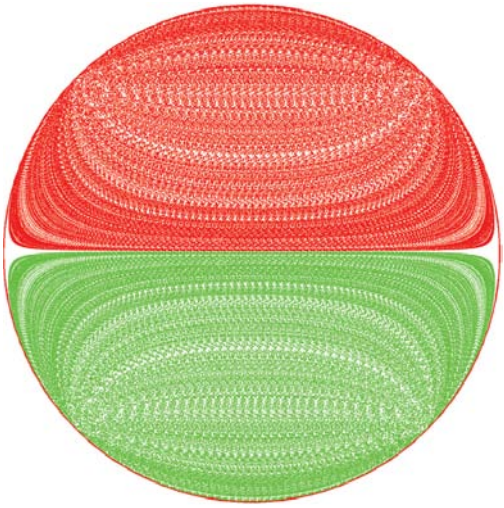

Figure 3.13: Poincaré section for the configuration TX using "LIFO" reinjection scheme, $\alpha = 1\%$, and $\theta = 45^o$.

particle with an initial condition in the green (or the red) section moves all over in the green (or the red) section only. For $\alpha \geq 10\%$ there is no fluid division in the domain and one chaotic region occupies a fraction of the domain. For $\alpha \geq \alpha_{cr}^{TXL}$ a circular elliptic island exists in the domain of the system, where $\alpha_{cr}^{TXL} = 100/3\%$ is the time required for a fluid particle at the center of the domain to get extracted in one pulse. For higher values of α, radius of the island at the center of the domain increases.

Plots for μ_s, Lyapunov exponent λ and the Kolmogrov entropy h_{KS} are shown in Figs. 3.15, 3.16, and 3.17, respectively. Figure 3.16 shows a plot of Lyapunov exponent for various value of α and θ. The values of Lyapunov exponent for small values of α are relatively higher than the values of Lyapunov exponent for higher values of α.

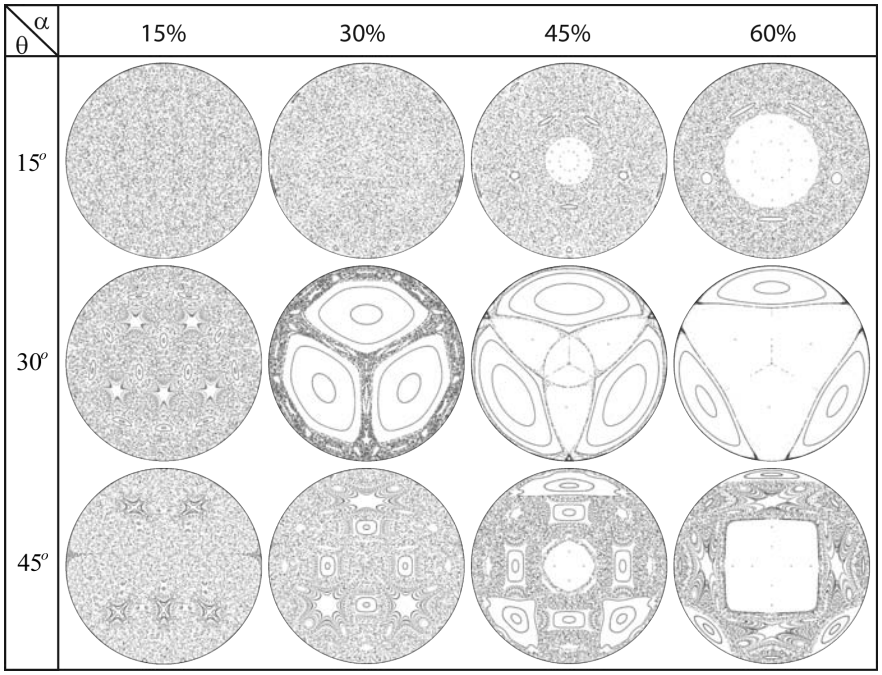

Figure 3.14: Tabulated Poincaré sections for the configuration TX using "LIFO" reinjection scheme (TXL).

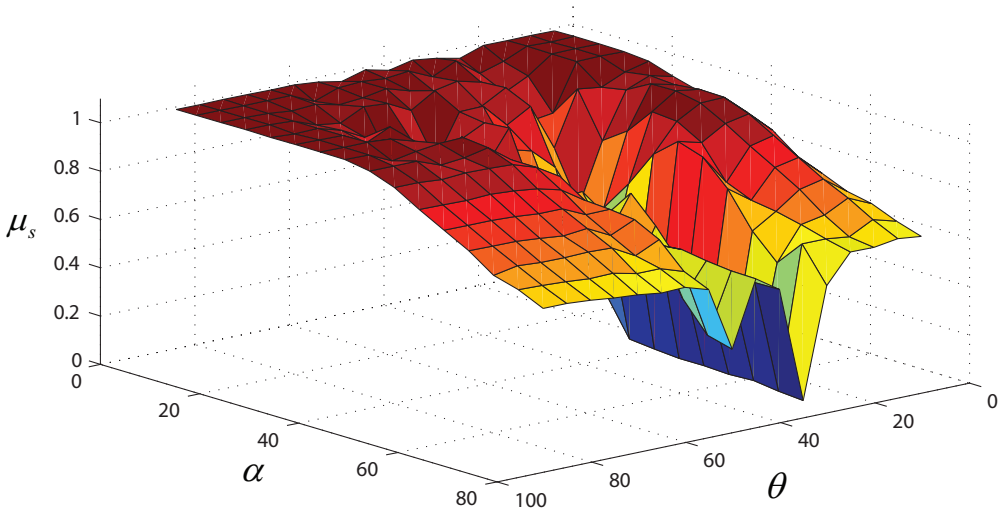

Figure 3.15: Variations of μ_s with α and θ for configuration TXL.

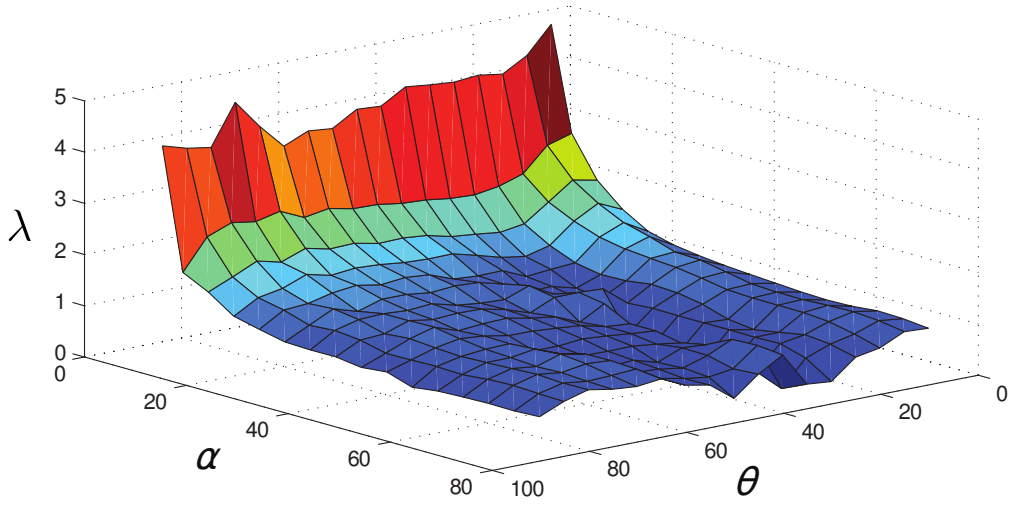

Figure 3.16: Variations of λ with α and θ for configuration TXL.

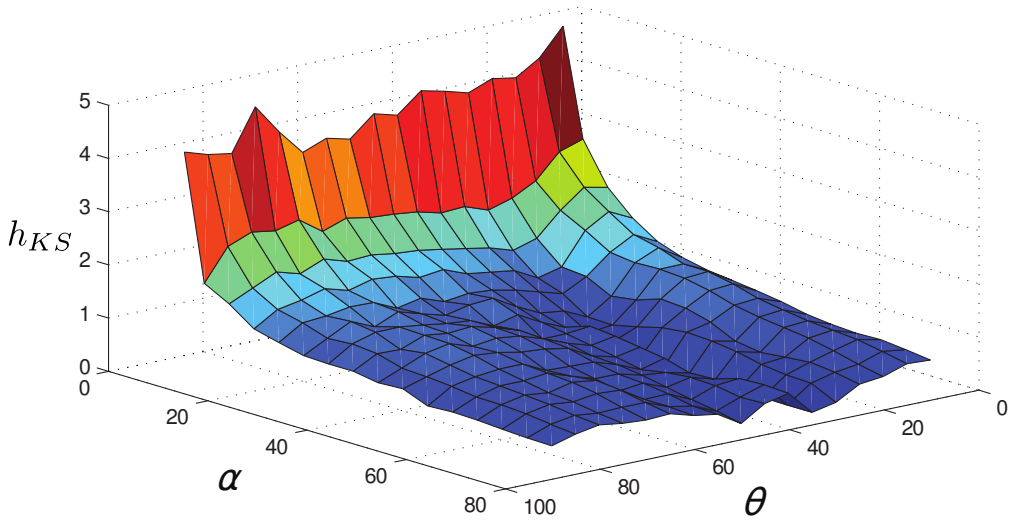

Figure 3.17: Variations of h_{KS} with α and θ for configuration TXL.

Relocation of extracted fluid from a sink to a source using "LOFI" (or "FOFI") relocation adds a delay time to the system. The delay time required for fluid relocation is independent of the pulse time. To practically implement the system, a delay time $\alpha_d = 10\%$ is considered for the fluid relocation. With the consideration of the delay time, an effective pulse time for the system can be defined as $\alpha_e = \alpha + \alpha_d$. Considering the delay time reduces the value of the Lyapunov exponent and the KS entropy as shown in Figs. 3.18 and 3.19, respectively. The

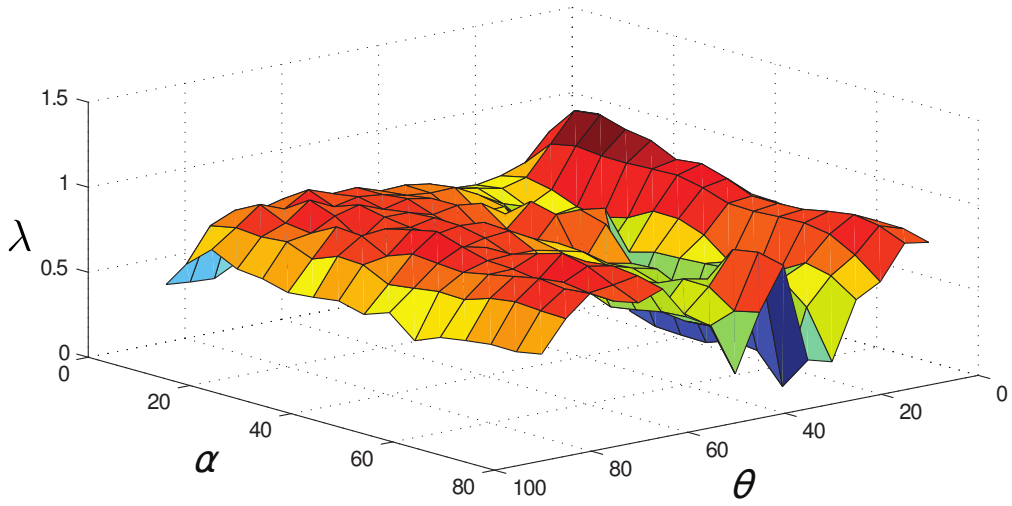

Figure 3.18: Plot for λ with α and θ for configuration TXL.

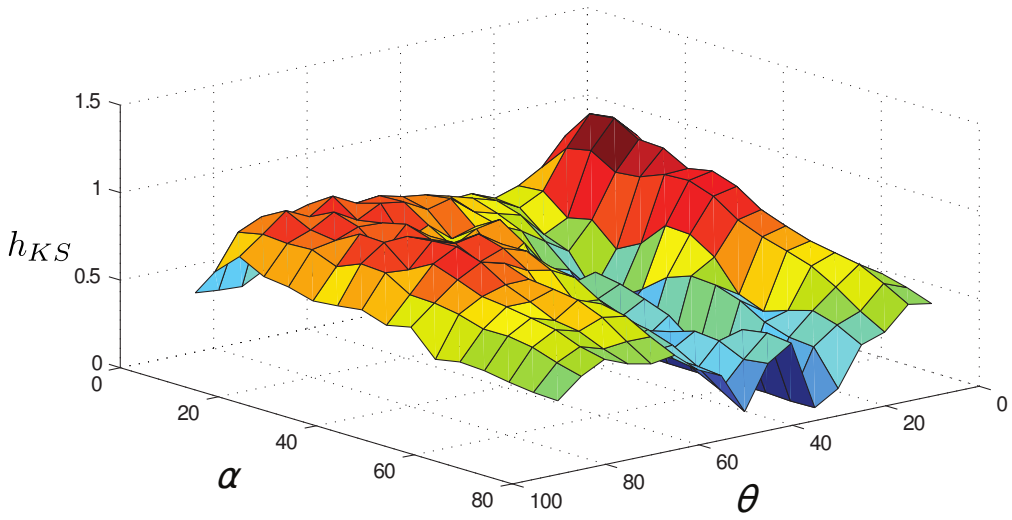

Figure 3.19: Plot for h_{KS} with α and θ for configuration TXL.

maximum value of KS entropy in Fig. 3.19 is $h_{KS} \approx 1$ for $5\% \leq \theta \leq 20\%$ and $10^o \leq \alpha \leq 20^o$.

Configuration RP

A schematic of the configuration RP is shown in Fig. 3.10(c). The orientation of the static source-sink pairs in the domain and the relation between extraction and reinjection angle are shown. Poincaré sections are generated by recording the position of a passive fluid particle in the domain after every period of operation. A set of Poincaré sections are shown in Fig. 3.20 for various values of α and θ. Plots for μ_s, Lyapunov exponent λ, and KS entropy h_{KS} are

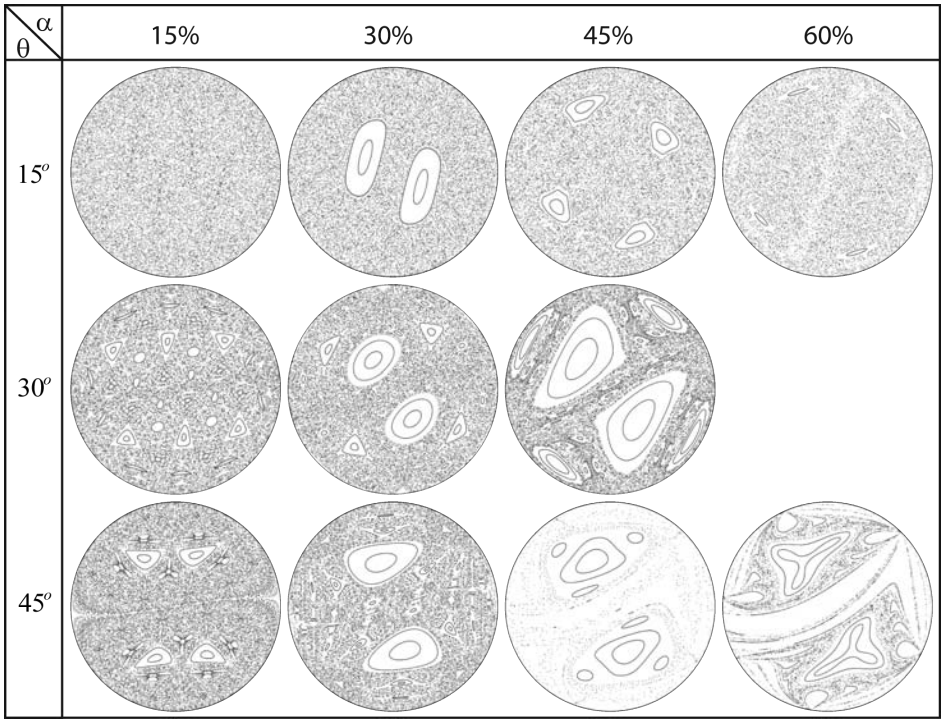

Figure 3.20: Poincaré sections for the configuration RP using LIFO reinjection (RPL).

shown in Figs. 3.21, 3.22, and 3.23, respectively. ‘ The value of Lyapunov exponent and KS entropy is high for small value of α and θ. Considering a delay time $d\alpha = 10\%$ for practical implementations, Lyapunov exponent and KS entropy are computed with effective pulse time $\alpha_e = \alpha + \alpha_d$. Plots for the Lyapunov exponent and the KS entropy with effective

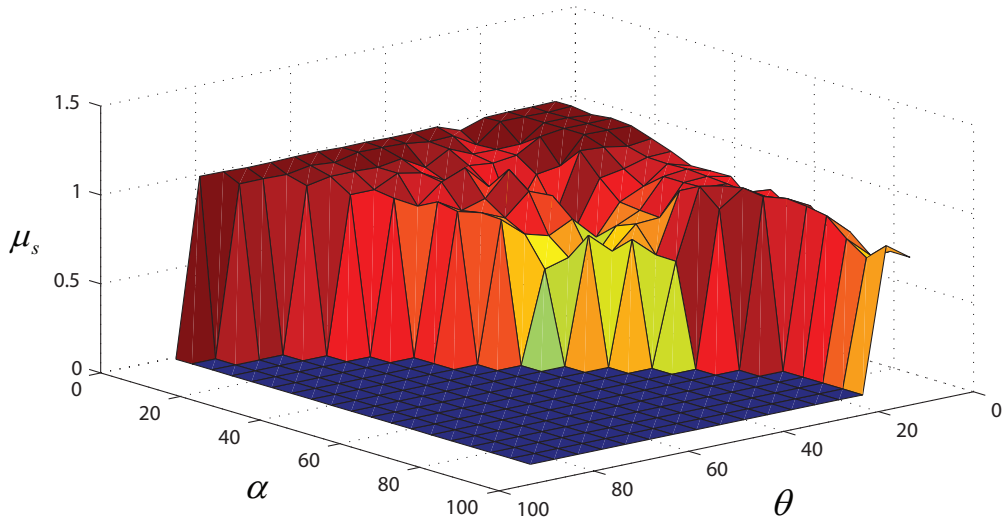

Figure 3.21: Variations of μ_s with α and θ for configuration RPL.

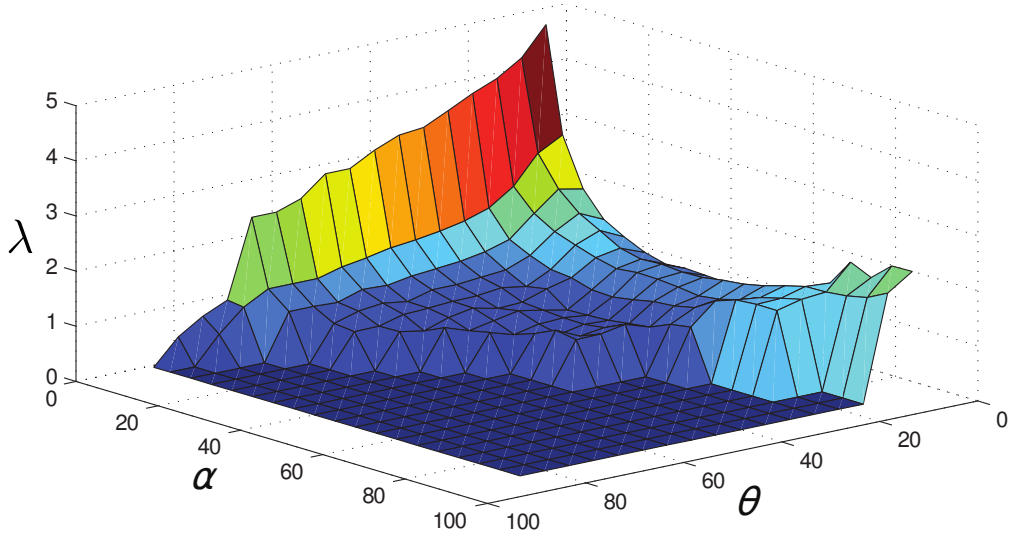

Figure 3.22: Variations of λ with α and θ for the configuration RPL.

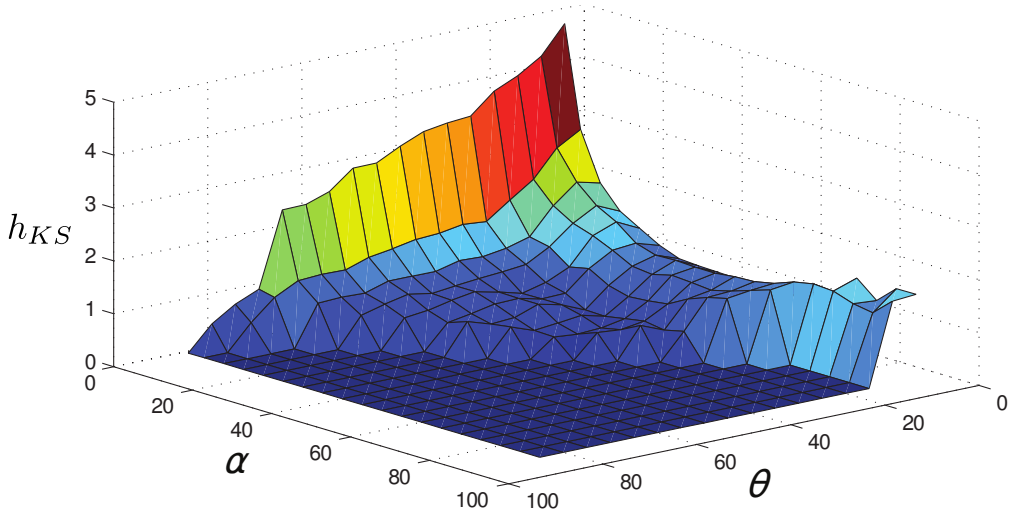

Figure 3.23: Variations of h_{KS} with α and θ for the configuration RPL.

pulse time are as shown in Figs. 3.18 and 3.19, respectively. The maximum value of KS

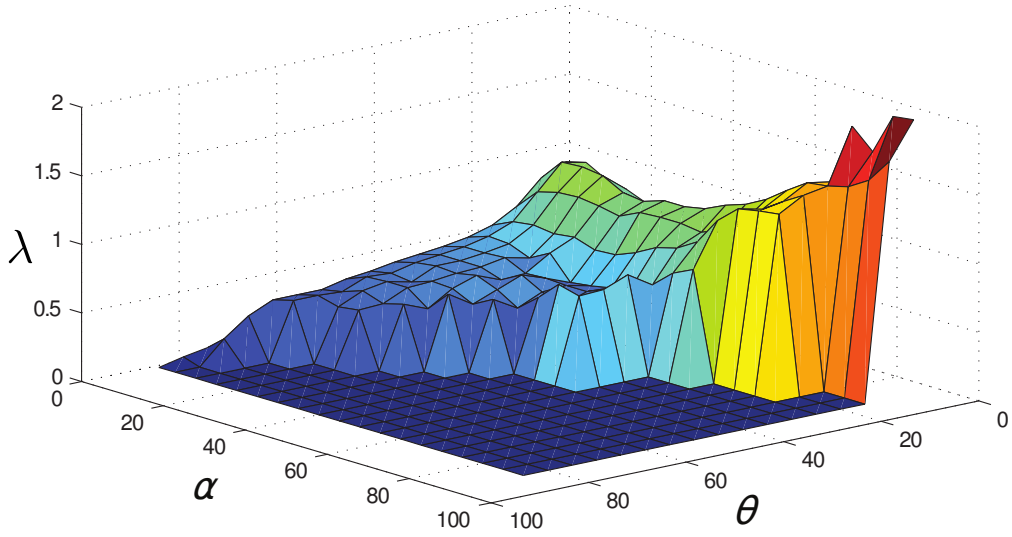

Figure 3.24: Variations of λ using effective α_e with α and θ for the configuration RPL.

entropy in Fig. 3.19 is $h_{KS} \approx 1.5$ for $10^o \leq \theta \leq 20^o$ and $80\% \leq \alpha \leq 90\%$.

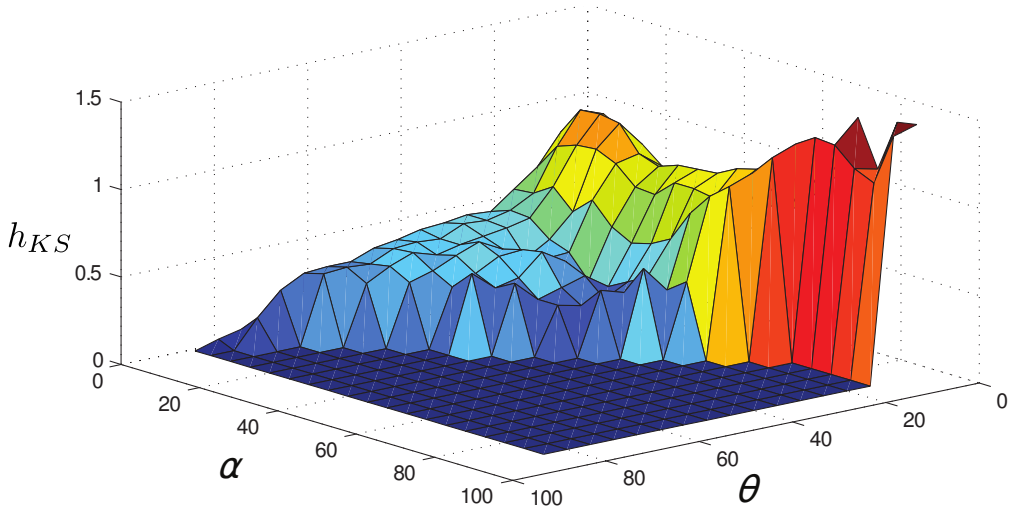

Figure 3.25: Variations of h_{KS} using effective α_e with α and θ for the configuration RPL.

3.4.3 "FOFI" reinjection scheme

Pulsed operation of the source-sink configurations, shown in Fig. 3.10, with "LIFO" reinjection scheme are analyzed in sections 3.4.1 and 3.4.2. Using "LIFO" relocation scheme, a fluid particle extracted through a sink in time t during n^{th} pulse (i.e. $t < T$) is reinjected through a source for time t during $(n+1)^{th}$ pulse. With "FOFI" reinjection scheme, a fluid particle extracted during n^{th} pulse for time $t < T$, is reinjected through a source for time $(T-t)$ during $(n+1)^{th}$ pulse. Practically the "FOFI" relocation method can be implemented with a positive displacement pump like peristaltic pump shown in Fig. 3.9.

Configuration RX

A schematic of the configuration is shown in Fig. 3.10(a) showing the position of the static source-sink pairs in the domain and the relation between the angle of extracted and reinjected fluid particle. A Poincaré section is computed by plotting position of a fluid particle after every period of operation. A set of Poincaré sections for the system are shown in Fig. 3.26 for various values of α and θ. Plots for μ_s, Lyapunov exponent λ and KS entropy h_{KS} are shown in Figs. 3.27, 3.28, and 3.29, respectively. Considering a delay time $d\alpha = 10\%$ for practical implementation, the values of Lyapunov exponent and KS entropy decrease for small values of α as explained in Section 3.4.2. Comparatively high values of KS entropy $h_{KS} \approx 2.5$ is for $10^o \leq \theta \leq 20^o$ and $60\% \leq \alpha \leq 70\%$

Configuration TX

A schematic of the configuration is shown in Fig. 3.10(b) showing the position of the static source-sink pairs in the domain. Figure 3.10(b) also shows the relation between angle of ex-

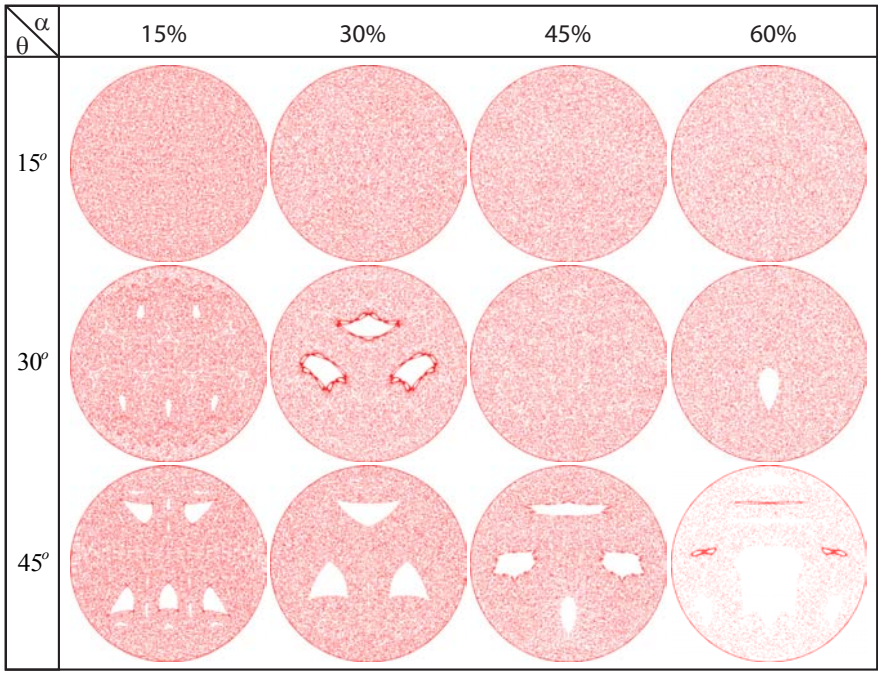

Figure 3.26: Poincaré sections for configuration RX. Extracted fluid through a sink is reinjected through a source using FOFI reinjection scheme.

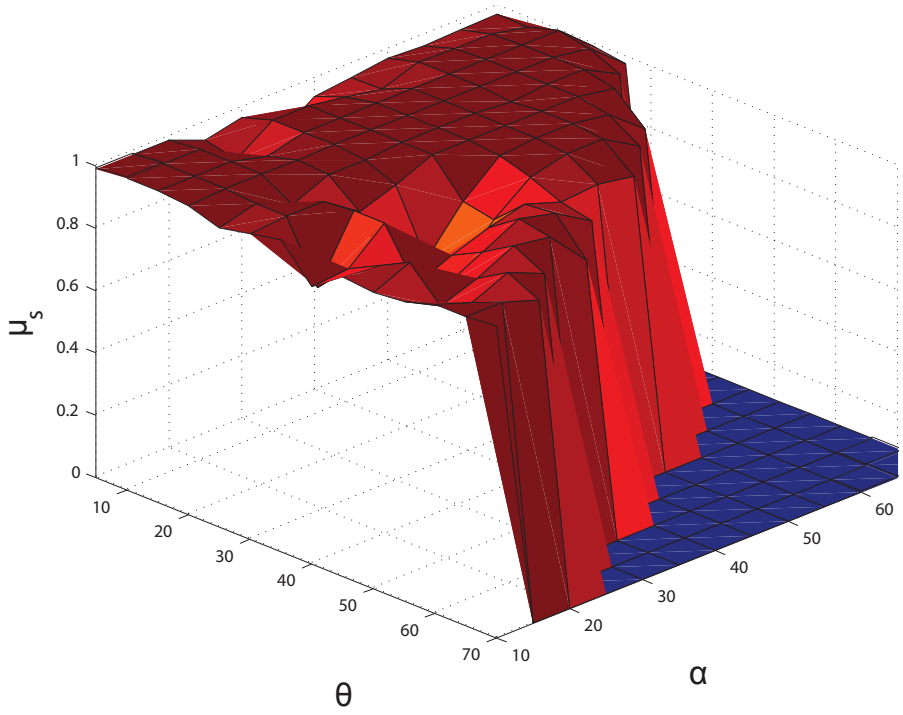

Figure 3.27: μ_s for configuration RX using FIFO reinjection scheme.

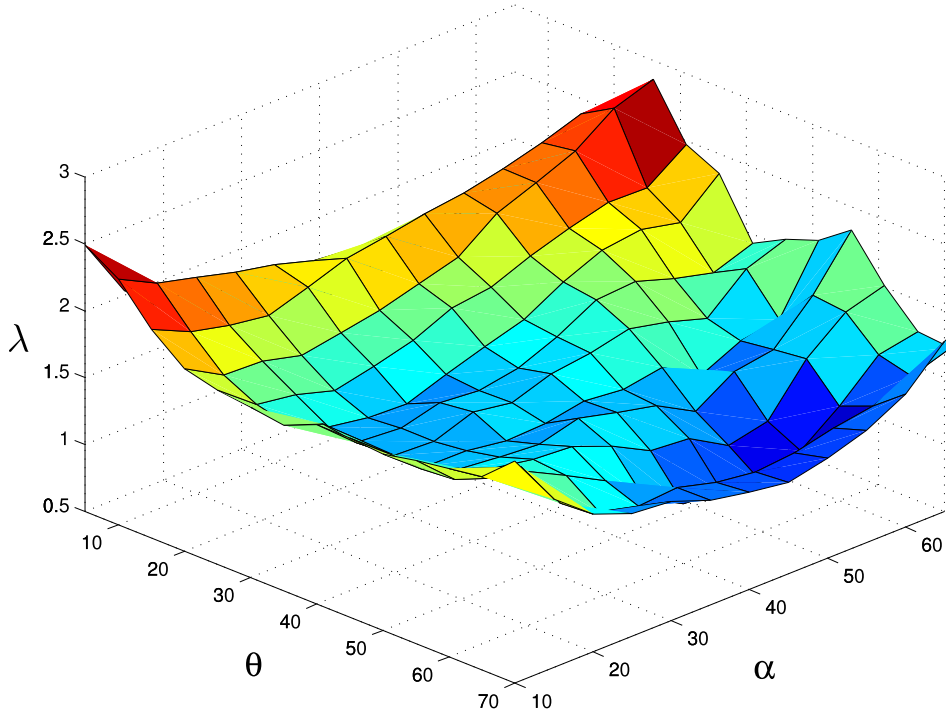

Figure 3.28: Lyapunov exponent for configuration RX using FIFO reinjection scheme.

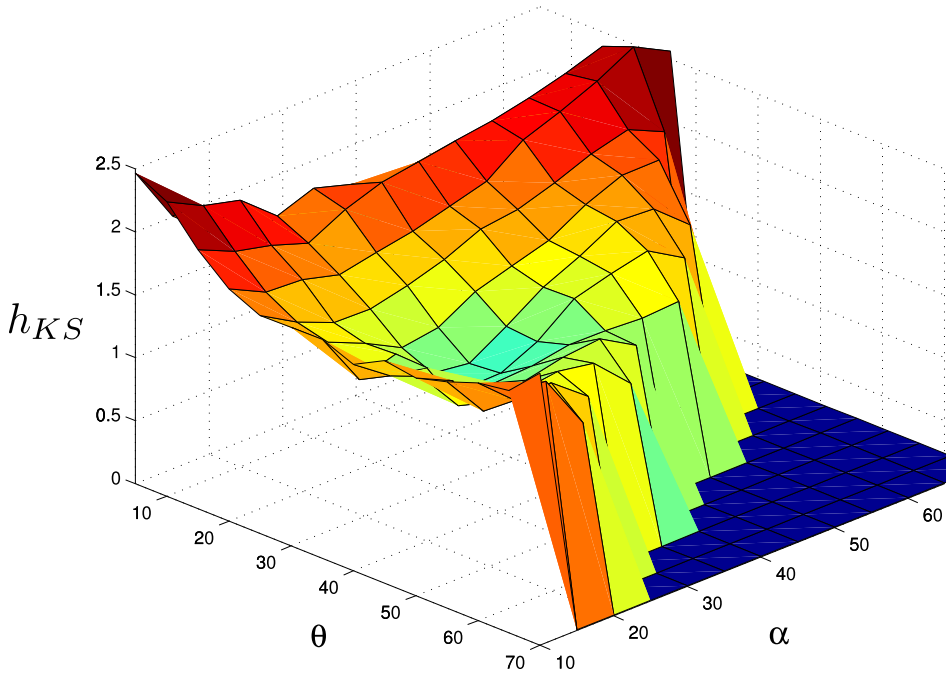

Figure 3.29: KS entropy for configuration RX using FIFO reinjection scheme.

traction and reinjectin of a passive fluid particle. A Poincaré section is plotted by computing position of a passive fluid particle after every period of time 2α. Chaos is observed in some part of the domain as shown in Fig. 3.30. Plots for μ_s, Lyapunov exponent λ and KS entropy

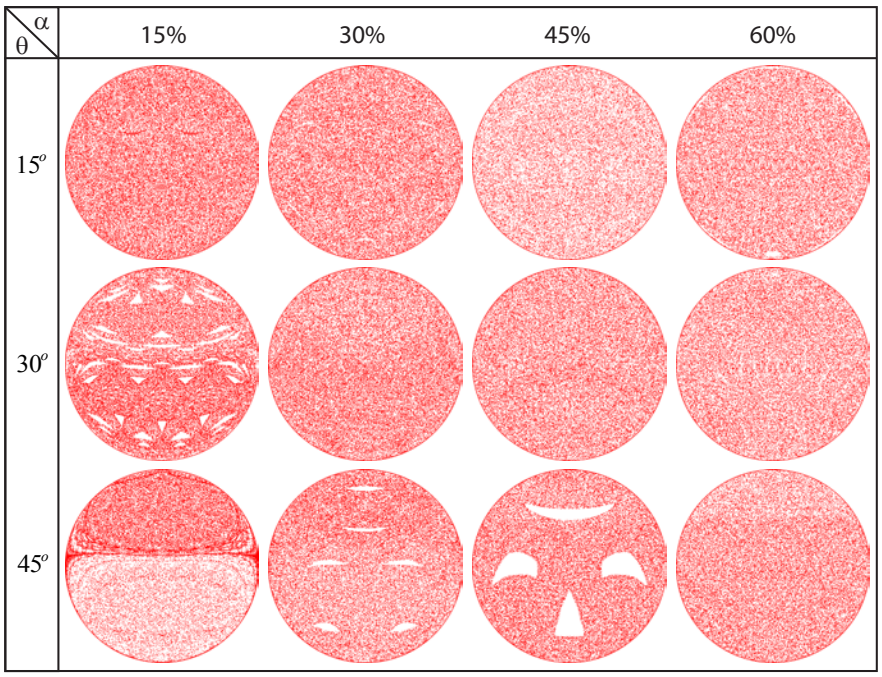

Figure 3.30: A set of Poincaré section for configuration TX using FIFO relocation scheme.

h_{KS} are shown in Figs. 3.31, 3.32, and 3.33, respectively. Once again the KS entropy for small values of α can be considered for the practical implementation of the system. Practical implementation of the system requires fluid relocation time from a sink to a source. The relocation time $d\alpha = 10\%$ can be considered as a delay time in the system which decreases the value of the Lyapunov exponents and the KS entropy in the system for small values of α. With the consideration of the delay time, the highest value of the KS entropy $h_{KS} \approx 2.5$ is for $25^o \leq \theta \leq 40^o$ and $55\% \leq \alpha \leq 65\%$.

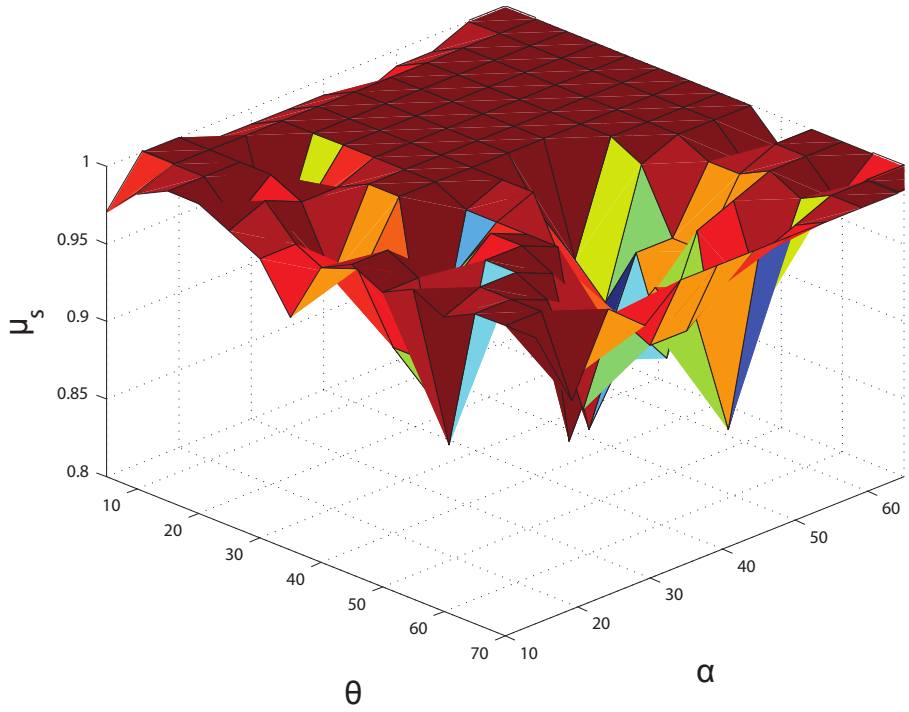

Figure 3.31: μ_s for configuration TX using FIFO relocation scheme.

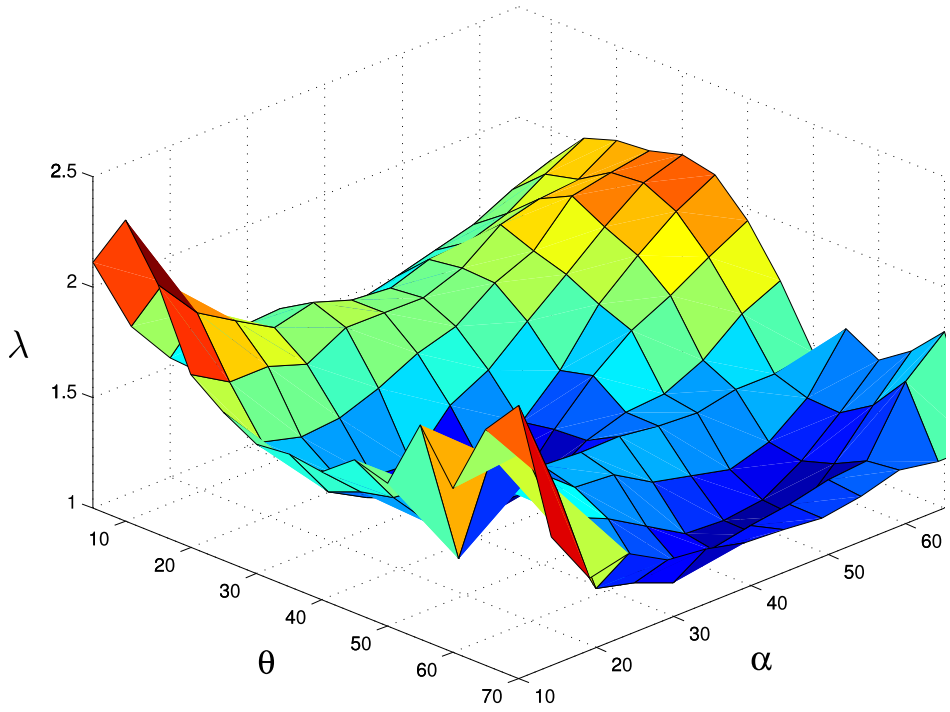

Figure 3.32: Lyapunov exponent for configuration TX using FIFO relocation scheme.

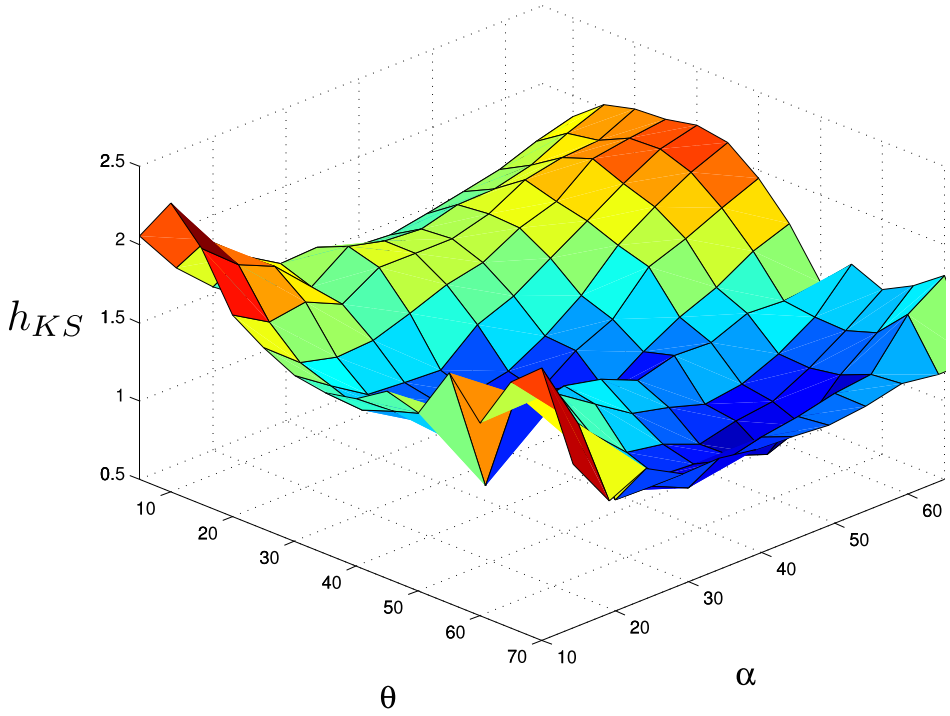

Figure 3.33: KS entropy for configuration TX using FIFO relocation scheme.

Configuration RP

A schematic of the configuration RP is shown in Fig. 3.10(c) to explain the position of static source-sink pairs in the domain and the relation between angle of extraction and reinjection for a fluid particle. Poincaré sections are plotted for various values of α and θ by computing the position of a passive fluid particle in the domain. Tabulated plots for Poincaré sections are shown in Fig. 3.34 for various values of α and θ. Plots for μ_s, Lyapunov exponent λ and KS entropy h_{KS} are shown in Figs. 3.35, 3.36, and 3.37, respectively. The KS entropy for small values of α can be avoided for the practical implementation as explained in Section 3.4.2. Comparatavely high value of KS entropy $h_{KS} \approx 2.5$ is for $5^o \leq \theta \leq 20^o$ and $55\% \leq \alpha \leq 65\%$.

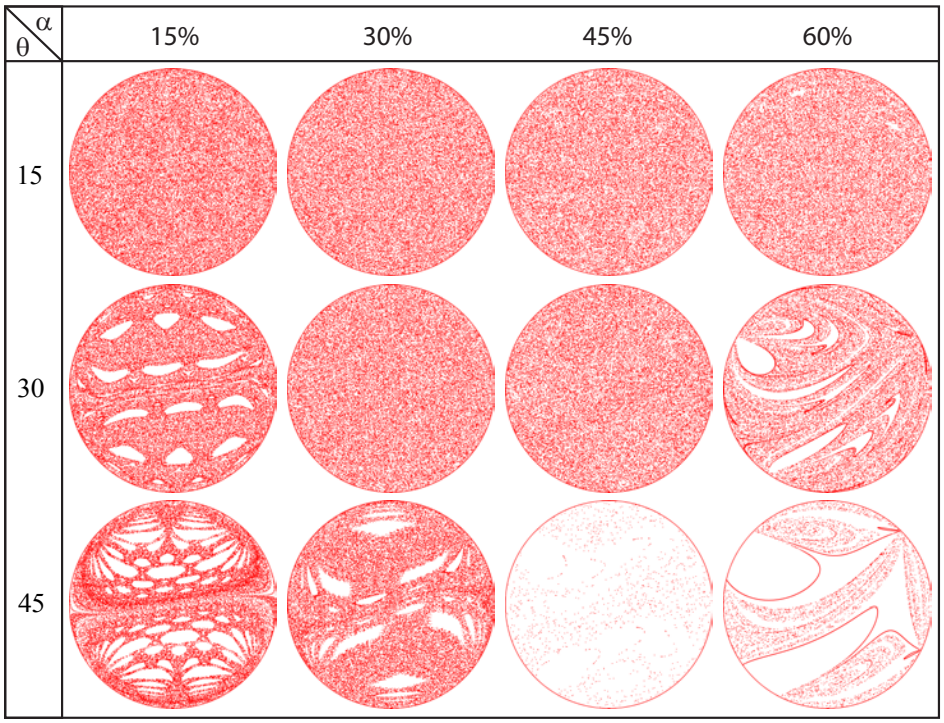

Figure 3.34: Poincaré sections for configuration RP with FIFO relocation scheme (RPF).

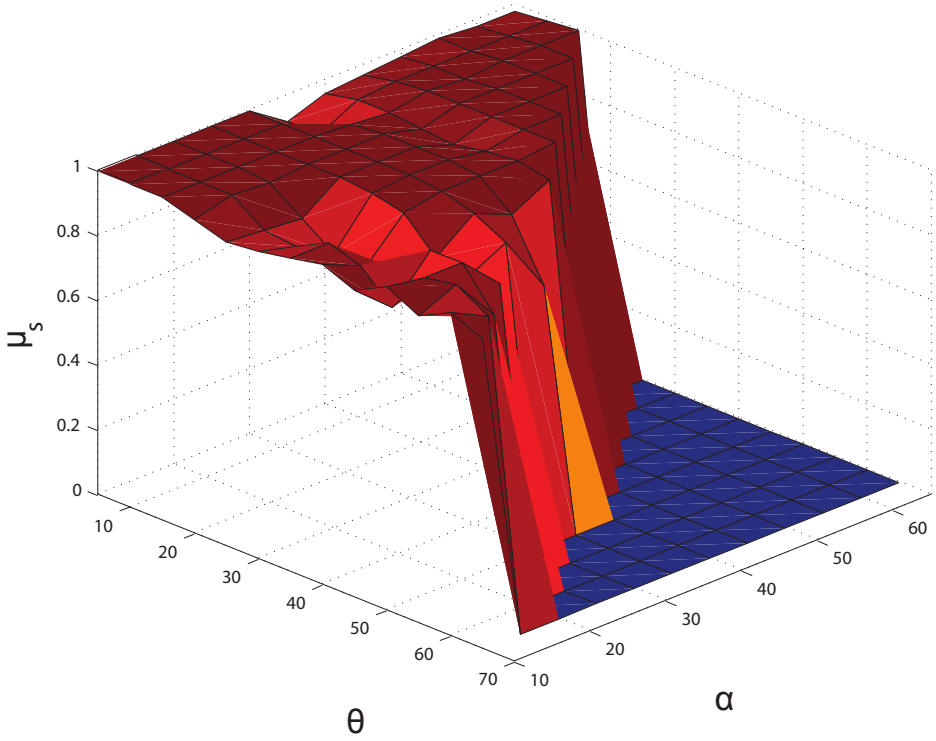

Figure 3.35: μ_s for configuration RP using FIFO relocation scheme.

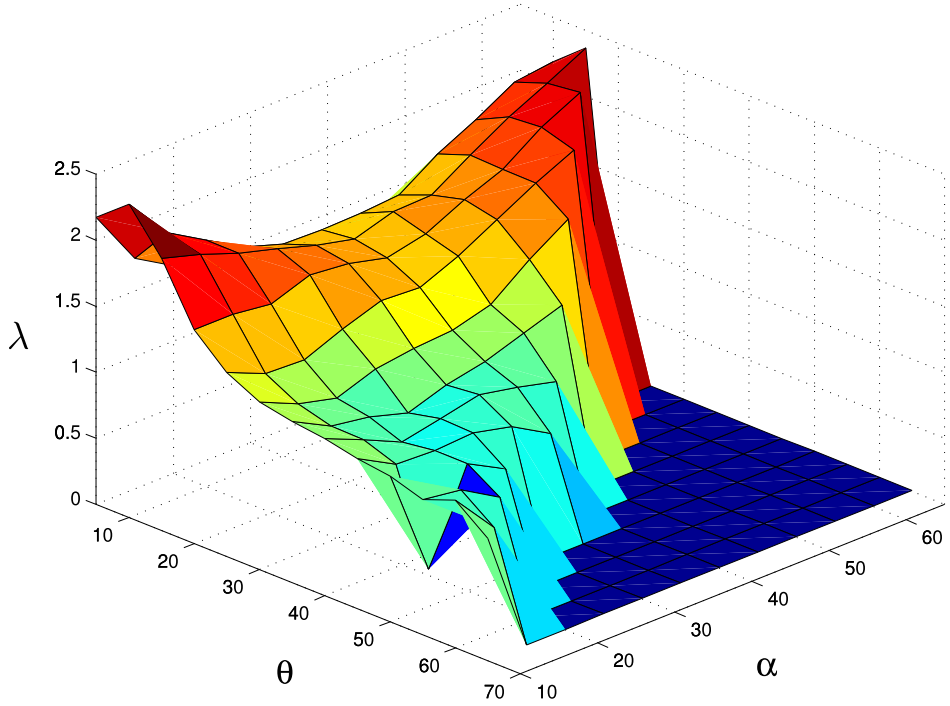

Figure 3.36: Lyapunov exponent for configuration RP using FIFO method.

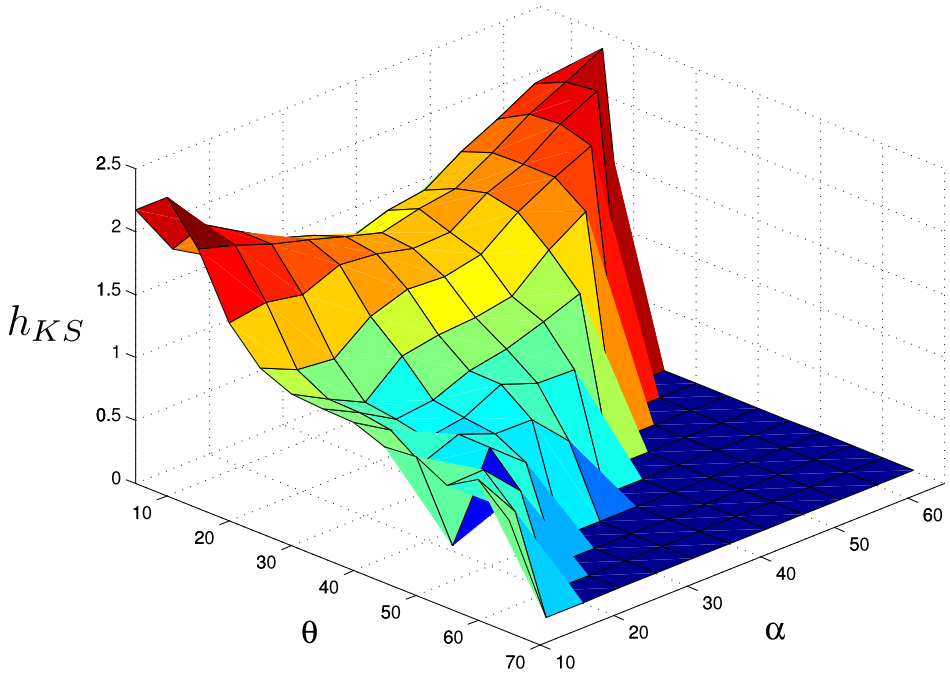

Figure 3.37: KS entropy for configuration RP using FIFO relocation scheme.

Configuration TP

Figure 3.10(d) shows a schematic of the configuration TP with the position of static source-sink pairs in the domain and the relation between the angles of extraction and reinjection of a fluid particle. Chaotic region is observed for various values of α and θ as shown in Fig. 3.38. Plots for μ_s, Lyapunov exponent λ and KS entropy h_{KS} are shown in Figs. 3.39,

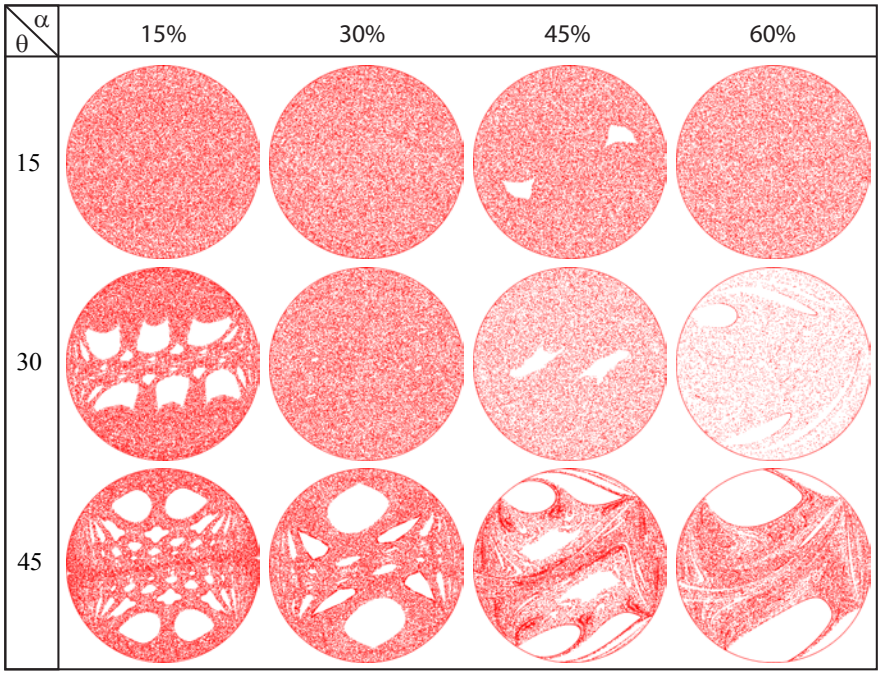

Figure 3.38: Poincaré sections for configuration TP with FIFO relocation scheme (TPF).

3.40, and 3.41, respectively.

Considering the delay time $d\alpha = 10\%$ for practical implementation as explained in Section 3.4.2, KS entropy for small value of α can be avoided. High value of KS entropy is $h_{KS} \approx 2.5$ for $5^o \leq \theta \leq 20^o$ and $55\% \leq \alpha \leq 65\%$. Table 3.1 lists the maximum KS entropy h_{KS} for each configuration with the consideration of $d\alpha = 10\%$ delay time.

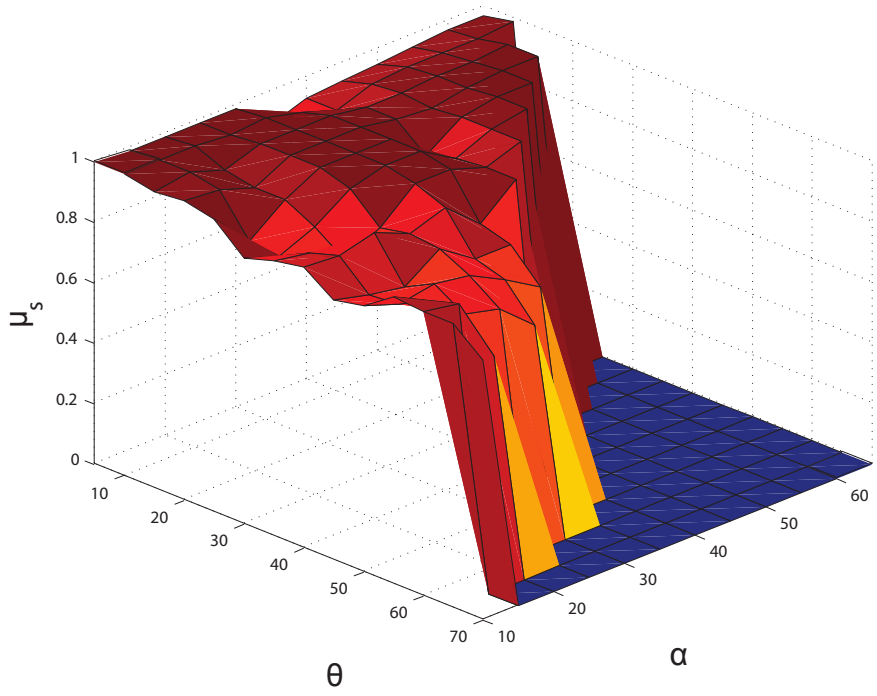

Figure 3.39: μ_s for configuration TP using FIFO relocation scheme.

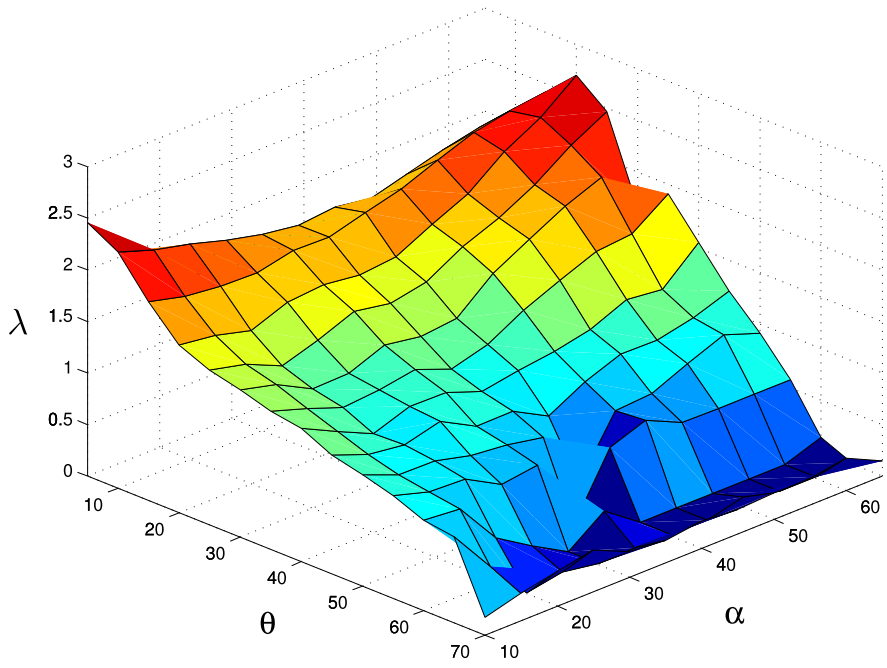

Figure 3.40: Lyapunov exponent for configuration TP using FIFO relocation scheme.

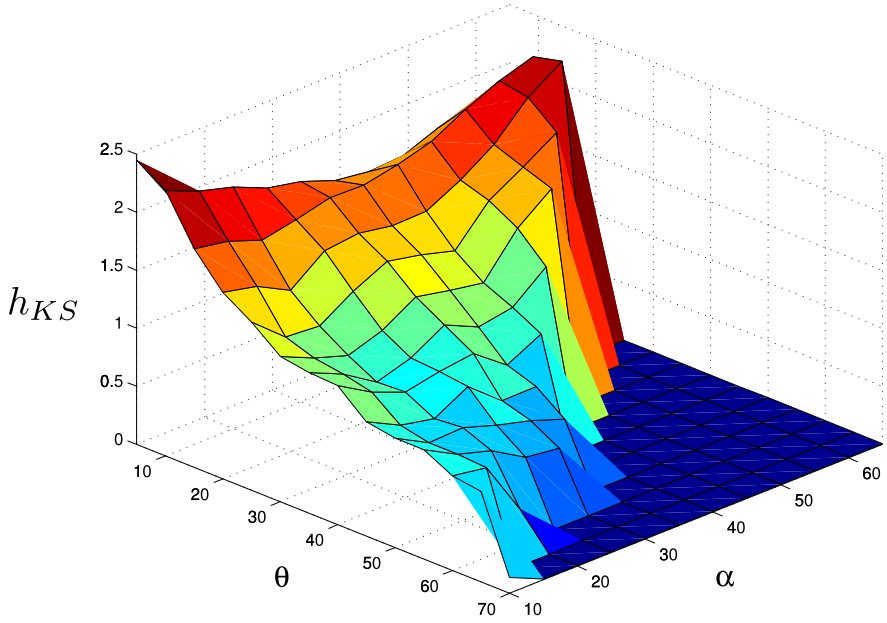

Figure 3.41: KS entropy for configuration TP using FIFO relocation scheme.

Table 3.1: Maximum KS entropy for pulsed source-sink systems.

	Configuration	h_{KS}	θ	α
LOFI	RX	0	0	0
	RP	1.5	$80^o \leq \theta \leq 90^o$	$10\% \leq \alpha 20\%$
	TX	1.0	$5^o \leq \theta \leq 20^o$	$10\% \leq \alpha 20\%$
	TP	0	0	0
FOFI	RX	2.5	$10^o \leq \theta \leq 20^o$	$60\% \leq \alpha 70\%$
	RP	2.5	$5^o \leq \theta \leq 20^o$	$55\% \leq \alpha 65\%$
	TX	2.5	$25^o \leq \theta \leq 40^o$	$55\% \leq \alpha 65\%$
	TP	2.5	$5^o \leq \theta \leq 20^o$	$55\% \leq \alpha 65\%$

3.5 Configurations with dynamic source-sink pairs

In a pulsed source-sink system, if fluid is extracted or reinjected through the same hole then the hole can be referred to as "dynamic", as defined in Section 3.3 and a pulsed source-sink pair consisting of "dynamic" holes is referred to here as a "Dynamic Source-Sink Pair (DSSP)".

The configurations presented in Section 3.4 avoid mechanical stirring for microfluidic systems. Chaos is generated in the system using combined action of pulsed operation of source-sink pairs and fluid relocation of extracted fluid from a source to a sink. Fabrication required for fluid relocation in a microfluidic system increases the procurement as well as maintenance cost of the equipments. In addition, practical implementation of the fluid relocation scheme adds delay time in the system, thereby increasing the effective pulse time of the systems and decreases the value of the KS entropy.

Fluid flow through a porous medium is described by Darcy's law. According to Darcy law, the pore velocity $\vec{u}$ is given as

$$\vec{u} = -\frac{k}{\varphi\mu}\nabla p, \tag{3.27}$$

where k is the permeability, μ is the dynamic viscosity, and φ is the porosity. Darcy flow in a porous medium and Hele-Shaw flow in a thin gap between rigid plates are represented by potential flows. The permeability k in the Darcy Eq. (3.27) is equivalent to the square of the gap between plates for Hele-Shaw flow [31]. Darcy law is only valid for slow viscous flows. So most groundwater flows can fall in this category.

Motivation of the work in present section is to design a pulsed source-sink system to generate complexity in fluid without relocating fluid. Avoiding the relocation of extracted fluid eliminates the fabrication required for the systems presented in Section 3.3. This section

presents pulsed source-sink system using DSSP which eliminates the delay time associated with the fluid relocation. In addition, the system presented in this section can be easily used in porous medium flow.

Configuration

A schematic diagram of the configuration DSSP is shown in Fig. 3.42. There are four

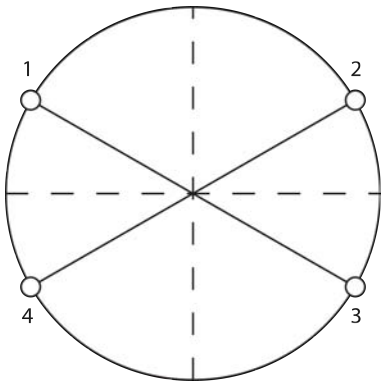

Figure 3.42: Configuration DSSP with four singularities on the circular boundary. Singularities connection by solid line operates together as a source-sink pair . Fluid extracted through a singularity is reinjected through the same singularity.

singularities at the boundary of the domain labeled as numbers 1, 2, 3, and 4. In practical implementation of the system, singularities are small holes at the boundary of the circular domain. All the singularities have equal strength and they can operate as a source or a sink for pulse time T. One period of the system consists of four pulses. Each pulse consists of a simultaneous action of two singularities, one as a source and other as a sink, as a source-sink pair for time T. The simultaneous operation of a source and a sink of equal strength conserves volume of fluid in the domain. A list of combination of the singularities as source-sink pairs during n^{th} period are shown in Table 3.2. Figure 3.43 shows the pulsed operation of source-sink pairs during n^{th} period. Fluid extracted through a singularity during i^{th} pulse is re-injected through the same singularity during $(i+2)^{th}$ pulse.

Table 3.2: Combination of singularities as a source-sink pair for four pulses during n^{th} period in configuration DSSP.

Pulse	Source	Sink
4(n-1)+1	1	3
4(n-1)+2	2	4
4(n-1)+3	3	1
4(n-1)+4	4	2

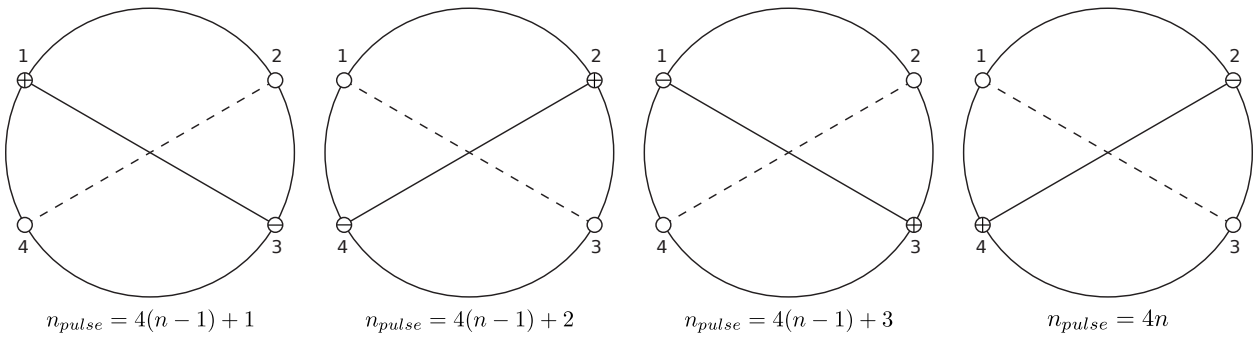

Figure 3.43: Combination of singularities as a source-sink pair for four pulses during n^{th} period in configuration DSSP. A source is denoted by $\oplus$ and a sink is denoted by $\ominus$. For a pulse, a source sink connected by solid line shows the active source-sink pair . n_{pulse} denotes the pulse number.

A Poincaré section is computed by plotting the position of a passive fluid particle after every period. A set of Poincaré sections are shown in Fig. 3.44 for various values of α and θ. Plots

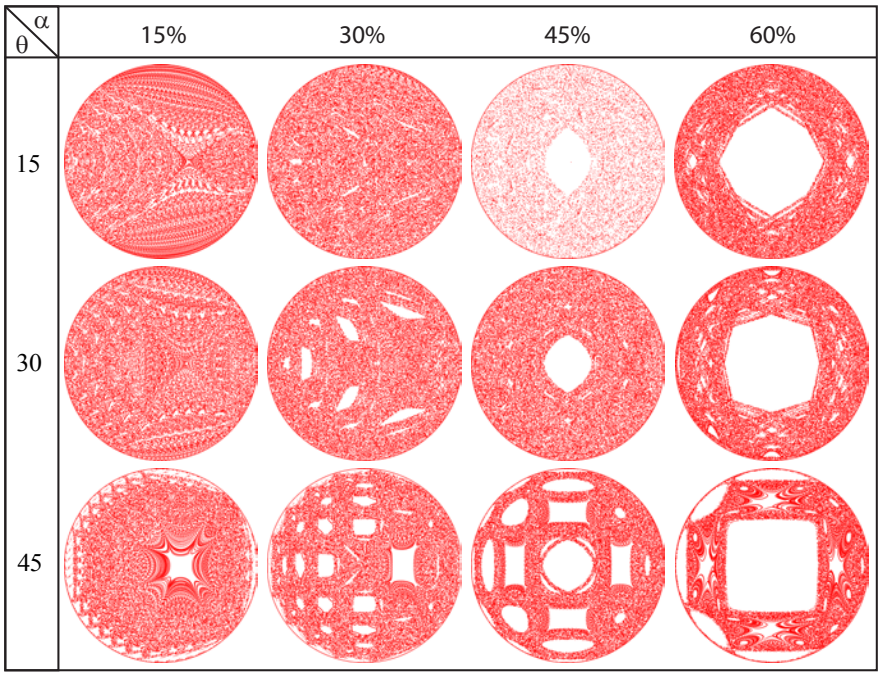

Figure 3.44: Poincaré sections for the configuration DSSP for various value of α and θ.

for μ_s, Lyapunov exponents λ and KS entropy h_{KS} are shown in Figs. 3.45, 3.46, and 3.47. So, chaos is generated in the system for various values of α and θ without fluid relocation. There is no delay time associated to extracted fluid transportation, hence, delay time is negligible and a system can be designed with small value of α. Highest value of KS entropy $h_k \approx 1.3$ is for $5^o \leq \alpha \leq 10^o$ and $5^o \leq \theta \leq 80^o$.

3.6 Summary

Pulsed source-sink systems are presented in this chapter to achieve chaotic advection in potential flow. The flow between two closely spaced parallel plates is modeled as Hele-Shaw flow with the depth averaged velocity proportional to the gradient of the pressure. Chaos

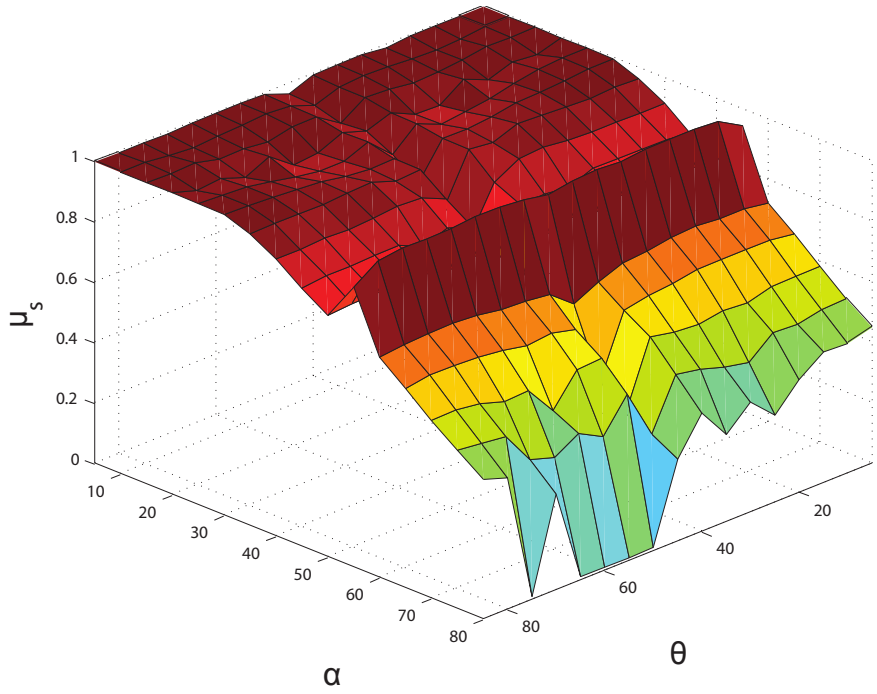

Figure 3.45: Variation of μ_s with α and θ for configuration DSSP.

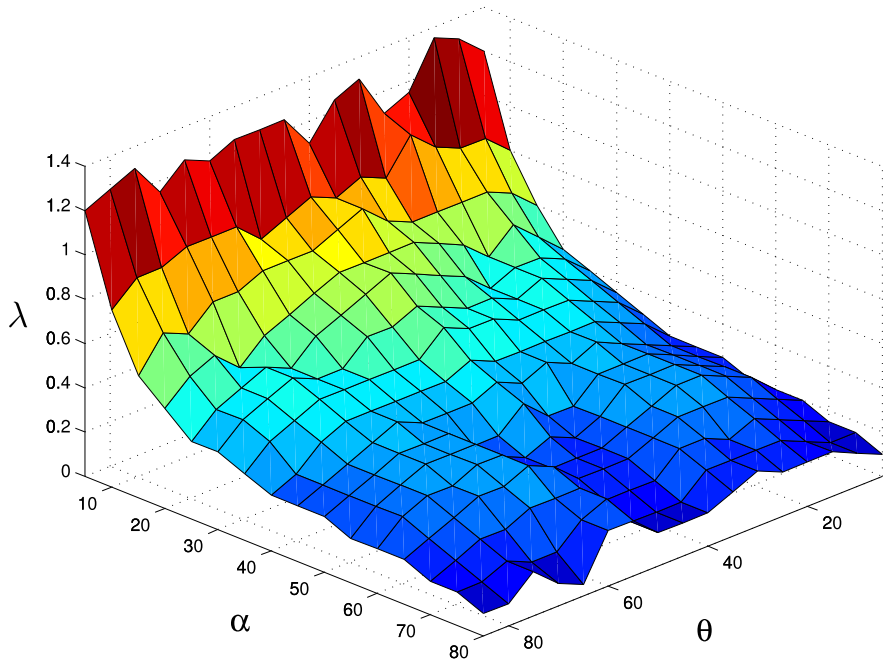

Figure 3.46: Variation of Lyapunov exponent with α and θ for configuration DSSP.

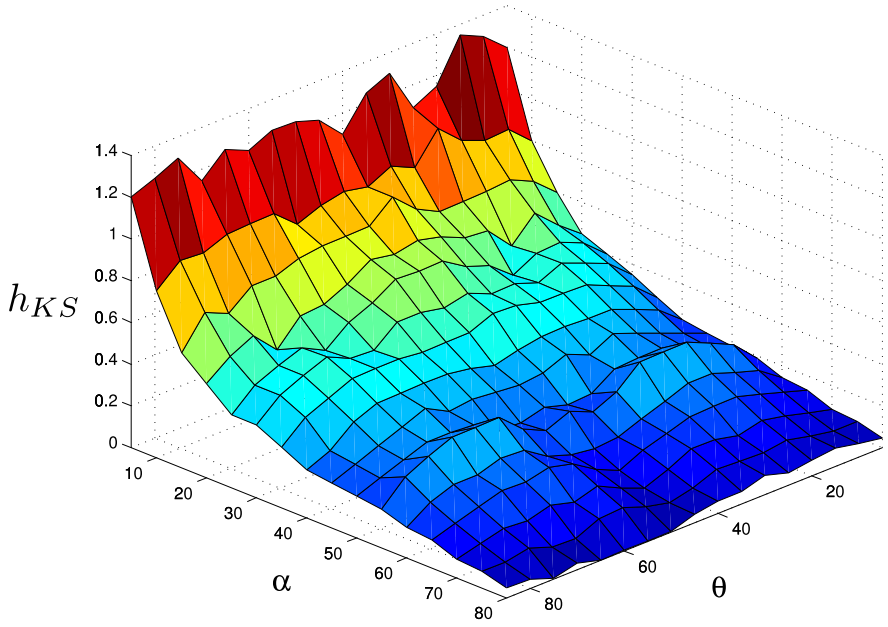

Figure 3.47: Variation of KS entropy with α and θ for configuration DSSP.

is generated in the flow by pulsed operation of fluid extraction and fluid reinjection through singularities in the domain. A sink is a singularity through which fluid is extracted and a source is a singularity through which fluid is reinjected. One source and one sink of equal strength operate together as a source-sink pair to conserve the volume of fluid in the domain. Configurations with crossed and parallel orientations of source-sink pairs are analyzed for a wide number of design parameters including the pulse volume, orientation of source-sink pairs, fluid relocation method, and fluid reinjection method. Kolmogorov-Sinai entropy is used as a mixing measure for the system. Maximum Lyapunov exponent and Poincaré section are computed to determine the mixing measure.

In the first analysis, fluid extracted through a sink is relocated for reinjection through a source to generate complexity in the flow. Two different methods, "LOFI" and "FOFI", are used for the fluid relocation. Configurations with "FOFI" relocation scheme generates comparatively more complex fluid flow than the configurations with "LOFI" relocation scheme.

The second analysis presents and analyzes a pulsed source-sink system generating complex

fluid flow without fluid relocation. The absence of fluid relocation reduces the fabrication requirement. In addition, delay time due to the extracted fluid relocation is comparatively zero.

Chapter 4

Pulsed Lid-Driven Cavity Flow

4.1 Introduction

A quantitative lower bound on the complexity of a two-dimensional stirred flow can be determined by examining the motion of boundaries [8]. According to the TNCT [9], appropriate time-dependent stirring with a sufficient number of rods in a fluid domain, e.g., pseudo-Anosov stirring with at least three rods for bounded or unbounded two dimensional flow in a plane, guarantees exponential stretching and folding of at least some of the fluid. The Thurston-Nielsen classification theorem does not require the use of solid rods for stirring. Rather, stirrers can be vortices or passive fluid particles which interact dynamically with appropriate trajectories [10, 20]. Gouillart et al. [20] termed the passive periodic structures "ghost rods". The TNCT does not depend on the flow dynamics: however, Chen [10] shows that the existence of the ghost rods depends on the flow dynamics. Recently, the analysis of ghost rods with topology has been extended to aperiodic orbits [52]. If a finite time portion of these aperiodic orbits can be periodically continued to orbits with the necessary topology, then predictions of exponential stretching and folding in the surrounding fluid can be

made. This generalization relaxes a substantial restriction in the application of the TNCT . However, this approach also introduces the significant complexity of needing to identify appropriate aperiodic orbits, as a random selection of trajectories generally leads to a poor estimate of the overall system behavior [51].

In this chapter, we determine the existence of ghost rods and apply the TNCT based on the presence of almost invariant sets as ghost rods. Almost invariant sets (AIS) define macroscopic structures preserved by the flow dynamics. This method makes the ghost rod methodology applicable to a wide range of problems. First, we give a description of the example system and demonstrate an application of the TNCT to a reference case in which there exist low-order periodic orbits. Next, we show that an eigenfunction of the Perron-Frobenius operator associated with this system is an almost invariant set with topological properties that give a lower bound on the measured topological entropy. This method is also applicable when the system is perturbed so that appropriate periodic orbits no longer exist. That is, the periodic motion of these almost invariant sets can be used as ghost rods for application of the TNCT . A method to predict line stretching is presented in Section 4.7 by tracking a braiding motion of three finite size rods. In the limiting case, when the size of rods are zero, the method leads to a matrix for pseudo-Anosov type of braiding which matches with the matrix derived from the TNCT in Section 2.7.1. In Section 4.8, the concept of almost invariant sets as ghost rods is presented for lid-driven cavity flow at finite Reynolds number on which to apply the TNCT. Conclusions of the work on fluid mixing in a lid-driven cavity flow are given in Section 4.9.

4.2 Lid-driven cavity flow

This section describes the fluid system used for the design and verification of the analysis techniques. The considered fluid system is a two-dimensional lid-driven cavity flow in an infinitely wide cavity. The top and bottom boundaries are enforced as spatially-periodic and the flow can be viewed as a combination of a series of rectangular lid-driven cavity flows with periodic side boundary conditions. For our example system, we consider two-dimensional Stokes flow in a rectangular domain $M = (x, y) : 0 \leq x \leq 2a, -b \leq y \leq b$, and streamlines of the flow serve as the vertical boundaries at $x = 0,\ 2a$. For a Stokes flow in lid-driven

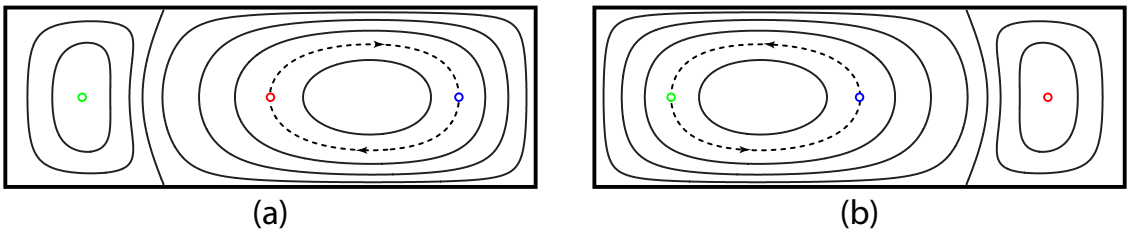

Figure 4.1: Possible streamlines with top and bottom boundaries moving under piecewise uniform velocity. (a) Streamlines for $n\tau_f \leq t \leq (n + 1/2)\tau_f$ and the flow is denoted by $R+$ and (b) streamlines for $(n + 1/2)\tau_f \leq t \leq (n + 1)\tau_f$ and the flow is denoted by $L-$, where $n \geq 0$ is an integer.

cavity, the stream function $\psi(x, y)$ satisfies the two-dimensional biharmonic equation given by (2.17). The biharmonic equation is linear so the lid-driven cavity flow with four side walls can be divided into four subproblems which can be numerically solved by Meleshko's method [10, 30]. A detailed solution of the biharmonic equation in a lid-driven cavity flow model is discussed in [10].

Let the top and bottom boundary velocities be expressed as a series sum of sinusoidal functions. For simplicity, only two terms of the series are considered here. With two terms

in the series, the piecewise steady boundary velocity of the top boundary is given as

$$V(x,b) = \begin{cases} U_1 sin(\pi x/a) + U_2 sin(2\pi x/a) & 0 \le t \le \tau_f/2 \\ -U_1 sin(\pi x/a) + U_2 sin(2\pi x/a) & \tau_f/2 \le t \le \tau_f \end{cases} \tag{4.1}$$

where τ_f is the normalized period of the periodic boundary condition. The corresponding bottom boundary velocity is given by $V(x,-b) = -V(x,b)$. Figure 4.1 shows the symmetry of the flow fields during $0 \le t \le \tau_f/2$ and $\tau_f/2 \le t \le \tau_f$ developed by the boundary velocity at the top and bottom boundaries. For the boundary condition above [10, 30], the stream function can be given as

$$\psi(x,y) = \sum_{n=1}^{N} U_n C_n f_n(y) \sin\left(\frac{n\pi}{2}\right), \tag{4.2}$$

where

$$f_n(y) = y\cos\left(\frac{nb}{2}\right)\sin\left(\frac{ny}{2}\right) - b\sin\left(\frac{nb}{2}\right)\cos\left(\frac{ny}{2}\right),$$

and

$$C_n = 2[\sinh(nb) + nb]^{-1}.$$

With $N = 2$, Eq. (4.2) can be written as

$$\psi(x,y) = U[\sqrt{1-\beta}\psi_1 + \sqrt{\beta}\psi_2], \tag{4.3}$$

where

$$\psi_1 = C_1 f_1(y)\sin(x/2)$$

$$\psi_2 = C_2 f_2(y)\sin(x).$$

There is no singularity in the boundary condition, and hence it may be possible to build an experimental implementation of the presented model. The possible streamlines for the piecewise uniform boundary motions are shown in Fig. 4.1. With the symmetric boundary velocity, it is possible to generate three period-three points in the cavity that form a non-trivial braid in $(2+1)D$ space-time for specific values of β and τ_f. A schematic of the

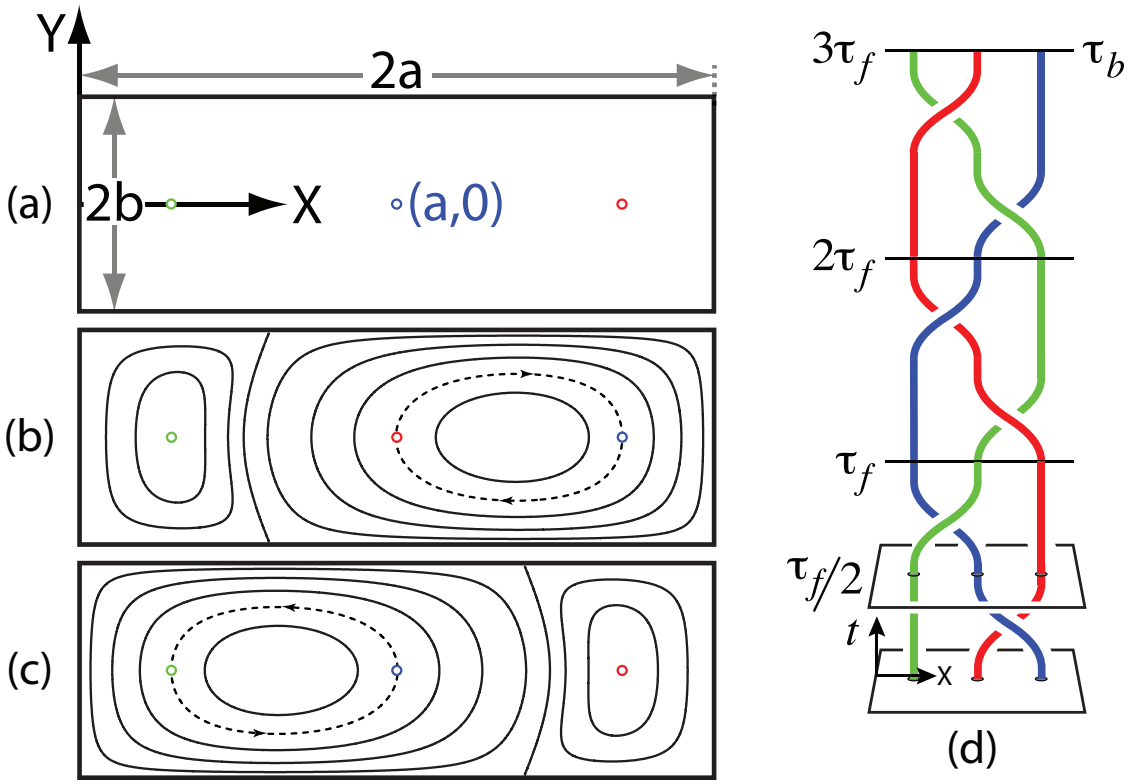

Figure 4.2: Non-trivial braiding of three period-3 points in lid-driven cavity flow. (a) Dimension and design of the of the lid-driven cavity flow. Three small circles show the location of the periodic points for the reference case, (b) initial position of three periodic points, (c) positions of three periodic points after $t = \tau_f/2$, and (d) braiding of the fixed point for the reference case.
The lowest rectangle in (d) shows the lid-driven cavity flow domain for (b) and the second lowest rectangle in (d) shows the lid-driven cavity flow domain for (c).

resulting non-trivial braid is shown in Fig. 4.2. To ensure the existence of three periodic points:

- Three periodic points X_L, X_C and X_R are denoted by green, red and blue circles in Fig. 4.2 (a), respectively. The point X_C is located exactly at the center of the domain, and X_L and X_R are symmetric about X_C in the horizontal direction and at the center of the domain in the vertical direction. The value of β is computed using the position of these three periodic points.

- For $0 \leq t \leq \tau_f/2$, X_L is a fixed point and X_C and X_R are moving clockwise. At $t = \tau_f/2$, X_C and X_R have exchanged their positions. This condition determines the value of U and τ_f.

- For $\tau_f/2 \leq t \leq \tau_f$, X_R is a fixed point and X_L and X_C are moving counterclockwise.

With the aspect ratio of the domain $b/a = 1/3$, the values of $\beta = 0.414445$ and $U = 9.173958$ generate three periodic points X_L, X_C, and X_R with $\tau_f = \tau_f^* = 1.0$ as the reference case.

4.3 Topological chaos in lid-driven cavity flow

The braiding protocol in the case described in Section 4.2 has the same pseudo-Anosov braid as discussed in Section 2.7.1. Thus, the lower bound h_{TNCT} on topological entropy using the TNCT is $\log(\lambda_{TN}) \approx 0.962$, where $\lambda_{TN} = (3+\sqrt{5})/2$. The actual topological entropy of this flow is determined by computing the stretching rate of topologically nontrivial lines, such as loops that encircle exactly two of the periodic points or lines that join periodic points with the outer boundary. For the reference case, the computed topological entropy with the line stretching data for 10 periods, as shown in Fig. 4.3, is $h = 0.968$, which is well represented by the lower bound given by the underlying braid.

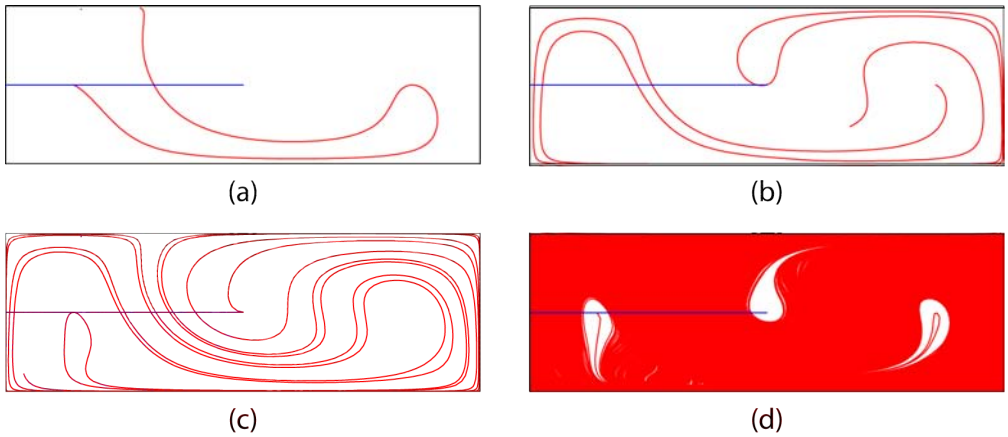

Figure 4.3: Stretching of a material line initially along the blue line, (a) after one period of the flow, (b) after two periods of the flow, (c) after three periods of the flow, and (d) after ten periods of the flow.

4.4 Perturbation from the reference case

For the analysis of flow in the lid-driven cavity flow, β in Eq. (4.3) is kept fixed and the value of τ_f is perturbed from the reference case $\tau_f^* = 1.0$. Perturbing the value of τ_f away τ_f^* prevents the points identified in Fig. 4.2 from exactly exchanging position when the underlying flow is changed, and these points no longer lie on period-3 orbits on the flow. So, the pseudo-Anosov braiding of ghost rods using low-order periodic orbits is not present for $\tau_f < \tau_f^*$. Perturbing the value of τ_f above τ_f^* breaks the periodic points into a set of two hyperbolic points and two elliptic points forming a ghost rod structure as shown in Fig. 4.4. The braiding motion of the ghost rod structure is of pseudo-Anosov type and the predicted lower bound on h_f remains $h_{TN} = 0.962$. However, it is found that the difference between the computed topological entropy and the h_{TN} increases with τ_f.

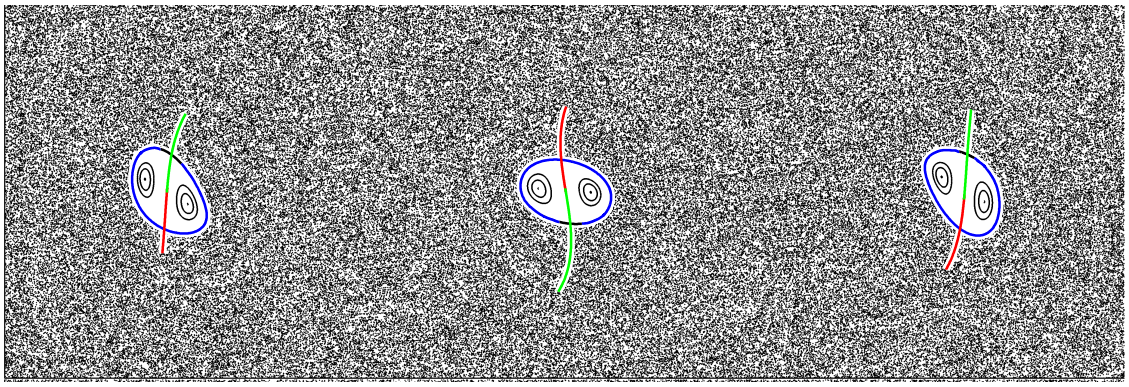

Figure 4.4: Ghost rod structure for $\tau = 1.01$ with Poincaré section in lid-driven cavity flow .

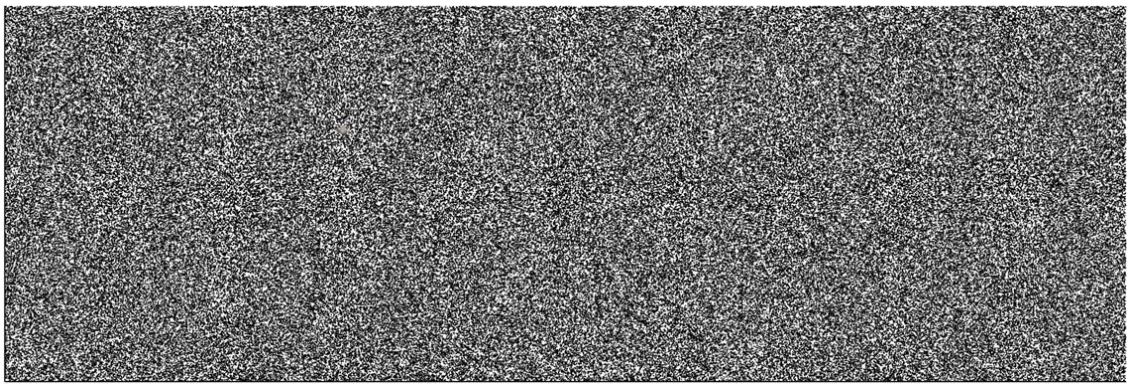

Figure 4.5: Poincaré section for flow in lid-driven cavity flow for $\tau_f = 0.98$.

4.5 Lower bound of topological entropy

Case: $\tau_f < \tau_f^*$

Perturbing the value of τ_f below τ_f^* destroys the formation of the periodic orbits as discussed in Section 4.4. Thus, the pseudo-Anosov braiding of ghost rods based on periodic orbits is not present. The careful analysis of the Poincaré section for $\tau_f < \tau_f^*$ in Fig. 4.5 shows the chaotic regions in phase space. Also, the plot in Fig. 4.6 for computed values of h_f shows that h_{TN} from the reference case still provides a good estimate as a lower bound for $0.93 < \tau_f < \tau_f^*$ even when there is not any periodic point in the system on which to apply the TNCT. The presence of stretching and folding for $0.93 < \tau_f < \tau_f^*$ such that $h_f > h_{TN}$ motivates us to

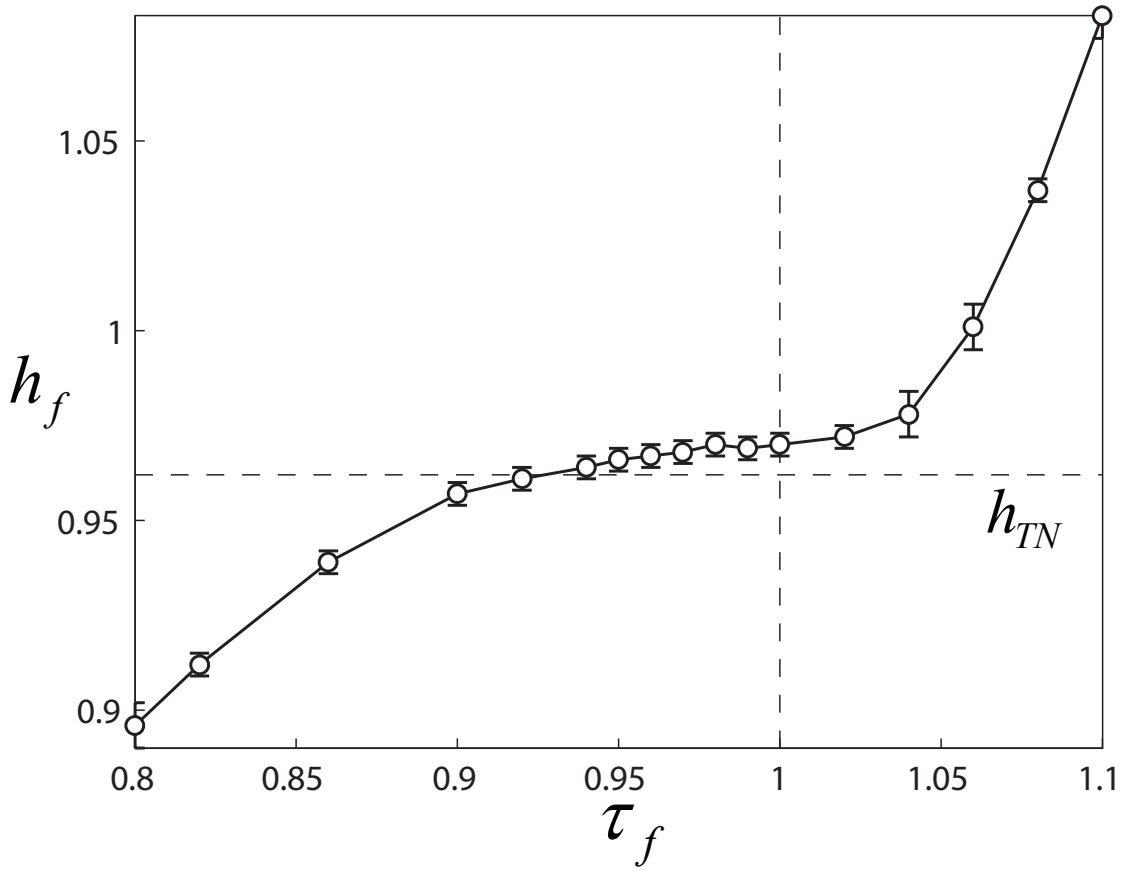

Figure 4.6: Topological entropy h_f of the perturbed flow for various periods of the flow, τ_f. The TNCT predicts lower bound h_{TNCT}.

analyze the system to verify the existence of structures with pseudo-Anosov braiding motion. To explain the validation of the TNCT for $0.93 < \tau_f < \tau_f^*$, we move away from identifying exactly periodic orbits as ghost rods and choose the concept of almost invariant sets.

4.6 Almost invariant sets

The validity of the TNCT for $0.93 < \tau_f < \tau_f^*$, in the absence of periodic points, motivates a search for structures in phase space that serve as ghost rods [48]. In this section, it will be shown that almost invariant sets serve as ghost rods in this flow and form a pseudo-

Anosov braid. The almost invariant set drags the fluid in a nontrivial way resulting in exponential stretching and folding [48]. An almost invariant set will be verified as a macroscopic natural object which braids in a non-trivial way and satisfies the requirement for the validation of the TNCT.

4.6.1 Computing almost invariant sets

To compute the dynamics in lid-driven cavity flow we cover the domain M with a collection of $n = 120 \times 40 = 4800$ rectangular boxes, where 120 is the number of boxes in the $x-$direction and 40 is the number of boxes in the $y-$direction. Each box in the domain can be labeled as $B_1,\ B_2, \ldots, B_{4800}$. A total of 900 points are equally distributed in each box at time $t = 0$, such that no point is on the boundary of any box. Each point in M is iterated forward in time for one period of the flow, and the new box reached by each point is computed. A transition probability matrix P_{t,τ_f} is computed by the fraction of points from the source box that reach the destination box. Any $(i,j)^{th}$ element of the transition matrix can be approximated as

$$(P_{t,\tau_f})_{i,j} = m(B_i \cap f^{-1}(B_j))/m(B_i), \tag{4.4}$$

where f is the map from time t to $t+\tau_f$, B_i is the source box, B_j is the destination box, and m is the area measure. Figure 4.7 shows the physical meaning of the quantity $B_i \cap f^{-1}(B_j)$ for $i = 122$ and $j = 4$. The transition matrix P_{t,τ_f} is a matrix of an $n-$state Markov chain. Since P_{t,τ_f} is not reversible in time, a reversible matrix R_{t,τ_f} is generated from P_{t,τ_f} to determine its eigenspectrum.

To find the almost invariant set , we consider only those partitions of the domain A_i as almost invariant sets , where $i = 1, 2, \ldots, k$ such that $A_i = \cup_{j \in I} B_j$, for some set of box $I \in \{1, 2, \ldots, n\}$. The first eigenvector v_1 of R_{t,τ_f}, which corresponds to an eigenvalue

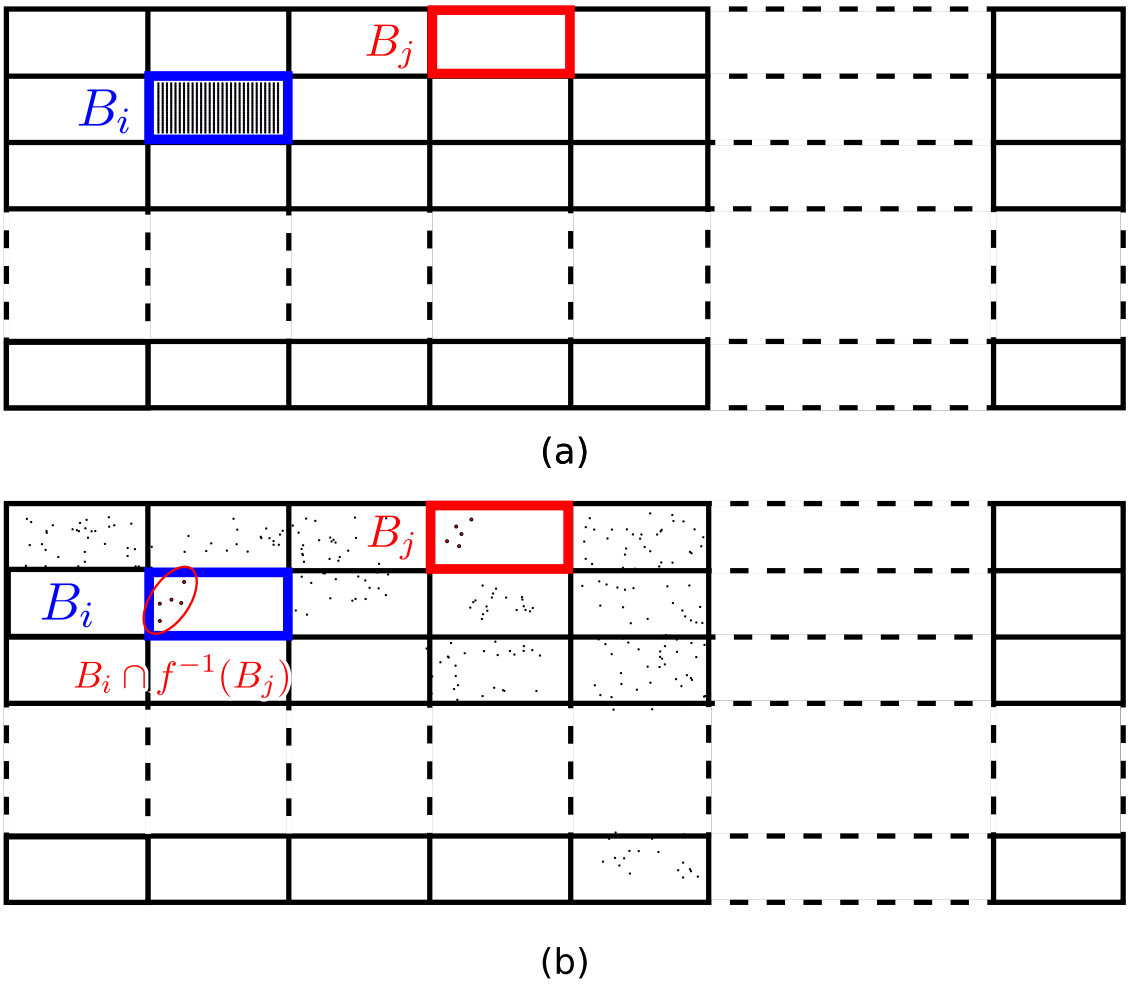

Figure 4.7: A schematic of covering the domain with $n = 120 \times 40 = 4800$ rectangular boxes. $m(B_i \cap f^{-1}(B_j)) = 5$ with 900 points in i^{th} box for $i = 122$ and $j = 4$. The larger red dots shown in source box B_i for $i = 122$ reach the destination box B_j for $j = 4$.

$\lambda_1 = 1$, is the invariant distribution of the system. Since we know that our system is Hamiltonian, v_1 corresponds to a uniform distribution all over the phase space. The second eigenvector v_2, corresponding to the second largest eigenvalue λ_2, divides the phase space into two sets such that $v_2 > c$ and $v_2 < c$. The two sets divided by v_2 are the two almost invariant set structures. Two plots of almost invariant sets corresponding to the second largest eigenvalue λ_2 are shown in Fig. 4.8. The almost invariant set corresponding to the region with components of $v_2 > 0$ is shown as three structures located nearly at the location

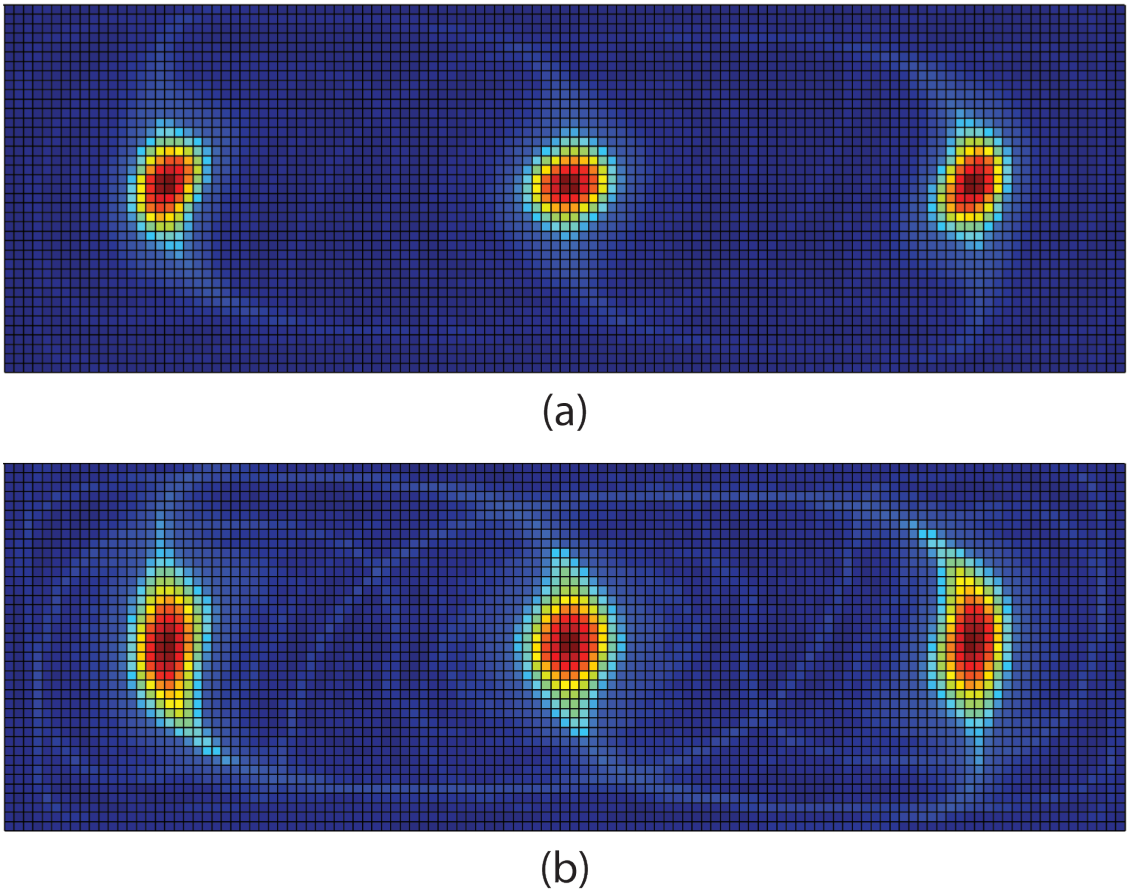

Figure 4.8: Almost invariant set structures for (a) $\tau_f = 1.00$, when three periodic points are in the domain and (b) $\tau_f = 0.98$, when the domain has no periodic point.

of the periodic points for the reference case $\tau_f = \tau_f^*$. The magnitudes of the eigenvalues are associated with the leakiness of the almost invariant set. Larger eigenvalues correspond to less leakiness of the almost invariant sets, but smaller eigenvalues correspond to more leakiness of the almost invariant sets. The highest eigenvalue $\lambda_1 = 1$ shows that the system is invariant. The value of λ_2 is close to λ_1 such that $\lambda_2 < \lambda_1$ indicates that the almost invariant sets corresponding to λ_2 have some leakiness. Eigenvector plots for $\tau_f = 1.00$ and $\tau_f = 0.98$ are shown in Fig. 4.8 to verify the existence of almost invariant sets in the phase space even when periodic points disappear from the phase space.

4.6.2 Braiding analysis with almost invariant set

We have shown the existence of three components of one almost invariant set corresponding to the second highest eigenvalue λ_2 for $0.93 < \tau_f < \tau_f^*$. The next step is to analyze the braiding motion of these sets to verify if these sets generate a braid of pseudo-Anosov type. We considered $\tau_f = 0.98$ for the braiding analysis. Markov operators are computed for 10 different time steps from $t = 0,\ \tau_f/10, \ldots t_f$ with the time step $dt = \tau_f/10$. To determine the Markov operator at a time step $t = t_i$, where $i = 1,\ 2, \ldots,\ t_f$, the cover the domain M with a collection of $n = 120 \times 40 = 4800$ rectangular boxes, where 120 is the number of boxes in the $x-$direction and 40 is the number of boxes in the $y-$direction at time $t = t_i$ with a total of 900 points are equally distributed in each box. Each point in M is iterated forward in time from $t = t_i$ to $t = t_i + \tau_f$, and the new box reached by each point is computed. The rest of the steps required to compute the transition matrix is similar to explained in Section 4.6.1.

The braiding motion of the almost invariant set components is shown in Fig. 4.9(a) for $n\tau_f \leq t \leq (n + 1/2)\tau_f$ and in Fig. 4.9(b) for $(n + 1/2)\tau_f \leq t \leq (n + 1)\tau_f$. It can be recalled that the motion in Fig. 4.9(a) corresponds to σ_2, and the motion in Fig. 4.9(b) corresponds to σ_{-1} (Section 2.7.1). So, the braiding protocol for a period is given by $\sigma_{-1}\sigma_2$. Following the pseudo-Anosov braiding formed by an almost invariant set, the lower bound on topological entropy is given by $h_{TN} \approx 0.962$, and thus, the TNCT is valid for $\tau_f = 0.98$. The braiding with three strands generated by almost invariant set exists to $\tau_f \approx 0.96$. For $\tau_f < 0.95$, the almost invariant set with three (3) cyclic structures breaks into an almost invariant set with sixteen (16) cyclic structures.

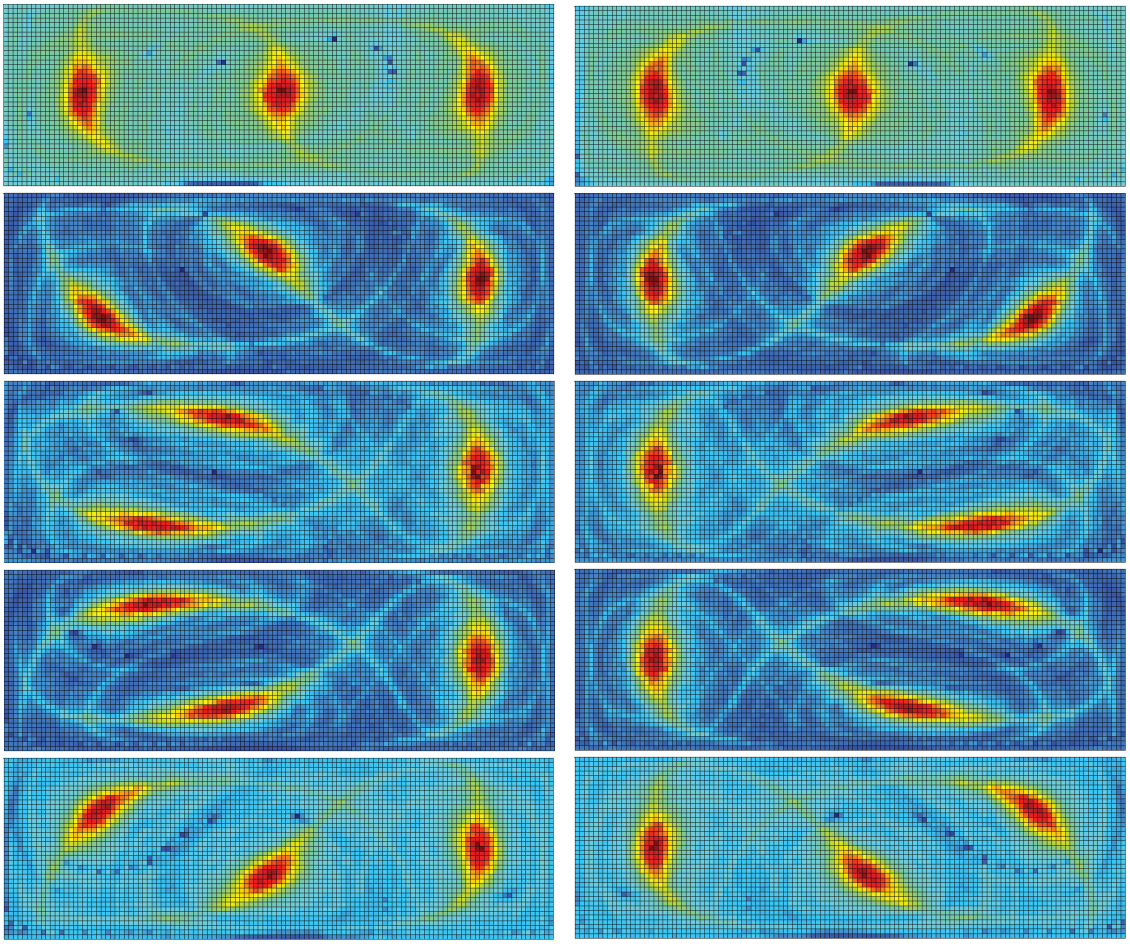

Figure 4.9: Braiding of almost invariant set structure for (a) $n\tau_f \leq t \leq (n+1/2)\tau_f$ and (b) $(n+1/2)\tau_f \leq t \leq (n+1)\tau_f$. Time step from top to bottom is $dt = \tau_f/10$.

Case: $\tau_f > \tau_f^*$

Varying the value of τ_f away from τ_f^* prevents the points identified in Fig. 4.2 from exactly exchanging positions before the underlying flow is changed, and these three points no longer lie on period-3 orbits of the flow. When $\tau_f > \tau_f^*$, each of the periodic points bifurcate into a set of two hyperbolic points and two elliptic points as shown in Fig. 4.10(b). Stable and unstable manifolds join the corresponding two hyperbolic points and envelop the two elliptic points. These four periodic points travel together through the flow, simply twisting around

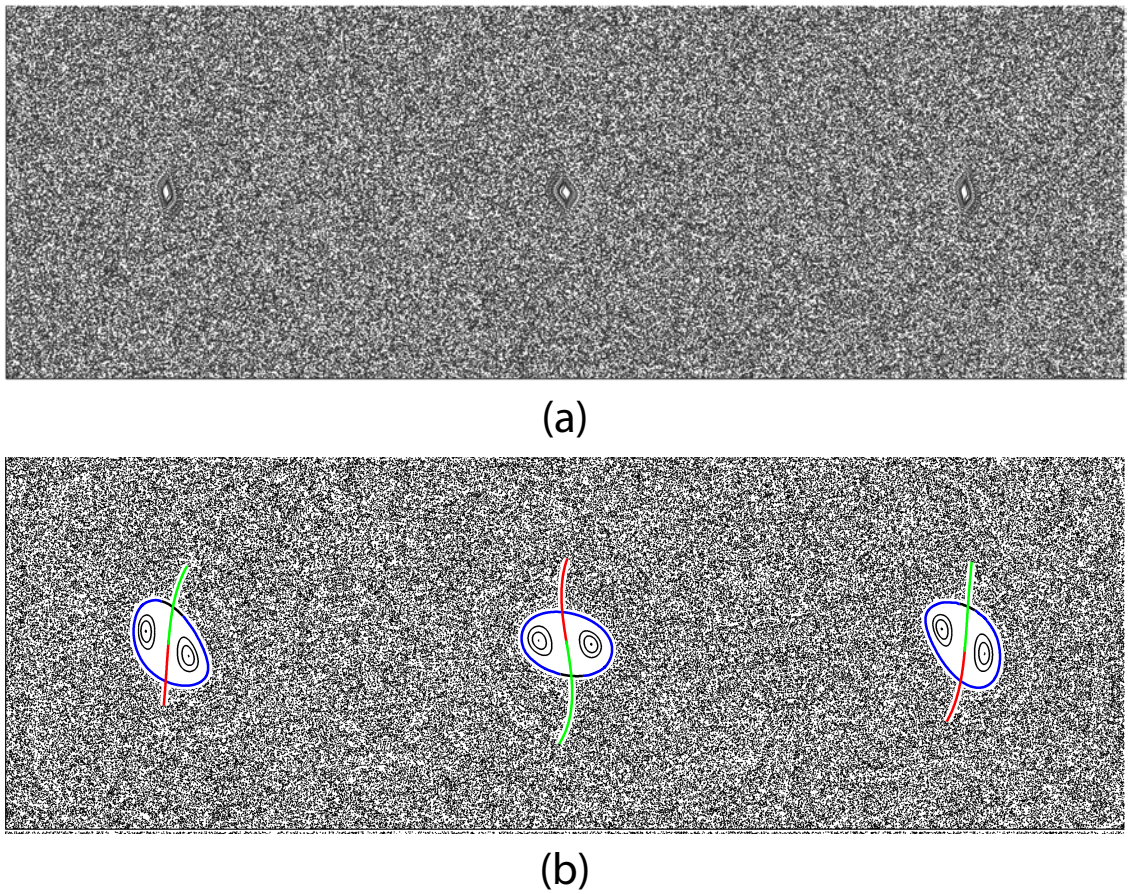

Figure 4.10: Breaking of the periodic points into hyperbolic points and elliptic points. (a) Parabolic points for $\tau_f = \tau_f^*$ and (b) ghost rods for $\tau_f > \tau_f^*$ consisting of two hyperbolic points, two elliptic points, and manifolds connecting the hyperbolic points.

one another as they move. The global motions of these periodic orbits are similar to that in the reference case. Thus, the perturbed flow with $\tau_f > \tau_f^*$ can be represented by a braid that is *reducible* to the pseudo-Anosov braid on three strands from the reference case, and the predicted lower bound on h remains $h_{\mathrm{TN}} \approx 0.962$. For large $\tau_f > \tau_f^*$, the size of the ghost rods in the flow leads to additional stretching and folding that is not captured by the lower bound predicted by the TNCT .

4.7 Braiding analysis with finite-size rods

It is shown in Section 4.5 that the TNCT predicts the lower bound of the topological entropy using the information from the braiding motion of the rods and does not count on the geometry of the domain or boundary. It is also shown in the previous section that the almost invariant sets can be used as natural objects to predict the class of braiding motion. Careful analysis of the plot for topological entropy, Fig. 4.6, shows:

- The topological entropy increases for $\tau_f > \tau_f^*$ which is not captured by the TNCT
- The value of topological entropy is nearly constant for $0.96 < \tau_f < 1.01$,

which motivates the work in the present section.

In the first part of the section, we present an analysis of pseudo-Anosov braiding motion with three rods which gives the braiding matrix derived from the TNCT for pseudo-Anosov type braiding for a three-rod system. In the second part of the section, the braiding analysis is modified to consider the rods' geometry when deriving the braiding matrix. A detailed analysis of the method is presented with an application for lid-driven cavity flow.

Figure 4.11 shows the pseudo-Anosov braiding motion of three periodic points. In this figure, three periodic points are connected with two material lines shown with the colors black and cyan. In this system, the left, central, and the right rods are counted as 1, 2, and 3, respectively. The stretched line is divided into two sections:

Section	Material Length	Rod_1	Rod_2
1	x_n	1	2
2	y_n	2	3

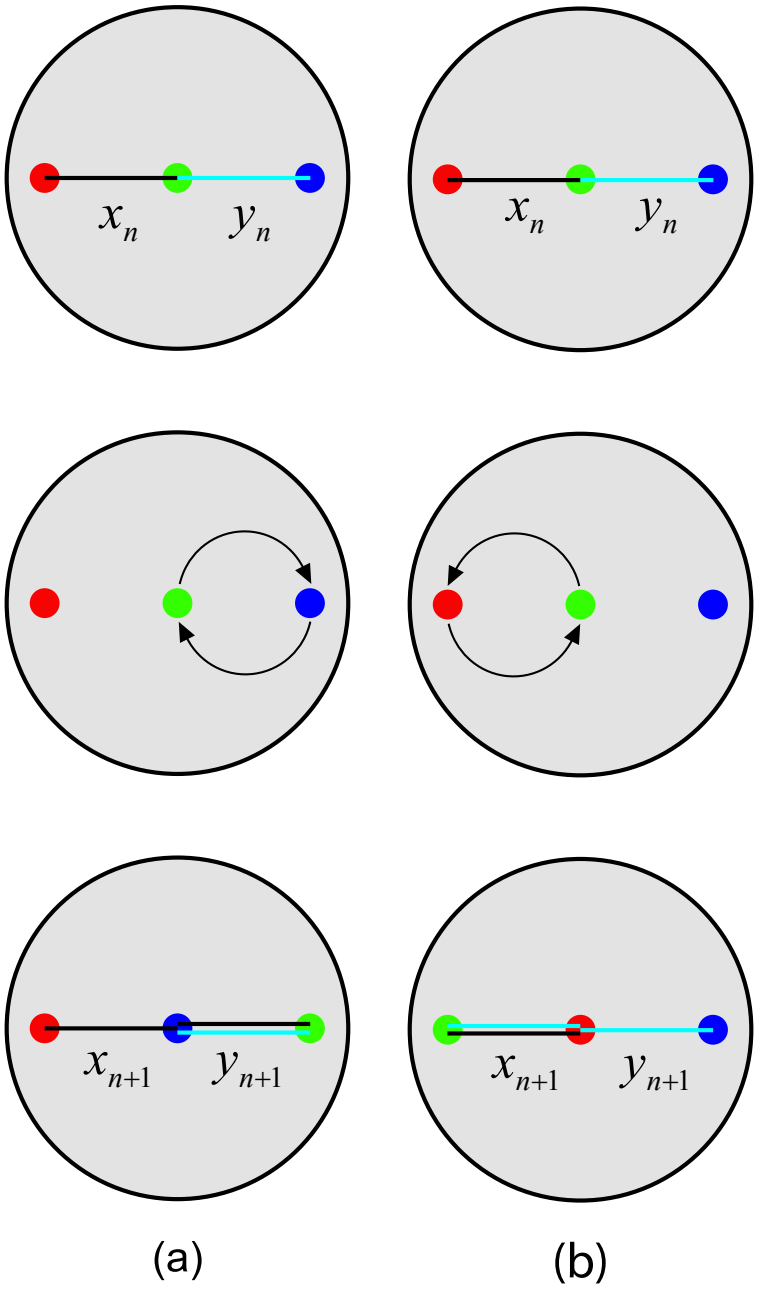

Figure 4.11: Material stretching for stirrers interchange for (a)R_+ interchange with braid σ_2 and (b) L_- interchange with braid σ_{-1}.

where x_n is the length of the stretched line in section 1, y_n shows the length in section 2, and n is the pulse number. Stretched lines are connected to rods Rod_1 and Rod_2 in both of the sections. Suppose x_n and y_n are material lengths after the n^{th} pulse, and after the $(n+1)^{th}$ pulse with the σ_2 braiding motion the material lengths are denoted as x_{n+1} and y_{n+1}. As shown in Fig. 4.11, the values of x_{n+1} and y_{n+1} are

$$x_{n+1} = x_n, \tag{4.5}$$

and (4.6)

$$y_{n+1} = x_n + y_n, \tag{4.7}$$

which can be written in matrix form as

$$\begin{bmatrix} x_{n+1} \\ y_{n+1} \end{bmatrix} = M_2 \begin{bmatrix} x_n \\ y_n \end{bmatrix}$$

where

$$M_2 = \begin{bmatrix} 1 & 0 \\ 1 & 1 \end{bmatrix}.$$

The material length with σ_{-1} braiding, as shown in Fig. 4.11(b) is

$$x_{n+1} = x_n + y_n, \tag{4.8}$$

and (4.9)

$$y_{n+1} = y_n, \tag{4.10}$$

which can be written as

$$\begin{bmatrix} x_{n+1} \\ y_{n+1} \end{bmatrix} = M_{-1} \begin{bmatrix} x_n \\ y_n \end{bmatrix},$$

where

$$M_{-1} = \begin{bmatrix} 1 & 1 \\ 0 & 1 \end{bmatrix}.$$

The matrix representation of braiding motion σ_2 followed by σ_{-1} can be written as

$$M = M_{-1}M_2 = \begin{bmatrix} 1 & 1 \\ 0 & 1 \end{bmatrix} \begin{bmatrix} 1 & 0 \\ 1 & 1 \end{bmatrix} = \begin{bmatrix} 2 & 1 \\ 1 & 1 \end{bmatrix},$$

which matches with the matrix representation of the pseudo-Anosov braiding with three rods in Eq. (2.29). For braiding motion with rods of finite size, rods can be considered circular with radius $r = \alpha l$, where l is the distance between two ghost rods as shown in Fig. 4.12. Figures 4.13 and 4.14 show the σ_{-1} and σ_2 braiding, respectively. Figure 4.15 shows the

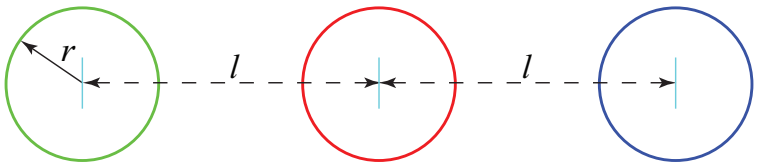

Figure 4.12: Radius of the rods and the distance between rods.

geometry of a stretched line from section 2 after the σ_{-1} braiding motion. The length of the material line $2ABC = 2(AB + BC)$ can be determined from the geometry as

$$2ABC = C_{rod}l, \tag{4.11}$$

where C_{rod} is a function of the rod size and the distance between rods, defined by

$$C_{rod} = \{2\alpha \sin^{-1}(a\alpha) + \sqrt{1 - 4\alpha^2}\}. \tag{4.12}$$

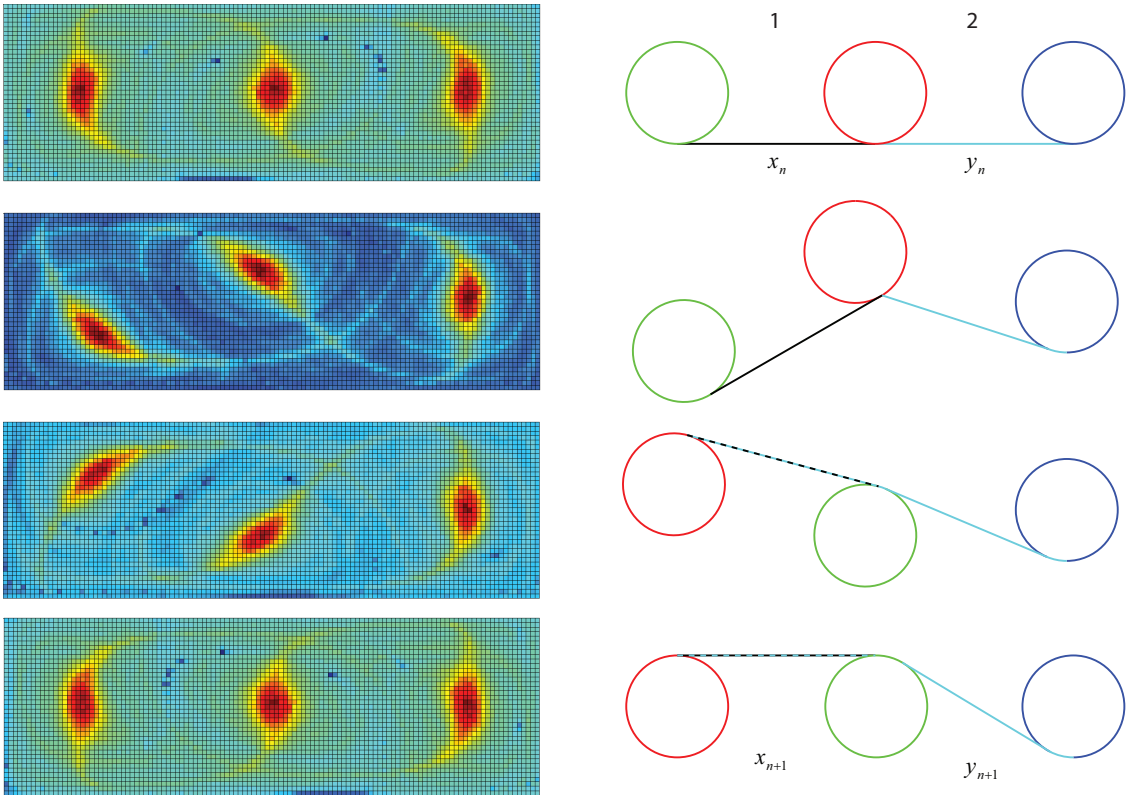

Figure 4.13: σ_{-1} braiding.

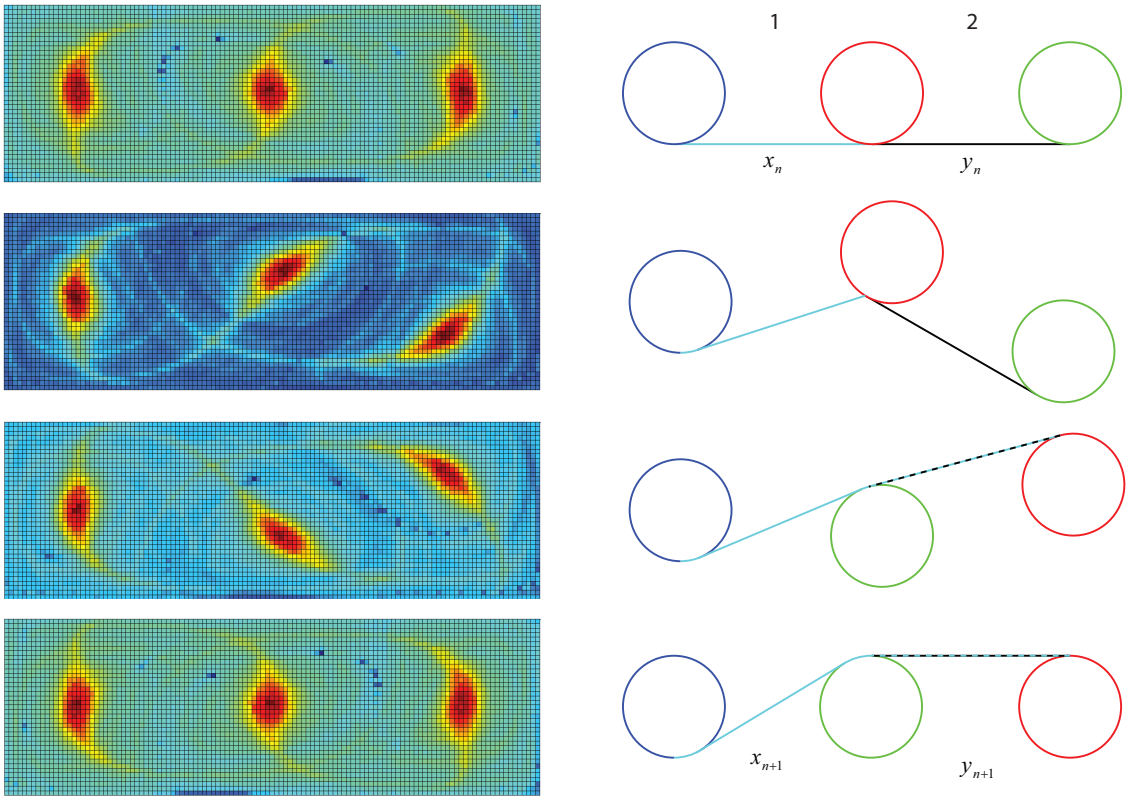

Figure 4.14: σ_2 braiding.

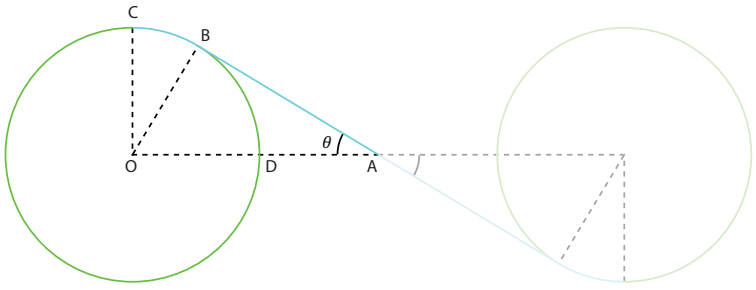

Figure 4.15: Geometrical details of one section of the stretched line.

As illustrated in Figs. 4.11(a) and 4.14, the material lengths between rods after the $(n+1)^{th}$ pulse with the σ_2 braiding motion are

$$x_{n+1} = C_{rod} x_n, \tag{4.13}$$

and (4.14)

$$y_{n+1} = x_n + y_n, \tag{4.15}$$

which can be written as

$$\begin{bmatrix} x_{n+1} \\ y_{n+1} \end{bmatrix} = M_2^{rod} \begin{bmatrix} x_n \\ y_n \end{bmatrix},$$

where

$$M_2^{rod} = \begin{bmatrix} C_{rod} & 0 \\ 1 & 1 \end{bmatrix}.$$

Again with reference to Figs. 4.11(b) and 4.13, the stretched material lengths after the $(n+1)^{th}$ pulse with σ_{-1} braiding motion are

$$x_{n+1} = x_n + y_n, \tag{4.16}$$

and (4.17)

$$y_{n+1} = C_{rod} y_n, \tag{4.18}$$

which can be written as

$$\begin{bmatrix} x_{n+1} \\ y_{n+1} \end{bmatrix} = M_{-1}^{rod} \begin{bmatrix} x_n \\ y_n \end{bmatrix},$$

where

$$M_{-1}^{rod} = \begin{bmatrix} 1 & 1 \\ 0 & C_{rod} \end{bmatrix}.$$

The matrix representation of braiding motion σ_2 followed by σ_{-1} can be written as

$$M = M_{-1}^{rod} M_2^{rod} = \begin{bmatrix} 1 & 1 \\ 0 & C_{rod} \end{bmatrix} \begin{bmatrix} C_{rod} & 0 \\ 1 & 1 \end{bmatrix} = \begin{bmatrix} C_{rod}+1 & 1 \\ C_{rod} & C_{rod} \end{bmatrix}.$$

The maximum eigenvalue of the matrix is thus

$$\lambda_{rod} = \frac{1}{2}(1 + 2C_{rod} + \sqrt{4C_{rod}+1}) \tag{4.19}$$

and an estimate of the topological entropy with rods of finite size is given by

$$h_{rod} = \log \lambda_{rod}. \tag{4.20}$$

In the limiting case when $r \to 0$, $C_{rod} \to 1$ and the matrix representation of the braiding motion converges to the matrix for pseudo-Anosov braiding motion with three rods using TNCT. In Section 4.5 it is shown that the almost invariant set with periodic structures moves with pseudo-Anosov type of braiding motion on which the TNCT is applied. Figure 4.16 shows a plot for the equivalent radius of a cyclic structure of the almost invariant set with three components and a periodic region covered by the manifolds connecting two hyperbolic points. For $\tau_f < 1.0$, there is no periodic point of lower order and the size of the almost invariant set structures control the actual topological entropy. For $1.0 < tau_f < 1.01$, the periodic points are enveloped by the periodic structures of almost invariant sets, so, the actual topological entropy is governed by the size of the almost invariant set structures. For $tau_f > 1.01$, size of the structure of almost invariant set with three components and the periodic region covered by the manifolds connecting two hyperbolic points are of equal size. Hence, almost invariant set structure size can be used to compute the value of C_{rod} using

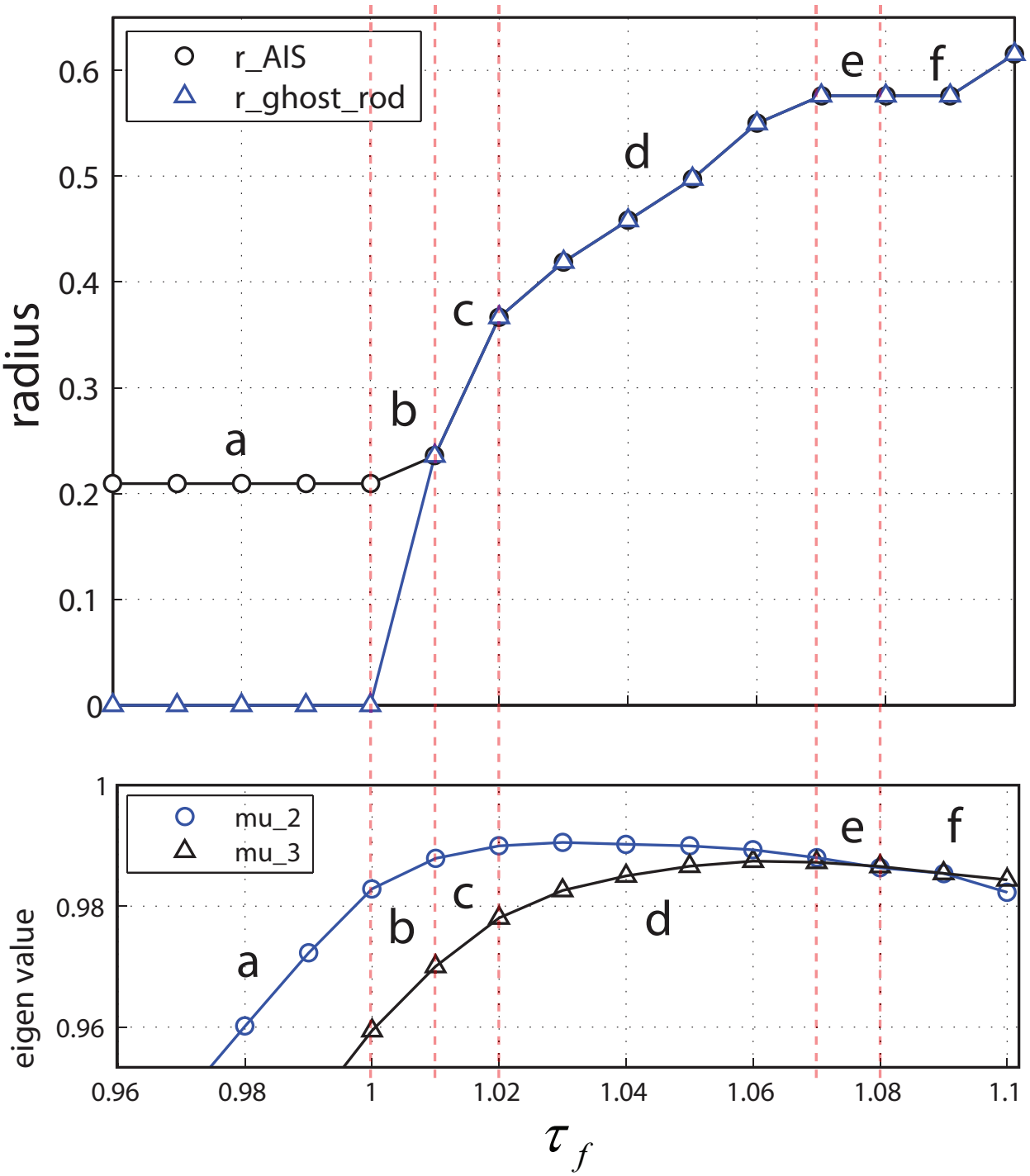

Figure 4.16: Plot for the equivalent radius of a cyclic structure of the almost invariant set with three components and a periodic region covered by the manifolds connecting two hyperbolic points (top) and the second and third eigenvectors for almost invariant sets (bottom).

Eq. (4.12). Radius of the a cyclic structure of almost invariant set is computed as

$$r_{AIS} = 0.5 * (r^h_{AIS} + r^v_{AIS}), \tag{4.21}$$

where r^h_{AIS} and r^v_{AIS} are size of a structure in horizontal and vertical direction, respectively. Plots for topological entropy and the second and third eigenvectors for almost invariant sets are shown in Fig. 4.17. This plots are divided into six different sections labeled as **a, b, c, d, e,** and **f** to explain the properties of topological entropy. Figure 4.18 shows the almost invariant sets corresponding to these sections.

Section a

There is no change in the component size of the almost invariant set with three structures, thus there is no change in h_{rod}. This can be used to explain the lack of change in h_f. The value of average topological entropy $h_{avg} = 0.5(h_{rod} + h_{TNCT})$ is very close to the computed topological entropy h_f.

Section b

Figures 4.18(ii), 4.18(iii), and 4.16 show small increment in the size of the braiding structures resulting the small increment in value of h_{rod}, hence verifying the small increment in the value of h_f. Once again, the value of h_{avg} is very close to the value of h_f.

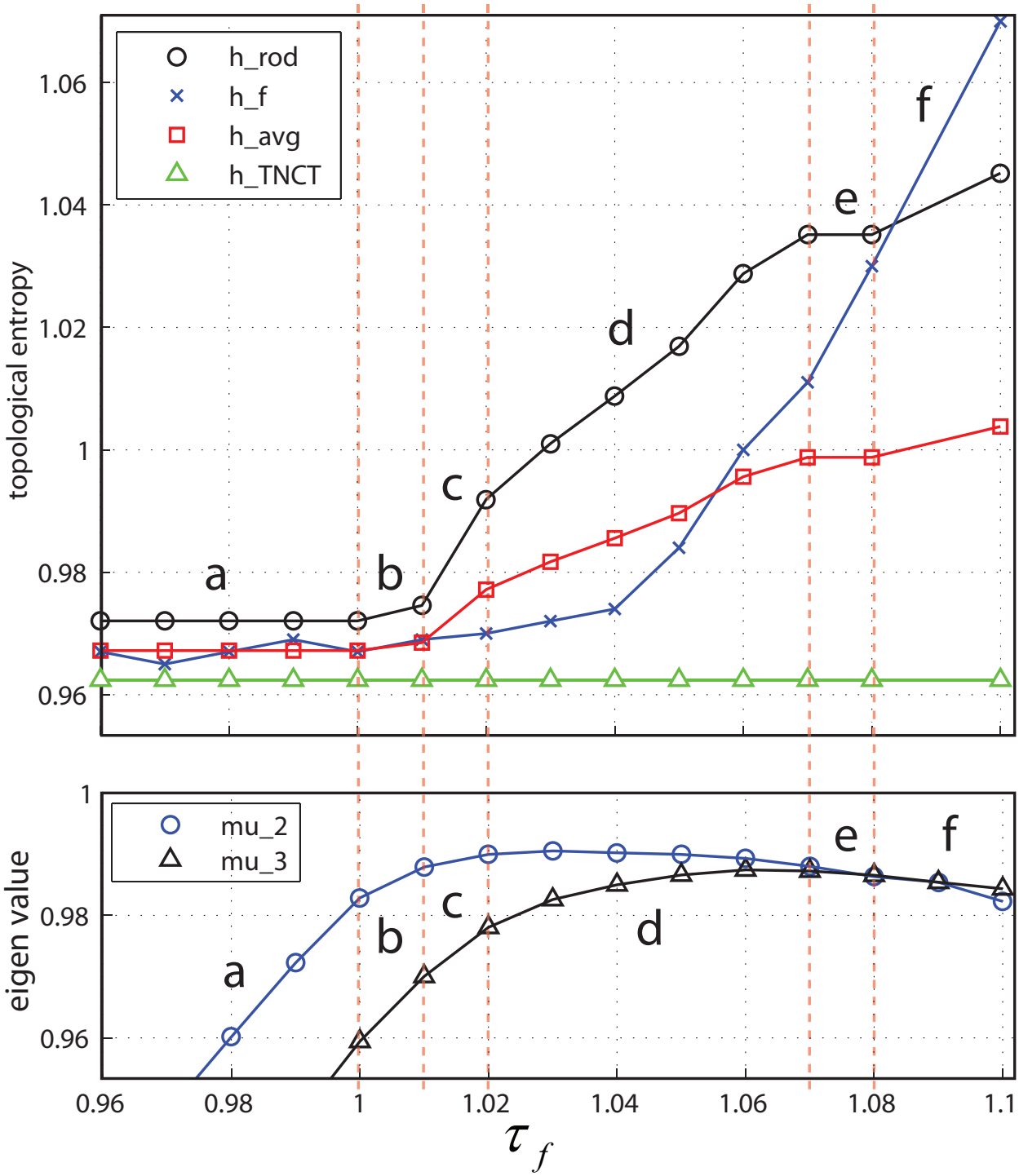

Figure 4.17: Plots for the topological entropy (top) and the second and third eigenvectors for almost invariant sets (bottom). h_{rod} is the topological entropy computed from the maximum eigenvalues of the braiding matrix with rod sizes considered, h_f is the topological entropy computed from the line stretching, h_{TNCT} is the topological entropy predicted by the TNCT, and $h_{avg} = (h_{rod} + h_{TNCT})/2$.

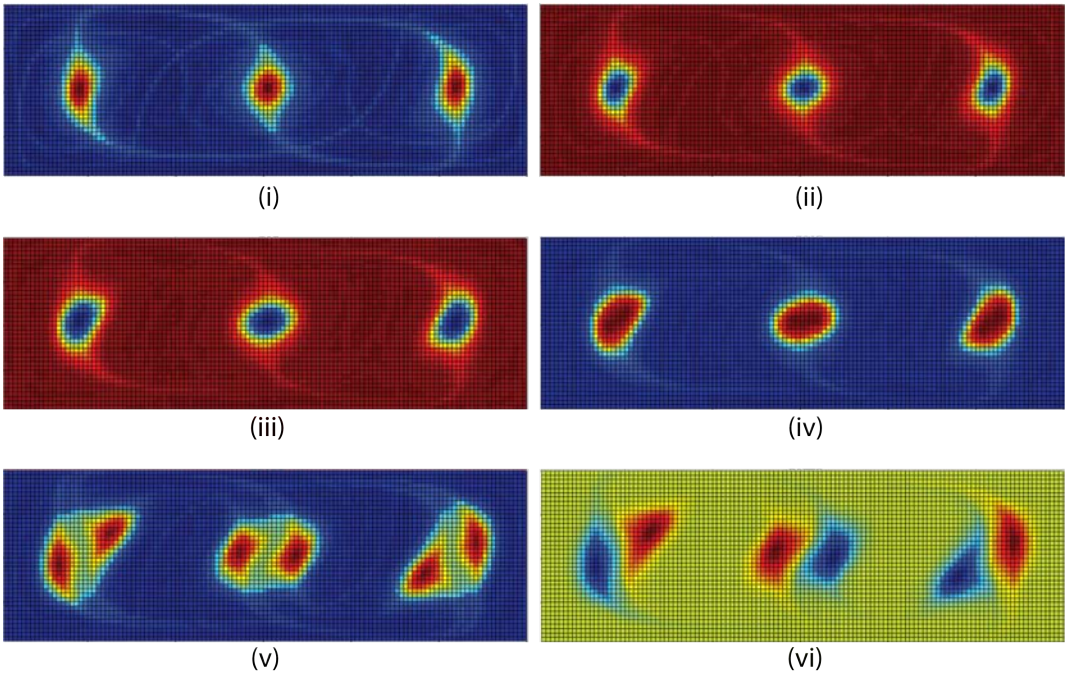

Figure 4.18: Almost invariant sets for lid-driven cavity flow with (i) $\tau_f = 0.98$, (ii) $\tau_f = 1.00$, (iii) $\tau_f = 1.01$, (iv) $\tau_f = 1.02$, (v) $\tau_f = 1.07$, and (vi) $\tau_f = 1.08$.

Section c

Figures 4.16 and 4.19 show that the size of the almost invariant set components are equal to the periodic area enveloped by the manifolds joining the hyperbolic points. Increment in

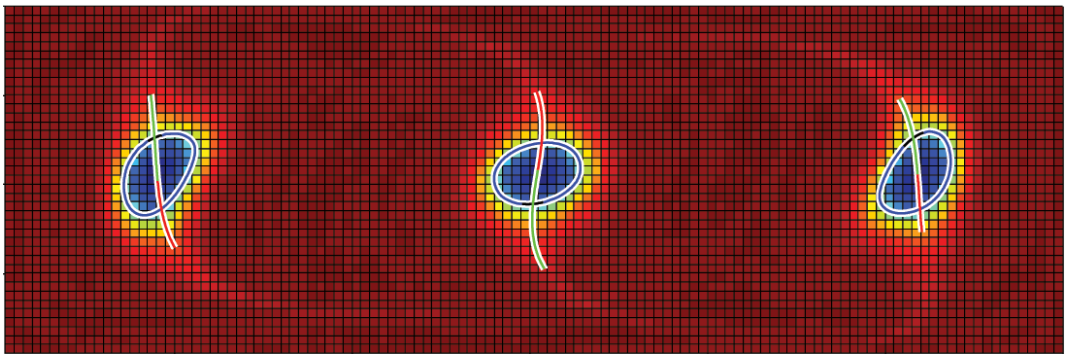

Figure 4.19: Plot for almost invariant sets and ghost rods for $\tau_f = 1.01$.

the size of the ghost rods resulting the increment in h_{rod}

Section d

For $1.02 < \tau_f < 1.07$ the almost invariant set with three periodic structures starts splits into six periodic structures resulting the high rate of increment of h_f. The presented model with the three rods system still predicts the value of h_f due to increment in size of the ghost rods as shown in Figs. 4.18(iv), 4.18(v), and 4.16.

Section e, and f

In these cases, the eigenvalues corresponding to the almost invariant set with six components are higher than the eigenvalues corresponding to the almost invariant set with three components. Figures 4.18(v) and 4.18(vi) shows the ghost rods structures. So, the braiding motion is due to the six periodic structures traveling together through the flow as shown in Fig. 4.20. The braiding motion of these six rods system is reducible to the pseudo-

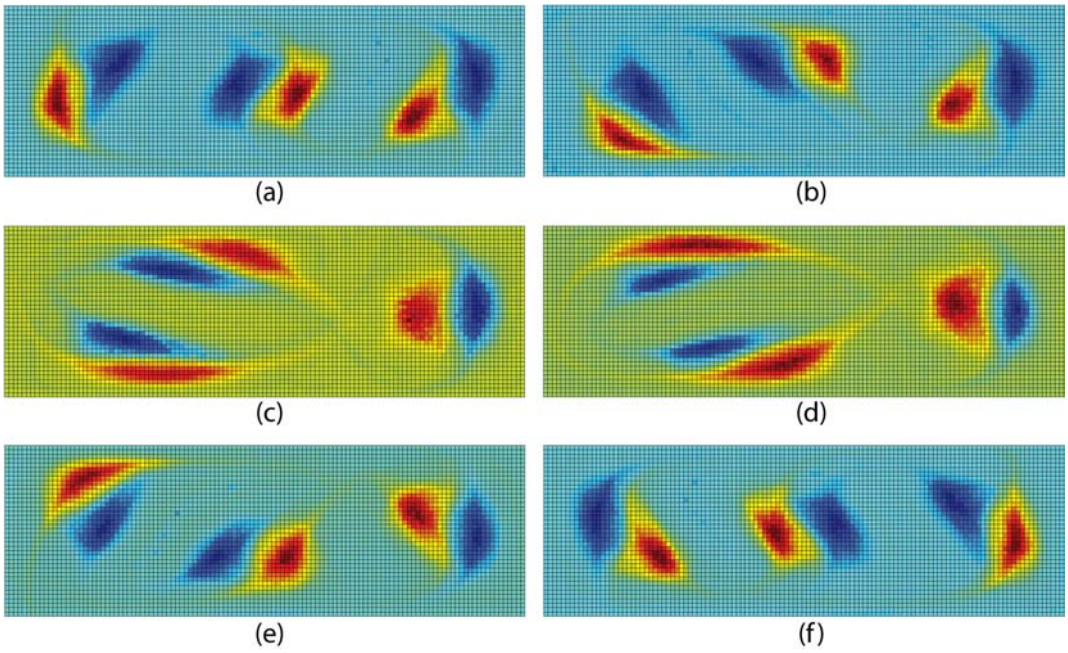

Figure 4.20: Braiding motion of almost invariant set structure with six components. The braiding motion is in the sequence of $a \to b \to c \to d \to e \to f$.

Anosov braiding shown in Fig. 4.9 but the finite size of the ghost rods lead to additional stretching and folding not predicted by the three rods system.

4.8 Lid-driven cavity flow with finite Reynolds number

The work presented in the previous section for lid-driven cavity flow assumes that the flow is Stokes flow. This assumption simplifies the flow and renders it completely determined by the boundary conditions such that an exact analytical solution exists. This enables the accurate tracking of particle trajectories in the flow for the purpose of measuring stretching rates. However, the Stokes flow assumption does not take into account the inertial effects that are present in many flows where the analytical solutions are valid only for small times, since the chaotic motion magnifies errors at an exponential rate. Dutta and Chevray [13] observed that inertial effects significantly enhanced mixing in the annular flow between two eccentric cylinders. Hobbs and Muzzio [22] found that for a Kenics static mixer, the formation of non-chaotic islands in the flow for $Re > 10$ leads to a loss in mixing efficiency.

It is concluded that the best mixing protocol depends strongly on the Reynolds number of operation of the mixing devices. Thus, it is necessary to study these flows at finite Reynolds number for the simulation and optimization of real-world mixers. To examine the effects of inertia for real systems, the Navier-Stokes equations are solved computationally by the group of *Andrew Duggleby and Pradeep C. Rao at Texas A&M University* for finite Reynolds number. These equations are solved in two dimensions using spectral-method techniques by first recasting them into the stream function vorticity formulation [39].

Topological chaos in lid-driven cavity flow

The complexity generated in fluid flow due to the topology of the boundary motion is computed by tracking a material line. Topological entropy is computed for various values of Re, as shown in Fig. 4.21. In Section 4.5, almost invariant set is shown as a natural object doing pseudo-Anosov braiding for the application of TNCT. In this section, we verify the existence

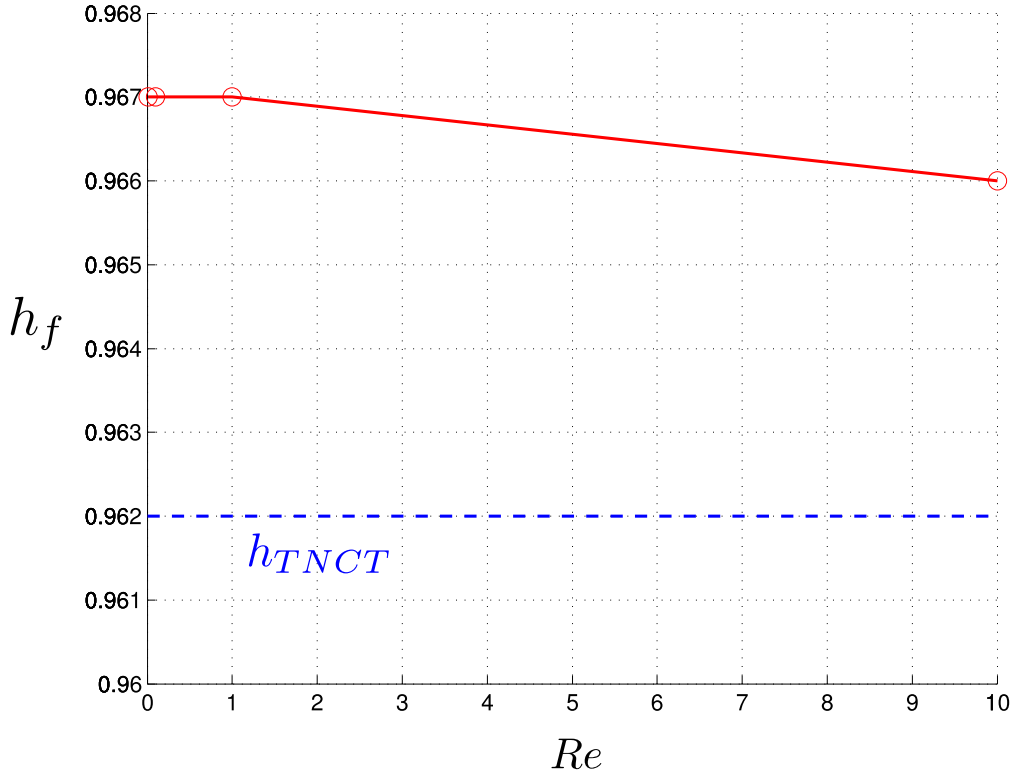

Figure 4.21: A plot for topological entropy with the finite Reynolds number.

of structures of almost invariant set in phase space that serve as ghost rods required for the existence of chaos by the application of TNCT.

Structures of almost invariant sets are approximated by the method discussed in Section 4.5. We cover the domain with a collection of 120×40 boxes, where 120 is the number of boxes in the horizontal direction and 40 is the number of boxes in the vertical direction. A total of sixteen (16) equally spaced points are taken in each box. Figure 4.22 shows plots for eigenvalues corresponding to the almost invariant sets with three and six components. Structures of almost invariant set corresponding to second highest eigenvalues are also shown in Fig. 4.22. The almost invariant set structures are present in the flow for Re$\leq$ 10, and these structures braid in the fluid as discussed in Section 4.6.2. Hence, the lower bound on the topological entropy is given by $h_{TNCT} \approx 0.962$, which is verified in the plot for h_f in

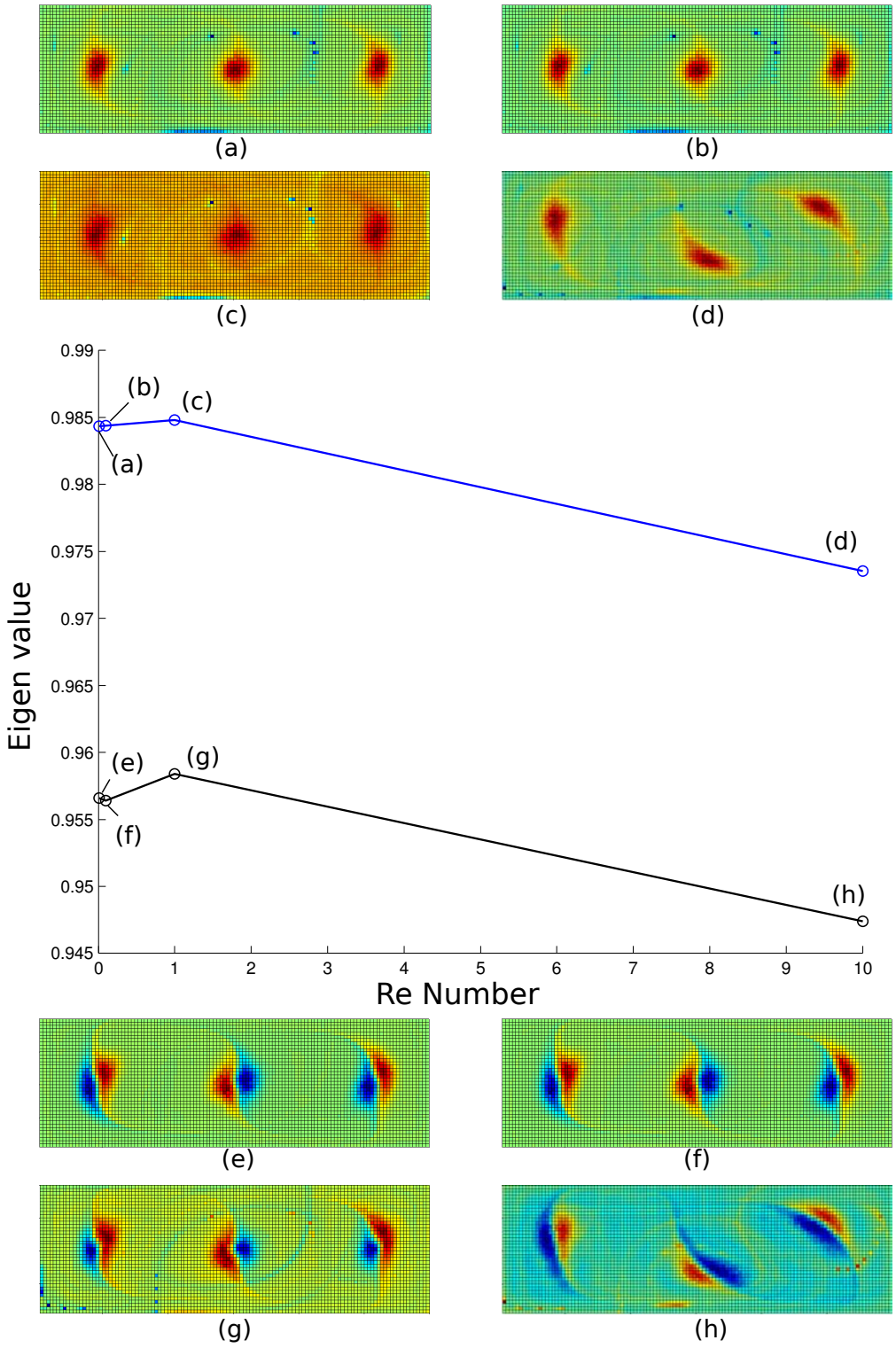

Figure 4.22: The blue curve plots the eigenvalues corresponding to the almost invariant sets with three components. The black curve plots the eigenvalues corresponding to the almost invariant sets with six components.

Fig. 4.21.

4.9 Summary

In this chapter, stretching and chaos is investigated in pulsed lid-driven cavity flow. One specific set of boundary conditions with $\tau_f = \tau_f^* = 1$, termed the reference case, generates three periodic points leading to a pseudo-Anosov type braid in $(2+1)$-dimensional space-time as shown in Fig. 4.2(d) [10]. The three periodic points are identified as ghost rods. The TNCT predicts the lower bound on topological entropy $h_{TNCT} = 0.962$ for this system. The actual topological entropy of this flow $h_f = 0.968$ is determined by computing the stretching rate of topologically nontrivial lines, which is well represented by the lower bound predicted by the TNCT. The boundary condition is first perturbed for $\tau_f < \tau_f^*$ to destroy the periodic orbits and then perturbed for $\tau_f > \tau_f^*$ to break each periodic point into a set of two hyperbolic points and two elliptic points forming a ghost rod structure as shown in Fig. 4.4.

In the first case, when $0.93 < \tau_f < \tau_f^*$, there is no periodic point generating a pseudo-Anosov type braid in the domain and the TNCT still provides a good estimate of the lower bound. This chapter generalizes the TNCT to systems which have no periodic points by the use of almost invariant set structures. It is shown that the almost invariant set structure braid non-trivially and mimic the behavior of physical rods or periodic points that is required for the existence of chaos using the TNCT.

In the second case, when $\tau_f > \tau_f^*$, the four periodic points travel together through the flow, simply twisting around one another. The resulting braid is reducible to the pseudo-Anosov type and the predicted lower bound on h remains $h_{TN} \approx 0.962$.

A method is discussed to predict line stretching by tracking the pseudo-Anosov type of braiding motion with three finite size rods. This method leads to a matrix for pseudo-Anosov type of braiding motion with finite size rods. The logarithm of the maximum eigenvalue of the matrix predicts a value close to the topological entropy. In the limiting case, when the sizes of rods are zero, the method leads to a matrix for pseudo-Anosov type of braiding which matches with the generator matrix derived from the TNCT. This method verifies the near constant values of topological entropy for $0.96 \leq \tau_f \leq 1.01$, which is due to the constant size of the almost invariant set structures.

In the last section, the concept of almost invariant sets as ghost rods is established for the application of the TNCT to the lid-driven cavity flow with finite Reynolds number. The TNCT predicts the lower bound of the pseudo-Anosov type braiding motion for Re$\leq$ 10.

Chapter 5

Conclusions

This thesis analyzes fluid transportation in two pulsed laminar flow systems that can generate chaos. The considered pulsed laminar flow systems are

- Pulsed source-sink system
- Pulsed lid-driven cavity flow.

Pulsed source-sink systems are presented in chapter 3 to achieve chaotic advection in a flow between two closely spaced parallel plates. Fluid flow between two closely spaced parallel plates is modeled as Hele-Shaw flow with the depth averaged velocity proportional to the gradient of the pressure. So, with the depth-averaged velocity, the flow between the parallel plates can effectively be modeled as a two-dimensional potential flow. Chaos is generated in fluid by the pulsed operation of fluid extraction and reinjection through singularities in the domain. A singularity through which fluid is injected (or extracted) is called a source (or a sink). In a bounded domain, one source and one sink with equal strength operate together as a source-sink pair to conserve the volume of fluid. Kolmogorov-Sinai entropy is used as a mixing measure for the system. Maximum Lyapunov exponent and Poincaré section are

computed to determine the mixing measure. This thesis analyzes chaos generated in the pulsed source-sink systems with various design parameters like the strength of sources (or sinks), position of source-sink pairs in the domain, and the method of fluid relocation. Two different orientations of source-sink pairs are analyzed in this thesis:

- Crossed source-sink system
- Parallel source-sink system

as shown in Fig. 3.5. Two different methods for fluid relocations "LOFI" and "FOFI" are used to transport the extracted fluid through a sink to a source. In addition, a pulsed source-sink system without fluid relocation is analyzed in Section 3.5. In this system, a singularity in the domain can extract and reinject fluid; thus, a singularity can either act as a source or as a sink during a pulse. Fluid extracted through a singularity, when it is active as a sink, is reinjected through the same singularity when it is active as a source. The absence of fluid relocation reduces the fabrication requirement. In addition, delay time due to the extracted fluid relocation is comparatively zero. Fluid flow is chaotic in this system for different orientations of source-sink pair.

Pulsed source-sink systems with "FOFI" reinjection scheme generate comparatively more complex fluid flow than other pulsed source-sink systems. The pulsed source-sink system without fluid relocation generates comparatively more complex fluid flow than the pulsed source-sink systems with "LOFI" reinjection scheme. The pulsed source-sink system without fluid relocation is easy to fabricate for microfluidic systems. In addition, this system can easily be applied to groundwater flows.

In Chapter 4, we study the phase space mixing and transport in a lid-driven cavity flow. We extended the TNCT based framework to systems that do not have any fixed points. The almost invariant set structure is approximated in phase space of the lid-driven cavity

flow using set oriented transfer operator. The actual topological entropy of this flow is determined by computing the stretching rate of topologically nontrivial lines to demonstrate the validity of the lower bound predicted by the TNCT.

A method is discussed to predict line stretching by tracking the pseudo-Anosov type braiding motion with three finite size rods. This method generates a matrix for the pseudo-Anosov type of braiding motion. The logarithm of the maximum eigenvalue of the matrix predicts a value close to the topological entropy. In the limiting case, when the size of rods are zero, the method leads to a matrix for pseudo-Anosov type of braiding which matches with the generator matrix derived from the TNCT. This method verifies the near constant values of topological entropy for $0.96 \leq \tau_f \leq 1.01$ which is due to the constant size of the almost invariant set structures.

In Section 4.8, the concept of almost invariant set as ghost rods is established for the application of TNCT to the lid-driven cavity flow with finite Reynolds number. This study extends the TNCT based framework to the use of almost invariant set in real-world fluid mixing problem.

Bibliography

[1] R. L. Adler, A. G. Konheim, and M. H. McAndrew. Topological entropy. *Transactions of the American Mathematical Society*, 114:309–319, 1965.

[2] H. Aref. Stirring by chaotic advection. *Journal of Fluid Mechanics*, 143:1–21, 1984.

[3] G. K. Batchelor. *An Introduction to Fluid Dynamics*. Cambridge University Press, Cambridge, UK, 1967.

[4] F. Bertucci, P. Viens, R. Tagett, C. Nguyen, R. Houlgatte, and D. Birnbaum. DNA arrays in clinical oncology: Promises and challenges. *Laboratory Investigation*, 83:305–316, 2003.

[5] M. Bestvina and M. Handel. Train tracks and automorphisms of free groups. *The Annals of Mathematics*, 135:1–51, 1992.

[6] M. Bestvina and M. Handel. Train-tracks for surface homeomorphisms. *Topology*, 34: 109–140, 1995.

[7] R. Bowen. Entropy and the fundamental group. *The Structure of Attractors in Dynamical Systems, Lecture Notes in Mathematics, Springer-Verlag, Berlin*, 668:21–29, 1978.

[8] P. L. Boyland, H. Aref, and M. A. Stremler. Topological fluid mechanics of stirring. *Journal of Fluid Mechanics*, 403:227–304, 2000.

[9] A. J. Casson and S. A. Bleiler. *Automorphisms of Surfaces after Nielsen and Thurston*. Cambridge University Press, Cambridge, UK, 1988.

[10] J. Chen. *Topological chaos and mixing in lid-driven cavities and rectangular channels*. PhD thesis, Virginia Polytechnic Institute and State University, Blacksburg, VA, 2008.

[11] M. J. Clifford and S. M. Cox. Smart baffle placement for chaotic mixing. *Nonlinear Dynamics*, 43:117–126, 2006.

[12] J. L. DeRisi and V. R. Iyer. Genomics and array technology. *Current Opinion in Oncology*, 11:76–79, January 1999.

[13] P. Dutta and R. Chevray. Inertial effects in chaotic mixing with diffusion. *Journal of Fluid Mechanics*, 285:1–16, 1995.

[14] C. Eckart. An analysis of the stirring and mixing process in incompressible fluids. *Journal of Marine Research*, VII:265–275, 1948.

[15] K. A. Elraies and M. H. Yunan. Determination of water breakthrough time in noncommunicating. *E-journal of Reservoir Engineering*, 1(1), 2007.

[16] J. Evans, D. Liepmann, and A. P. Pisano. Planer laminar mixer. *In Proceedings of the IEEE International Workshop Microelectromechanical Systems*, pages 96–101, January 1997.

[17] J. M. Franks and M. Handel. Entropy and exponential growth of 1 in dimension two. *Proceedings of American Mathematical Society*, 102(3):753760, 1988.

[18] G. Froyland. Extracting dynamical behaviour via markov models. In *Proceedings, Newton Institute*, pages 283–324. Birkhauser, 1998.

[19] P. Gaspard and J. R. Dorfman. Chaotic scattering theory, thermodynamic formalism, and transport coefficients. *Physical Review E*, 52:35253552, 1995.

[20] E. Gouillart, J. L. Thiffeault, and M. D. Finn. Topological mixing with ghost rods. *Physical Review E*, 73(3), Mar. 2006.

[21] M. J. Heller. DNA microarray technology: devices, systems, and applications. *Annual Review of Biomedical Engineering*, 4:129–153, 2002.

[22] D. M. Hobbs and F. J. Muzzio. Reynolds number effects on laminar mixing in the kenics static mixer. *Chemical Engineering Journal*, 70:93–104, 1998.

[23] R. Jendrejack, J. J. de Pablo, and M. D. Graham. Stochastic simulations of DNA in flow: dynamics and the effects of hydrodynamic interactions. *Journal of Chemical Physics*, 116:7752–7759, 2002.

[24] S. Jones and H. Aref. Chaotic advection in pulsed source-sink systems. *Physics of Fluids*, 31:469–485, 1988.

[25] D. R. Lester, G. Metcalfe, M. G. Trefry, A. Ord, B. Hobbs, and M. Rudman. Lagrangian topology of a periodically reoriented potential flow: Symmetry, optimization, and mixing. *Physical Review E*, 80:036208, 2009.

[26] A. J. Lichtenberg and M. A. Lieberman. *Regular and Chaotic Dynamics*. Springer-Verlag, Berlin, 1992.

[27] A. Lyapunov. Problème générale de la stabilité du mouvement. *Annales de la Faculté des Sciences de Toulouse*, 9:203–474, 1907.

[28] W. Magnus. Braid group: A survey. *Proceedings of the Second International Conference on the Theory of Groups, Lectures Notes in Mathematics, Springer-Verlag, Berlin*, 372: 463–487, 1974.

[29] M. K. McQuain, K. Seale, J. Peek, T. Fisher, S. Levy, M. A. Stremler, and F. R. Haselton. Chaotic mixer improves microarray hybridization. *Analytical Biochemistry*, 325:215, 2004.

[30] V. V. Meleshko. Steady flow in a rectangular cavity. *Proceedings of the Royal Society of London A*, 452:19992002, 1996.

[31] G. Metcalfe, D. Lester, A. Ord, P. Kulkarni, M. Trefry, E. H. Bruce, K. Regenaur-Lieb, and J. Morris. A partially open porous media flow with chaotic advection: towards a model of coupled fields. *Philosophical Transactions of the Royal Society A*, 368:217–230, 2010.

[32] S. Mohr, G. D. Leikauf, G. Keith, and B. H. Rihn. Microarrays as cancer keys: An array of possibilities. *Journal of Clinical Oncology*, 20:3165–3175, July 2002.

[33] S. Newhouse and T. Pignataro. On the estimation of topological entropy. *Journal of Statistical Physics*, 72(5-6):1331–1351, 1993.

[34] V. I. Oseledec. A multiplicative ergodic theorem. Lyapunov characteristic numbers for dynamical systems. *Transactions of the Moscow Mathematical Society*, 19:197–231, 1968.

[35] J. M. Ottino. *The Kinematics of Mixing: Stretching, Chaos, and Transport*. Cambridge University Press, Cambridge, UK, 1989.

[36] Y. B. Pesin. Characteristic lyapunov exponents and smooth ergodic theory. *Russian Mathematical Surveys*, 32:55114, 1977.

[37] H. Poincaré. *Les Méthodes Nouvelles de la Mécanique Céleste (New Methods in Celestial Mechanics)*, volume 1-3. Gauthier-Villars, Paris, 1892-1899. Reprinted by Dover, New York, 1957.

[38] H. Poincaré, editor. *Science et Methode*. Ernest Flammarion, 1908.

[39] P. Rao, A. Duggleby, M. A. Stremler, and P. Kumar. Analysis of topological chaos in ghost rod mixing at finite reynolds numbers using spectral methods.

[40] K. Sato, A. Hibara, M. Tokeshi, H. Hisamoto, and T. Kitamori. Microchip-based chemical and biochemical analysis systems. *Advanced Drug Delivery Reviews*, 55:379–391, 2003.

[41] Y. G. Sinai. On the notion of entropy of a dynamical system. *Doklady of Russian Academy of Sciences*, 124:768–771, 1959.

[42] Y. G. Sinai. *Dynamical Systems II*. Springer-Verlag, Berlin, 1989.

[43] M. A. Stremler and C. Baratunde. Chaotic advection and mixing in pulsed source-sink systems. In *XXI ICTAM*, 2004.

[44] M. A. Stremler and C. Baratunde. A mixing entropy approach to optimal mixing in a pulsed source-sink flow. *Physics of Fluids*, 18:011701, 2006.

[45] M. A. Stremler and J. Chen. Generating topological chaos in lid-driven cavity flow. *Physics of Fluids*, 19:103602, 2007.

[46] M. A. Stremler and B. A. Cola. A maximum entropy approach to optimal mixing in a pulsed sourcesink flow. *American Institute of Physics*, 18:011701, 2006.

[47] M. A. Stremler, F. R. Haselton, and H. Aref. Designing for chaos: applicayions of chaotic advection at the microscale. *Philosophical Transactions of the Royal Society A*, 362:1019–1036, 2004.

[48] M. A. Stremler, S. D. Ross, P. Grover, and P. Kumar. Topological chaos by periodic braiding of almost-cyclic sets. submitted, 2010.

[49] A. D. Stroock, S. K. W. Dertinger, A. Ajdari, I. Mezic, H. A. Stone, and G. M. Whitesides. Chaotic mixer for microchannels. *Science*, 295:647–651, 2002.

[50] D. Therriault, S. R. White, and J. A. Lewis. Chaotic mixing in three-dimensional microvascular networks fabricated by direct-write assembly. *Nature Materials*, 2:265–271, 2003.

[51] J.-L. Thiffeault. Measuring topological chaos. *Physical Review Letters*, 94:084502, 2005.

[52] J.-L. Thiffeault. Braids of entangled particle trajectories. *Chaos*, 20:017516, 2010.

[53] J.-L. Thiffeault and M. D. Finn. Topology, braids, and mixing in fluids. *Philosophical Transactions of the Royal Society A*, 364:3251–3266, 2006.

[54] D. B. Tuckerman and R. F. W. Pease. High-performance heat sinking for vlsi. *IEEE Electron Device Letters*, 2:126–129, 1981.